eXPRESS Polymer Letters Vol.4, No.4 (2010) 196
Available online at www.expresspolymlett.com
DOI: 10.3144/expresspolymlett.2010.25

Editorial corner – a personal view
Science Babel: Does the lack of a common terminology in the field of emulsion templating hinder progress?

*K. Kim, A. Bismarck**

Department of Chemical Engineering, Polymer and Composite Engineering (PaCE) Group, Imperial College London, South Kensington Campus, London, SW2 7AZ, UK

Emulsion templating to produce macroporous polymers with a well defined structure has developed into an established research area. Potential applications of very concentrated emulsions and macroporous polymers made from them rapidly expanded from food preparation to cosmetics and from oil recovery and to tissue engineering, respectively. In particular, high internal phase emulsions (HIPEs) are widely used as template to create very high porosity macroporous polymers, commonly known as poly(merised)HIPEs. Emulsion templating has proved to be extremely useful to manufacture tailor made highly interconnected open porous polymers. The advantage of this method is that the template is liquid which allows moulding it to any desired shapes. Polymer foams produced by emulsion templating have been explored for many applications. For instance, polyHIPEs based on biodegradable components show excellent biocompatibility for a wide range of cell types.

As the field is growing, many researchers have joined and produced remarkable research outcomes. More and more research groups are producing new templates and polymer foams for numerous applications but there are growing concerns about the non-consensual use of terminology. The very nature of making new materials inspires researchers to create new names to refer to their research outcomes on the basis of potential applications. This has become reality now: Researchers use different terminology for the emulsion templates, ranging from concentrated emulsions to HIPEs. Even if polymerised the resulting polymers were given different names, such as polyHIPE, macroporous polymers and polyFoams. Researchers also refer to an identical pore structure of 'polyHIPEs' with different names. There are plenty of examples causing potential confusion; for instance, the 'spherical' cavities in the macroporous polymers are called differently: pores, voids, cells and cavities. Moreover, the 'holes' in the polymer walls forming at contact points of neighbouring droplets during the polymerisation are called by some researchers pore throats, another research team names them windows. However, recently it becomes more complicated as researchers call them interconnecting pores or intercellular pores.

At the current stage, researchers seem not to be bothered by this diversified usage of terminology. However, as the field is growing, the confusion could cause babelisation of the field. As researchers produce interesting and promising outcomes, they are enticed to baptise their own creations. Before reaching the incommensurable state between researchers, the field needs to be unified with a well defined terminology for referring to new materials. The game of name is a part of progressing science but it might hinder progress in this interdisciplinary field as it becomes harder to identify what others have done – leading potentially to reinvent the wheel.

*Corresponding author, e-mail: a.bismarck@imperial.ac.uk

eXPRESS Polymer Letters Vol.4, No.4 (2010) 197–209
Available online at www.expresspolymlett.com
DOI: 10.3144/expresspolymlett.2010.26

Interrelationships of morphology, thermal and mechanical properties in uncrosslinked and dynamically crosslinked PP/EOC and PP/EPDM blends

*R. R. Babu, N. K. Singha and K. Naskar**

Rubber Technology Centre, Indian Institute of Technology, Kharagpur-721302, West Bengal, India

Received 22 December 2009; accepted in revised form 28 January 2010

Abstract. Thermoplastic vulcanizates (TPVs) based on polypropylene (PP) with ethylene octene copolymer (EOC) and ethylene propylene diene rubber (EPDM) have been developed by coagent assisted dicumyl peroxide crosslinking system. The study was pursued to explore the influence of two dissimilar polyolefin polymers (EOC and EPDM) having different molecular architectures on the state and mode of dispersion of the blend components and their effects with special reference to morphological, thermal and mechanical characteristics. The effects of dynamic crosslinking of the PP/EOC and PP/EPDM have been compared by varying the concentration of crosslinking agent and ratio of blend components. The results suggested that the uncrosslinked and dynamically crosslinked blends of PP/EOC exhibit superior mechanical properties over PP/EPDM blends. From the hystersis experiments it was found that PP/EOC blends also perform better fatigue properties over PP/EPDM based blends. It was demonstrated that, the origin of the improved mechanical properties of EOC based blends is due to the combined effect of the unique molecular architecture with the presence of smaller crystals and better interfacial interaction of EOC phase with PP as supported by the results of thermal and fatigue analyses.

Keywords: *polymer blends and alloys, polypropylene, ethylene octene copolymer, ethylene propylene diene rubber, thermoplastic vulcanizate*

1. Introduction

Blending of polymers is often an important route for obtaining new and improved polymeric materials, which are difficult to obtain by direct polymerization process [1, 2]. In addition to the family of synthesized thermoplastic elastomers (TPEs), advances in the rubber-plastic blends lead to the development of new avenues to prepare TPEs with tailor made properties by varying the blend ratio of the components. Thermoplastic vulcanizates (TPVs) are special class of TPEs prepared by dynamic vulcanization process which involves the crosslinking of rubber part while it is being mixed with the molten thermoplastic at high shear rate [3–5]. Amongst the various blends, polypropylene (PP)/ethylene propylene diene rubber (EPDM) blends have gained tremendous importance due to commercial interest because of the structural compatibility. A large number of reports have been published on the PP/EPDM uncrosslinked and dynamically crosslinked blends [3–5]. Recently, new families of ethylene-alpha olefin copolymers have gained significant attention due to their unique molecular architecture with narrow molecular weight distribution, uniform co-monomer distribution and long chain branching along the polymer backbone [6]. Ethylene octene copolymer (EOC) in particular has been shown to provide better toughening characteristics to PP, when compared with the conventionally used EPDM rubber [7, 8].

*Corresponding author, e-mail: knaskar@rtc.iitkgp.ernet.in

Presently, EOC is used for the impact modification of PP for various applications especially in the automotive sectors. Moreover, these materials are available in the form of pellets that help in easy handling, faster mixing and compounding. Nevertheless, reports on dynamically vulcanized PP/EOC TPVs are scanty. In case of TPVs, in addition to the constituent polymers, type of curing agent plays a major role in determining the final performance of the TPVs. Among several crosslinking systems used in the preparation of PP/EPDM TPVs, phenolic resin gained more commercial success due to its crosslinking and compatiblizing tendency [2]. However, in this particular PP/EOC blend system phenolic resin is ineffective, since the latter needs the presence of unsaturation to form a crosslinked network structure. Furthermore, use of phenolic resin in PP/EPDM blends causes black specks in the products which motivates the development of other crosslinking systems [9]. In that case, peroxides can be used which crosslink both saturated and unsaturated polymers without any reversion characteristics. However, the activity of peroxide depends on the type of polymer and presence of other ingredients in the system. It has been well established that PP exhibits β-chain scission (degradation) with the addition of peroxide [10]. Hence the use of peroxide alone is limited in the preparation of PP based TPVs. In general, to minimize the unwanted side reactions, coagent assisted peroxide crosslinking system is recommended. Naskar *et al*. [11, 12] studied the influence of different peroxides and multifunctional peroxide (having peroxide and coagent functionality in a single molecule) in the conventional PP/EPDM blends. Recently, Naskar *et al.* [13] have been involved in the development of a novel PP/EPDM TPVs by electron beam induced reactive processing. Special purpose TPVs based on silicone rubber [14] and maleated ethylene propylene rubber (m-EPM) [15] were also developed from the same lab. Lai *et al*. [16] investigated the fracture behavior and physico-mechanical properties of peroxide cured PP/EOC TPVs. As a part of the extensive research work on the peroxide cured PP/EOC TPVs, our earlier report deals with the influence of different peroxides [17], different coagents [18] and different mixing sequences [19, 20] on the solid and melt state viscoelastic properties of PP/EOC TPVs.

The present study primarily aims to evaluate the performance of the coagent assisted peroxide cured PP/EOC TPVs as a potential alternative to the conventional PP/EPDM TPVs. In this work, the morphological evolution and its influence on the mechanical and thermal properties have been investigated for both PP/EOC and PP/EPDM uncrosslinked and dynamically crosslinked blends. Detailed comparisons were pursued on morphological, thermal and mechanical properties. Investigation had been made to correlate the observed results with the microstructural architecture of the constituent polymers.

2. Experiemental

2.1. Materials

Isotactic polypropylene (PP), ethylene-octene copolymers (EOC) and ethylene propylene diene rubber (EPDM) were used as blend components. Metallocene catalyzed ethylene octene copolymers (Exact® 5171) were employed in this study. The octene content of these Exact copolymers was

Table 1. Molecular characteristics of the polymers

Polymer/properties	PP	EOC	EPDM
Specific gravity	0.90	0.87	0.86
MFI [g/10 min]	3.0 at 230°C/2.16 kg	1.0 at 190°C/2.16 kg	–
ML (1+4) at 125°C	–	25	55
M_n [g/mol]	218 967	277 751	273 082
M_w [g/mol]	949 319	494 872	622 876
PDI (M_w/M_n)	4.33	1.78	2.28
Octene content [%]	–	13	–
Ethylidene norbornene (ENB) content [%]	–	–	4.6
Propylene content [%]	99.9	–	25.4
Zero shear viscosity [Pa·s]*	1020	1980	4130
Grade	Koylene ADL (AS030N)	Exact 5171	Keltan 5508
Supplier	IPCL, India	ExxonMobil Chemical, USA	DSM Elastomers, The Netherlands

MFI – Melt flow index; PDI – Polydispersity index; M_n – number average molecular weight; M_w – Weight average molecular weight
*measured at a very low shear rate using Smart Rheo (Ceast, Italy) Capillary Rheometer at 180°C with 40:1 *L/D* capillary

determined from Proton Nuclear Magnetic Resonance Spectroscopy (^{1}H-NMR) measurement. The material and molecular characteristics of PP, EOC and EPDM are given in Table 1. The polymers taken for comparison are EOC and EPDM which were selected on the basis of number average molecular weight that lies relatively in the same range. Dicumyl peroxide (DCP) (Perkadox-BC-40B-PD) having active peroxide content of 40%; temperature at which half life time ($t_{1/2}$) is 1 hour at 138°C; specific gravity of 1.53 g/cm^3 at 23°C was obtained from Akzo Nobel Chemical Company, The Netherlands. N-N′-m-phenylene dimaleimide (MPDM) (SR 525; specific gravity, 1.44 g/cm^3 at 23°C) was obtained from Sartomer Company, USA.

2.2. Preparation of TPVs

TPVs were prepared by melt mixing of PP with EOC/EPDM (rubbery material) in a Haake Rheomix 600s with a mixing chamber volume of 85 cm^3 at a temperature of 180°C. Batch sizes were about 60 g. Total mixing time for each batch was 14 minutes. At first, PP was allowed to soften for 3 minutes and then rubbery material was added to the chamber and melt mixing was carried out for 5 minutes. Dynamic vulcanization was pursued by adding co-agent assisted peroxide for 2 minutes. Mixing was continued for another 4 minutes to complete the vulcanization. The compositions of TPVs employed for this study are shown in Table 2. For better understanding, blend ratios are designated as X, Y and Z for 75, 50 and 25% of PP respectively. TPVs prepared by different rubbery materials are designated as follows: C for EOC and D for EPDM. For example, YC corresponds to the composition of 50:50 PP/EOC uncrosslinked blends and ZD for 25:75 PP/EPDM uncrosslinked blend. Dynamically vulcanized blends are designated with prefixes D2 or D4 followed by corresponding blend ratio designation. The letter D2 or D4 corresponds to the type and concentration of peroxide (dicumyl peroxide of 2 phr or 4 phr). For example, D2ZC corresponds to the composition containing 2 phr (parts per hundred grams of rubber) of dicumyl peroxide in the 25:75 PP/EOC blend ratio. After mixing, the blends were removed from the chamber at hot condition and sheeted out on a two roll mill in a single pass. Sheets were then cut and pressed in a compression molding machine (Moore Press, Birmingham, UK) at 190°C for 4 min at 5 MPa pressure. Aluminum foils were placed between the mold plates. The molded sheets were then cooled down to room temperature under the same pressure.

Table 2. TPV compositions in phr

Polymers/ Designations	PP	EOC	EPDM
XC	75	25	–
YC	50	50	–
ZC	25	75	–
XD	75	–	25
YD	50	–	50
ZD	25	–	75

Prefix: D2 – Dynamically vulcanized blends with 2 phr DCP
D4 – Dynamically vulcanized blends with 4 phr DCP

2.3. Testing procedures

Morphology – Morphology studies were carried out using a scanning electron microscope (SEM) (JEOL JSM 5800, Japan). Molded samples of PP/EOC or PP/EPDM TPVs were cryofractured in liquid nitrogen to avoid any possibility of phase deformation during the fracture process. In case of uncrosslinked blends, the EOC or EPDM phase was preferentially extracted by treating with hot xylene at 50°C for 15 min, whereas in dynamically vulcanized blends the PP phase was preferentially and partially extracted by etching with hot xylene at 100°C for 45 min. The samples were then dried in a vacuum oven at 70°C for 5 hours to remove the traces of solvents present. Treated surfaces were then sputtered with gold before examination.

Differential Scanning Calorimetry (*DSC*) – DSC measurements were carried out in a TA instrument, USA (Model DSC Q100 V 8.1) to study the melting behavior. The samples of about 6 mg sealed in aluminum pans were heated from –80 to 200°C at a scanning rate of 10°C/min under nitrogen atmosphere. The degree of crystallinity of PP was determined from the heating curve by using standard formula which was discussed earlier by the authors [17, 18].

Mechanical Testing – The dumb-bell shaped specimens of the TPV used for testing were die cut from the compression molded sheet and the testing was done after 24 hours of maturation at room temperature. Tensile strength was measured according to ASTM D418-98A using a universal testing

machine Hounsfield H10KS (UK) at a constant cross-head speed of 500 mm/min. Tension set was performed at room temperature with a stretching condition for 10 minutes at 100% elongation according to the ASTM D412-98 method.

Cyclic Tensile Testing – The tensile testing specimen was used to perform the hysteresis and fatigue life testing of the samples. The loading and unloading cross-head speed of 500 mm/min was maintained. All the values were measured at the room temperature (25°C) in air without any pretreatment. The hysteresis measurements were done in two modes i.e. constant strain amplitude and stepwise increase in strain amplitude.

Overall Crosslink Density (*OCD*) – Equilibrium solvent swelling measurements were carried out on the PP/EOC TPVs to determine the crosslink density of the EOC (ν) in presence of PP [11, 17]. The overall crosslink density was calculated using the modified Flory–Rehner equation [21]. From the degree of swelling, the overall crosslink density was calculated relative to the (EOC+PP) phases and expressed as (ν+PP). The latter was done in order to avoid the need to correct for a part of the PP, being extracted as amorphous PP. A circular piece of 2 mm thickness was made to swell in cyclohexane for about 48 hours to achieve equilibrium swelling condition. Initial weight, swollen weight and de-swollen or dried weight were measured and substituted in the Equation (1):

$$(\nu + PP) = -\frac{1}{V_s} \cdot \frac{\ln(1 - V_r) + V_r + \chi (V_r)^2}{(V_r)^{1/3} - 0.5 V_r} \qquad (1)$$

where ν – number of moles of effectively elastic chains per unit volume of EOC [mol/ml] (crosslink density), (ν+PP) – crosslink density of EOC phase in the presence of PP (overall crosslink density), V_s – molar volume of cyclohexane [cm³/mol], χ – polymer swelling agent interaction parameter, which in this case is 0.306 [11] and V_r – volume fraction of ethylene-octene copolymer in the swollen network, which can be expressed by Equation (2):

$$V_r = \frac{1}{A_r + 1} \qquad (2)$$

where A_r is the ratio of the volume of absorbed cyclohexane to that of ethylene-octene copolymer after swelling.

3. Results and discussion

3.1. Processing characteristics

Mixing torque-time relationship (processing characteristics) of uncrosslinked and dynamically crosslinked blends were recorded from Haake Rheomix. The stabilized torque value is the characteristic feature of the viscous nature of the melt. It clearly indicates that the stabilized torque value increases with increase in rubber (EOC or EPDM) content as shown in Table 3. As mentioned previously (Table 1), EPDM has higher molecular weight and chain entanglement density relative to EOC. Therefore, EPDM macromolecules show higher resistance to the chain conformation and thereby show higher torque values than EOC based blends. In the dynamically vulcanized blends, the processing characteristic is more or less similar to that of corresponding uncrosslinked blends until the curative (peroxide with coagent) is added. When the curative is added, torque value increases, reaches maximum and then decreases before being stabilized. Typical torque-time relationship of 50/50 PP/EOC and PP/EPDM uncrosslinked and

Table 3. Mixing torque values of the uncrosslinked and dynamically crosslinked blends

Compound name	PP/EOC		Compound name	PP/EPDM	
	Maximum torque value after adding curative [N·m]	Torque value at the end of the mixing cycle [N·m]		Maximum torque value after adding curative [N·m]	Torque value at the end of the mixing cycle [N·m]
XC	–	3.5	XD	–	4.0
YC	–	5.3	YD	–	6.8
ZC	–	6.8	ZD	–	11.4
D2XC	7.6	2.5	D2XD	6.9	1.8
D2YC	14.0	7.4	D2YD	14.3	7.2
D2ZC	20.6	17.3	D2ZD	22.7	17.2
D4XC	7.4	1.6	D4XD	7.0	1.2
D4YC	15.2	7.0	D4YD	15.5	6.8
D4ZC	23.3	20.1	D4ZD	25.5	19.8

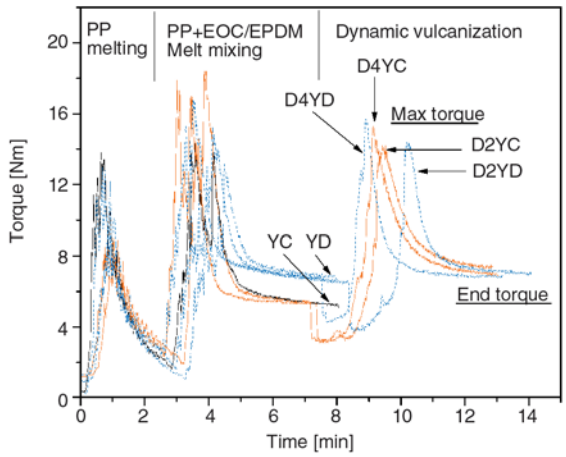

Figure1. Comparative mixing torque-time relationship of 50/50 PP/EOC and PP/EPDM uncrosslinked and dynamically crosslinked blends

dynamically crosslinked blends are shown in Figure 1. The increase in torque is due to the crosslinking occurring in the EOC or EPDM phases. Decrease in torque value after reaching the maximum is expected due to the combined effect of the disintegration of crosslinked EOC or EPDM domains and also by the degradation in the PP phase through β-scission [22]. The maximum torque value after adding the curative and the torque value at the end of the mixing cycle for different compositions are given in the Table 3. Depending on the composition and polymer type, extent of degradation and crosslinking might be resolved. Samples with higher amount of PP (XC and XD) having 75% of PP, suffer severe degradation in PP phase during dynamic vulcanization. Therefore end torque (final torque) value decreases with the addition of curative with respect to uncrosslinked blends. Nevertheless, torque value increases initially after the addition of curative, which may be associated with the crosslinking that takes place in the EOC or EPDM phase. In case of YC and YD blends containing 50% of PP, there exists equal contribution to crosslinking in the rubbery phase and chain-scission in the PP phase. It is worth noting that the maximum torque increases and end torque decreases as a function of curative dosage. In ZC and ZD blends containing 25% of PP curative is mostly consumed by the rubbery phase and overrides the degradation in PP phase. This reflected to increase both the end torque and maximum torque values as a function of curative dosage (within the curative concentration limit). The above results suggest that the maximum torque value increases with increase in rubber content in both the systems (PP/EOC and PP/EPDM).

It is to be noted here that, EPDM based TPVs show lower end torque values than corresponding EOC based TPVs at identical rubber/plastic composition. EPDM is a random terpolymer of ethylene, propylene and diene units and with the addition of peroxide, propylene units undergo chain-scission and/or disproportionation as side reaction apart from the crosslinking in the ethylene units. Hence EPDM based TPVs suffer severe degradation than EOC based TPVs. Apparently, peroxide at the higher curative dosage (4 phr) not only increases the extent of crosslinking in EOC or EPDM phase but also causes significant degradation in the PP phase.

3.2. Morphology

In general, phase morphology of the heterogeneous polymer blends are mainly determined by viscosity ratio, blend ratio and interfacial tension [23]. Several authors [24–27] surveyed the morphology and rheology of various kinds of polyolefin blends with special reference to the varying blend ratios. Figure 2 shows the SEM photomicrographs of 50/50 blend ratio of PP/EOC and PP/EPDM uncrosslinked and dynamically crosslinked blends. In uncrosslinked blends, rubbery phase EOC or EPDM was preferentially extracted and in dynamically crosslinked blends PP phase was preferentially extracted. Both the uncrosslinked compound (YC and YD) results in the formation of co-continuous phase morphology. Depending on the viscosity ratio, various levels of co-continuity exist in the blend compounds. It is clear from the Figures 2a and 2b that the PP/EOC (YC) contributes to have higher percentage of co-continuity than PP/EPDM (YD) blend. Because of higher viscosity ratio in YD, EPDM prefers to exist in dispersed phase. However by dynamic vulcanization, a complete phase transition (inversion) occurs i.e. co-continuous morphology is changed into dispersed phase morphology. The less viscous PP encapsulates the more viscous crosslinked rubber particles to minimize the mixing energy [22, 23]. At equal curative dosage of 2 phr DCP and compositional volume, PP/EPDM TPV shows coarser crosslinked rubber particle size than PP/EOC TPV (Figures 2c and 2d). By increasing the concentration of peroxide (4 phr) in order to increase the crosslink density of

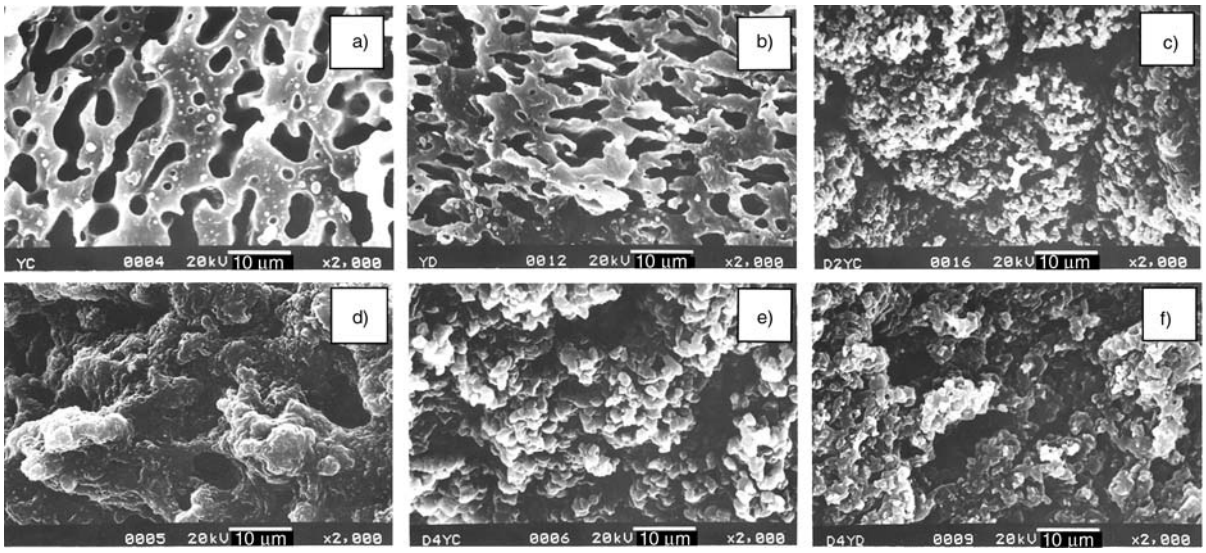

Figure 2. SEM photomicrographs of a) YC (50/50 PP/EOC uncrosslinked) b) YD (50/50 PP/EPDM uncrosslinked) c) D2YC (dynamically vulcanized; 2 phr) d) D2YD (dynamically vulcanized; 2 phr) e) D4YC (dynamically vulcanized; 4 phr) f) D4YD (dynamically vulcanized; 4 phr)

rubber phase, two opposite behaviors have been accounted in the particle size evolution for PP/EOC and PP/EPDM blend. Crosslinked rubber particles size increases in PP/EOC blends, whereas decreases in PP/EPDM blend as a function of peroxide concentration (Figures 2e and 2f). It is well known that, PP undergoes chain-scission with the addition of peroxide. In case of PP/EOC blends when the concentration of peroxide increases from 2 to 4 phr, extent of degradation in the PP phase dominates over crosslinking in the EOC phase. Therefore, it becomes too difficult for a relatively very low viscosity PP matrix (low molecular weight PP) to break-up the crosslinked EOC rubber. But in case of PP/EPDM blends, in addition to the PP-matrix chain-scission, the inherent PP segments in the EPDM also undergo chain-scission which cause to form low molecular weight compound. These low molecular weight compounds have higher tendency towards fine dispersion by lowering the viscosity ratio.

3.3. Thermal properties

DSC measurements were performed to characterize the crystallization and melting behavior of uncrosslinked and dynamically vulcanized blends. Figure 3 shows the DSC cooling and heating curves of 50/50 rubber/plastic blend ratio of uncrosslinked and dynamically vulcanized blends. Table 4 summarizes the relevant thermal parameters as obtained from the DSC scans. It can be seen from the Table 4, that neat PP exhibits a characteristic feature of semi-crystalline polymer with glass transition (T_g), melting temperature (T_m) and crystallization temperature (T_c) at around 1, 165 and 119°C, respectively. Pristine EOC shows a strong β-transition (step in DSC heat capacity traces) due to its movement of octene branch points at –50°C. On contrary, EPDM shows a transition at –45°C due to the relaxation of short chain branch points. But, PP does not show a significant change in β-transition in the DSC traces due to its semi-crystalline characteristics. Both EOC and EPDM show the occur-

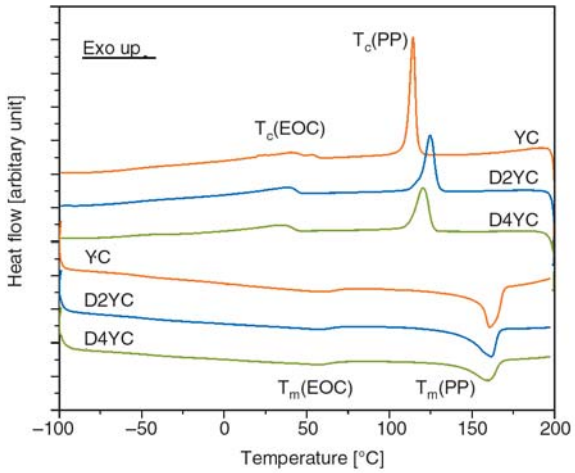

Figure 3. DSC curves of melting endotherm and crystallization exotherm of 50/50 rubber/plastic uncrosslinked and dynamically crosslinked blends. (second heating scan and cooling scan of the blends after subjecting them to same thermal history)

Table 4. Crystallization and melting characteristics of uncrosslinked and dynamically crosslinked blends

Compound name	PP					EOC/EPDM				
	T_g [°C]	T_m [°C]	ΔH_f [J/g]	X_c [%]	T_c [°C]	T_g [°C]	T_m [°C]	ΔH_f [J/g]	X_c [%]	T_c [°C]
PP	1	165	99.32	47.52	119	–	–	–	–	–
EOC	–	–	–	–	–	–50	60	18.9	6.55	45
EPDM	–	–	–	–	–	–45	38	8.2	2.85	20
YC	1	162	48.7	46.63	113	–47	60	7.5	5.17	42
D2YC	2	161	46.5	44.52	124	–46	58	6.4	4.41	40
D4YC	2	160	33.9	32.44	120	–45	58	5.5	3.76	37
YD	0	162	45.8	43.82	114	–43	37	3.6	2.48	19
D2YD	2	161	45.3	43.34	125	–38	33	5.1	3.51	18
D4YD	2	158	45.2	43.22	124	–38	33	4.0	2.75	18

T_g – Glass transition temperature, T_m – Peak melting temperature, ΔH_f – Heat of fusion value, X_c – Percentage crystallinity calculated from heat of fusion data, T_c – Crystallization temperature

rence of T_m and T_c, suggesting the presence of crystalline phase. It is expected that, both EOC and EPDM seem to have long enough ethylene blocks, which are easy to crystallize in a usual manner. However, depending on its inherent molecular architecture T_c of EOC and EPDM are 45 and 20°C respectively.

At 50/50 rubber/plastic blend ratio (YC and YD), T_m, T_c and X_c found to vary significantly for both PP as well as for rubbery component. The possible inter-diffusion and inter-molecular mixing reduces the size and perfectness of crystals and consequently inhibits the crystallization process on either component as also reported by Bielinski *et al*. [28]. The results, therefore, suggest that PP blended with EOC or EPDM needs higher undercooling to crystallize (i.e., rubbery components may depress the crystallization of PP) and correspondingly decrease the T_c. It is worth noting that the addition of rubbery component broadens the melting endotherms of PP phase, which is probably due to the changes in the distribution of crystal lamella thickness.

Upon dynamic vulcanization, significant changes in the thermal properties were observed in both PP and rubbery phases. Apparently, as the peroxide dosage increases from 0 to 4 phr in PP/EOC blend, T_g marginally increases, T_m as well as X_c decrease continuously in the EOC phase due to low degree of chain alignment resulting from predominant crosslinking. As for PP matrix phase, variation in the T_g is marginal whereas T_m and X_c continuously decrease as the curative concentration increases. A similar trend is found for the PP/EPDM TPVs. It is very clear from the Table 4, the extent of decrease in X_c of PP is more pronounced for PP/EOC TPVs as a function of curative concentration i.e., X_c of PP decreased from 46.6 to 32.4% with addition of 4 phr of peroxide. Bulk crystallization temperatures of both the components were found to vary significantly by dynamic vulcanization. As for the rubbery phase, $T_{c(EOC)}$ was found to decrease continuously in PP/EOC TPVs. This may be associated with the prominent crosslinking reaction in the EOC phase which needs higher under-cooling to crystallize. Whereas in case of PP/EPDM TPVs, EPDM undergoes simultaneously crosslinking in the ethylene sequence and chain-scission in the propylene sequence. The combined effect of the above mentioned two competing reactions inconsistently affect the crystallization process of EPDM phase. As the peroxide dosage increases from 0 to 4 phr (with in the given concentration limit), the $T_{c(PP)}$ was found to increase and then decrease for PP/EOC based TPVs. At 4 phr concentration of peroxide, chain scission in the PP phase dominates over the crosslinking effect in the EOC phase. Therefore, the lower molecular weight PP chains have less under-cooling effect to crystallize. But in case of PP/EPDM TPVs, $T_{c(PP)}$ initially increases and then gets stabilized, which is mainly due to the competition between the chain coupling reaction in the polyethylene segments and chain scission reaction in the polypropylene segments in the EPDM phase.

3.4. Mechanical properties

The effect of blend composition on the tensile properties of PP/EOC and PP/EPDM uncrosslinked and dynamically vulcanized blends are compared and shown in Table 5. Comparative stress-strain properties of the blend components are shown in Figures 4a and 4b. Neat PP shows very high tensile strength and poor elongation, a characteristic fea-

Table 5. Comparative physical properties of uncrosslinked and dynamically crosslinked blends

Compound name	Tensile strength [MPa]	Elongation at break [%]	100% modulus [MPa]	Tension set [%]	Overall crosslink density (ν+PP)·10^{-4} [mol/ml][a]
PP	39.6±1.2	16±3	–	–	–
EOC	14.4±0.8	1265±24	2.1±0.2	4±0.2	0.06
EPDM	3.51±0.4	1485±35	0.6±0.1	2.5±0.3	0.19
XC	22.9±2.1	91±11	–	–	40.05
YC	13.2±2.3	155±15	12.9±0.5	36±1.2	8.17
ZC	9.2±1.2	795±21	5.4±0.4	14±0.6	0.38
D2XC	20.1±2.4	16±3	–	–	36.10
D2YC	15.4±1.5	237±12	14.0±0.3	32±0.8	10.12
D2ZC	11.5±1.1	300±15	6.8±0.2	12±0.3	2.58
D4XC	18.3±2.4	14±2	–	–	32.21
D4YC	14.5±1.2	200±8	13.8±0.3	28±0.5	10.32
D4ZC	11.5±0.5	295±12	7.0±0.2	10±0.2	3.72
XD	19.7±1.6	105±10	–	–	46.15
YD	11.9±1.0	117±14	11.9±0.3	28±0.6	13.92
ZD	4.5±0.4	477±18	3.1±0.1	8±0.2	2.91
D2XD	19.5±2.5	17±2	–	–	39.21
D2YD	12.5±1.3	150±13	12.7±0.2	24±0.4	16.84
D2ZD	9.9±0.8	269±15	5.3±0.2	6±0.3	4.92
D4XD	15.4±1.5	93±9	–	–	32.38
D4YD	13.9±0.0	160±16	12.5±0.3	22±0.5	16.21
D4ZD	09.3±0.0	222±19	5.7±0.2	5±0.2	5.94

[a]Standard deviation of overall crosslink density value lies in between 0.1–0.15

ture of a brittle material. On the other hand, EPDM being primarily an amorphous polymer having unreliable amount of crystals due to the crystallizing nature of long chain polyethylene segments shows a typical uncrosslinked elastomer like deformation. The stress-strain behavior of EOC is similar to that of uncrosslinked rubber; however stress gradually increases with increase in strain level. This may be due to the crystallizing tendency of polyethylene segments during stretching (Figure 4a, *inset*). A significant difference was observed in the deformation characteristics of the blends with varying compositions (Figure 4a). Samples XC and XD show necking and yielding region. It may be associated with the distribution and dispersion of rubber particles in inter- and intraspherulitic region of PP matrix to reduce the notch sensitivity and brittle fracture [29]. The yield stress value and the peak broadening are observed when the rubber content increases from 25 to 50% (YC and YD). In case of ZC and ZD, elongation at break increase and modulus and tensile strength increase as compared to YC and YD. The improved rubbery behavior can be explained in terms of morphologi-

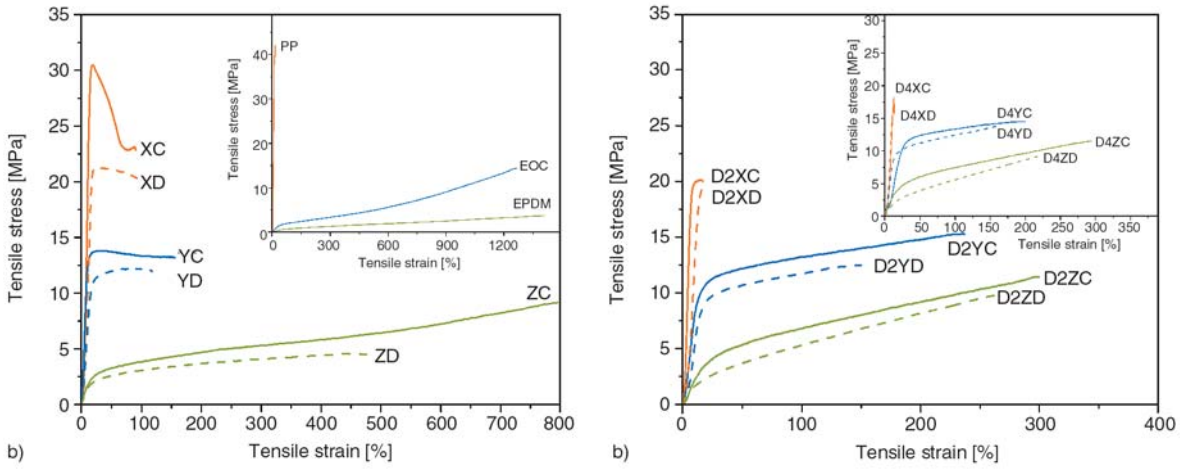

Figure 4. Stress-strain properties of (a) Uncrosslinked blends *Inset: Pristine polymer* (b) Dynamically vulcanized blends with 2 phr concentrations of peroxide *Inset: 4 phr peroxide*

cal evolution (phase transition of EOC or EPDM phase form co-continuous to continuous as the rubbery content increases from 50 to 75% as shown in the earlier sections).

The stress-strain curve of dynamically vulcanized blend with 2 phr concentration of peroxide is shown in Figure 4b. For the compositions D2XC and D2XD, degradation in the PP phase results to show lower stress and strain values. In case of D2YC and D2YD, the nature of the curve significantly changes from plastic to elastic type with the disappearance of necking and yielding. Thereby, dynamically vulcanized samples exhibit improved tensile strength and elongation at break. The above change in the deformation mechanism is mainly associated with the evolution of phase morphology during dynamic vulcanization. Samples with higher rubber content (D2ZC and D2ZD) are more towards the elastic type with increased modulus and tensile strength and lower elongation at break. Furthermore, at higher peroxide dosage (4 phr), D4XC and D4XD show poor tensile and elongation at break values, which may be due to extensive degradation or chain-scission in the PP phase. In case of dynamically vulcanized 50/50 rubber/plastic content (D4YC and D4YD), marginal decrease in both tensile and elongation values suggest that, chain-scission in PP dominates over crosslinking in EOC or EPDM phase. Interestingly, not much difference is observed in the stress-strain values with increase in the curative dosage for samples with higher rubber content (ZC and ZD) (Figure 4b, *inset graph*).

When comparing the behavior of PP/EOC and PP/EPDM samples, in all the cases EOC based uncrosslinked and dynamically vulcanized blends exhibit better physical properties than PP/EPDM samples at identical composition. Since EPDM is an ethylene propylene diene random terpolymer, part of the propylene units undergoes chain-scission or degradation while using peroxide as curative. During dynamic vulcanization, as the concentration of curative increases from 0 to 4 phr, a higher level of degradation in the PP phase is coupled with the chain-scission in the PP segments in the EPDM polymer in PP/EPDM blends. Thereby PP/EPDM TPVs lose their mechanical strength despite containing the finest vulcanized rubber particles. Therefore, it is expected that dynamically vulcanized blends of PP/EPDM depict inferior physico-mechanical properties than PP/EOC TPVs. From the DSC and SEM analyses, it was found that EOC containing small crystals have good affinity and finely dispersed particles in the PP matrix phase. On the other hand, EPDM itself contains small crystals but its crystallinity might be too low (due to high degree of chain entanglement density) to form an effective reinforcing characteristics. Although mechanical properties are found to be superior for PP/EOC blends, set properties are better for PP/EPDM blends.

Tension set and overall crosslink density (OCD) values show a good correlation for both PP/EOC and PP/EPDM uncrosslinked and dynamically crosslinked blends. As the concentration of peroxide increases form 0 to 4 phr (in both the cases), samples with higher amount of PP suffer from chain scission and hence OCD value decreases continuously. However samples with 50 and 75% rubber content, OCD continuously increases. Particularly, the latter (75% rubber content) shows significant increase in the OCD values with increase in peroxide concentration. These changes are associated with the chain coupling reactions in the rubbery phase. As a mater of fact, EPDM based blends show higher OCD values as compared to EOC based compounds. In case of EPDM based samples, the presence of natural physical entanglements at their characteristics network density would cause an increase in number of effective crosslink points per molecule (crosslink density) and correspondingly improve the set properties.

3.5. Hysteresis

In general, hysteresis measurements give information about the structural changes of the material under cyclic deformation. The samples are subjected to uniaxial tensile deformation at a constant speed of 500 mm/min and the deformation was removed at the same speed. In general, due to the viscoelastic nature of the polymeric materials, the energy applied may not be balanced with energy released i.e., the stretching and recoiling curves form a closed loop called as hysteresis loop. The hysteresis loop of cyclic tensile curves of 50/50 rubber/plastic blend ratio of uncrosslinked and dynamically crosslinked blends at constant strain of 100% are shown in Figures 5a and 5b. During stretching, a 50:50 blend ratio of PP and rubbery components exhibit the stress-strain behavior, a

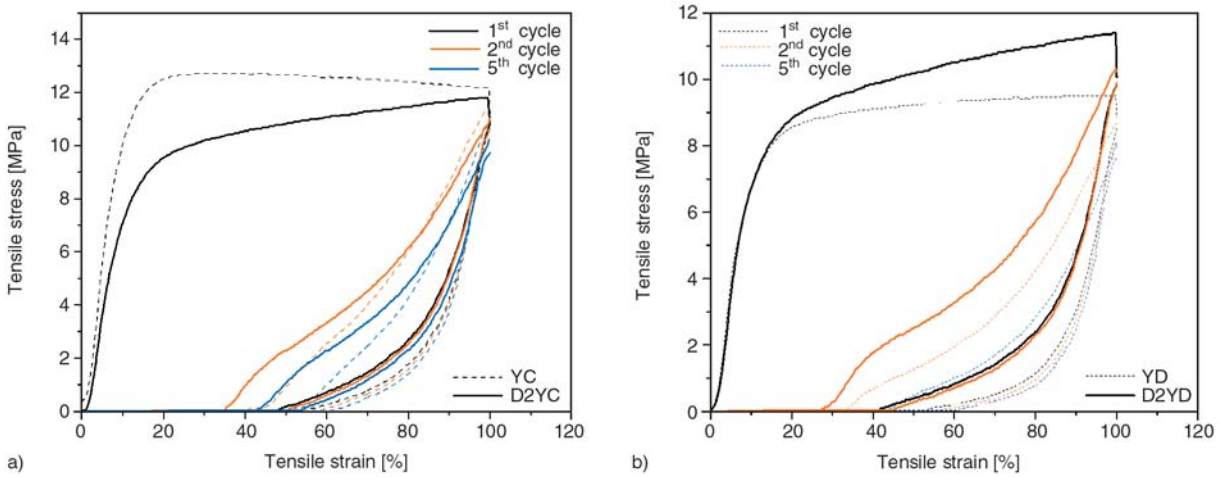

Figure 5. Stress-strain hysteresis loops during cyclic tension at constant strain of 100% (a) 50/50 PP/EOC uncrosslinked and dynamically crosslinked blends (b) 50/50 PP/EPDM uncrosslinked and dynamically crosslinked blends

Table 6. Results of hysteresis test at constant strain of 100%

Compound name	Residual strain [%]			Max. stress [MPa]		
	1st cycle	2nd cycle	5th cycle	1st cycle	2nd cycle	5th cycle
YC	41.0	43.0	51.1	11.8	11.2	10.8
YD	35.0	37.5	44.2	9.4	8.7	8.0
D2YC	34.3	36.4	43.3	11.8	10.9	10.2
D2YD	27.8	29.5	29.0	11.3	10.3	10.1

characteristic feature of a thermoplastic material: an initial linear elastic behavior followed by gradual yielding [30]. Compared to uncrosslinked blends, TPVs exhibit steady strain hardening effect immediately after yielding. According to Soliman *et al*. [31] the deformation mechanism of PP/EPDM TPVs (as shown in Figure 6) is the combination of matrix yielding and buckling of yielded PP matrix by the recovering tendency of crosslinked rubbery particles. During stretching, PP acts as glue between the crosslinked EPDM particles and part of the PP fractions undergo yielding in the direction perpendicular to the load. During recovery, the yielded PP fraction is partially pulled back by the recovering tendency of the crosslinked particles. During recoiling, the residual strain or permanent set is observed due to matrix yielding. All the samples exhibit a decrease in the maximum stress level which can be explained by strain softening effect. It is clear from the Table 6 and Figure 5; significant softening is occurred in the first cycle followed by gradual softening effect with increase in number of cycles. A plausible mechanism for the observed changes could be due to disentanglement and slippage of polymer chains as a consequence of matrix yielding or shear banding. In both the cases, (PP/EOC and PP/EPDM) the dynamically vulcanized blends decrease the setting behavior and lower the energy loss, a characteristics feature of elastomeric material. Furthermore, comparing the hysteresis behavior of two material classes, D2YC and D2YD, it is seen that latter exhibits less setting behavior in combination with lower energy loss. It may be due to the inherent physical crosslinks by higher chain entanglement density.

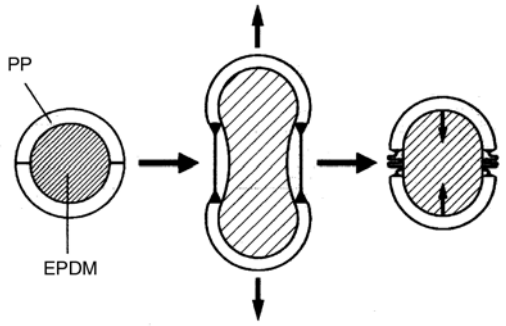

Figure 6. Deformation mechanism of TPVs suggested by Soliman *et al*. [31]

Samples have been subjected to stepwise increasing strain test (SIST) to understand the structural changes of the material as a function of cyclic fatigue straining. Figures 7a and 7b demonstrate the results of the SIST of uncrosslinked and dynamically crosslinked blends subjected to straining at predetermined values of 20, 50, 100, 150 and 180% at a same speed of 500 mm/min. From the

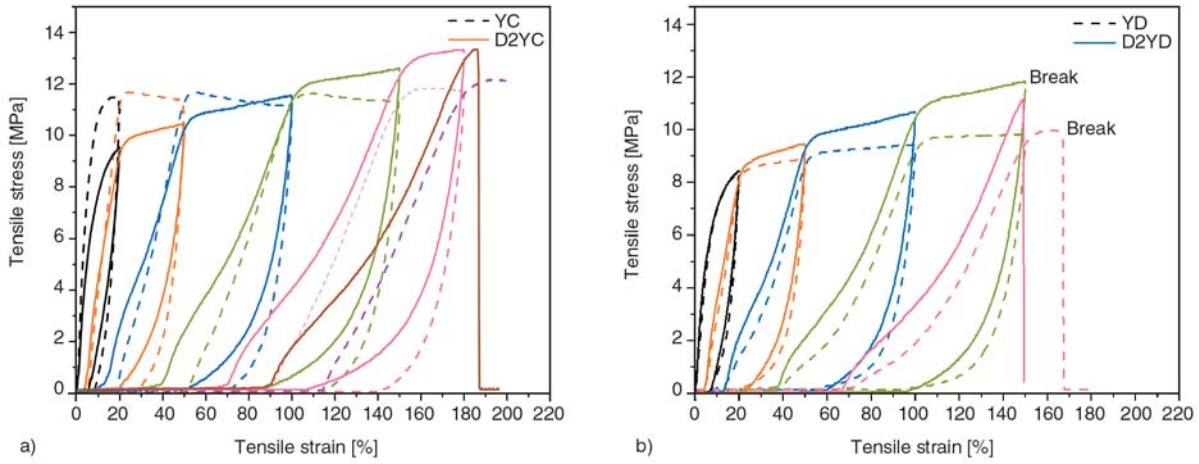

Figure 7. Stepwise hysteresis loops during cyclic tension (a) 50/50 PP/EOC uncrosslinked and dynamically crosslinked blends (b) 50/50 PP/EPDM uncrosslinked and dynamically crosslinked blends

Figures 7a and 7b, it is clear that the residual strain or irreversible strain is smaller in low strain region but becomes significantly higher at higher strain level. Therefore, the TPVs exhibit rubber like elastic deformation in the low strain region. But with increasing the strain level, elastic deformation is superimposed with irreversible plastic deformation. Although, PP/EPDM based uncrosslinked blend and dynamically blends exhibit lower setting tendency and energy loss than corresponding PP/EOC based blends but with poor fatigue resistance (failed before completing fourth cycle). The improved fatigue behavior of D2YC can be explained by the fact of better interfacial adhesion between the blend components.

4. Conclusions

The morphological, thermal and mechanical results are interpreted in terms of the balance between the crosslinking in the EOC and EPDM phases versus degradation in the PP phase. It is worth noting that, PP segments in the EPDM rubber might also undergo chain-scission and/or disproportionation reaction during dynamic vulcanization. So the obtained results are indeed the balance of the above mentioned reactions in the constituent polymers. The morphology of PP/EOC and PP/EPDM blends indicate a two phase morphology in which the rubber phase is dispersed in continuous PP matrix at lower rubber/plastic blend ratio and followed by phase inversion with increase in rubber/plastic blend ratio. The 50/50 composition of rubber/plastic shows co-continuous phase morphology. However, after dynamic vulcanization all the samples exhibit a dispersed phase morphology in which crosslinked rubber particles are dispersed in continuous PP matrix. The dispersion characteristics of the dispersed crosslinked rubber phase are mainly influenced by the melt viscosity ratio, shear rate, curative dosage and the rubber content.

The crystallinity of the PP phase in TPVs is more or less comparable for both the systems employed. Therefore the stress-strain response of the PP/EOC and PP/EPDM dynamically crosslinked blends at identical composition is found to depend on the dispersion characteristics of the crosslinked rubber phase. Dynamically vulcanized blends having higher rubber/plastic ratio show thermoplastic elastomeric characteristics, whereas those having higher plastic/rubber ratio show poor mechanical properties due to degradation in the PP phase. When compared to the conventional PP/EPDM TPVs, PP/EOC TPVs show lower viscosity and elasticity in the melt state and better physico-mechanical properties in the solid state. Hystersis measurements have been found to be a useful tool to evaluate the structural changes during dynamic deformation and fatigue analysis. Dynamically vulcanized 50/50 rubber/ plastic blend shows lower energy loss and better set properties. Although, PP/EPDM TPVs show lesser relaxation than corresponding PP/EOC TPVs but show poor fatigue characteristics.

In short, PP/EOC shows better mechanical, and thermal properties which may be due to better interfacial interaction and unique molecular microstructure of the EOC phase. In addition to lower cost,

EOC are supplied in free pellets which allow for both batch and continuous production of TPVs. So, peroxide cured PP/EOC TPVs combine better processing characteristics with superior performance in the solid state. Hence, peroxide cured PP/EOC can be considered as a potential alternative to the conventional PP/EPDM TPVs.

Acknowledgements

The authors are grateful to the Council of Scientific and Industrial Research (CSIR), New Delhi, India for financial assistance.

References

[1] Paul D. R., Bucknall C. B.: Polymer blends. Wiley, New York (2000).

[2] Karger-Kocsis J.: Thermoplastic rubbers via dynamic vulcanization. in 'Polymer blends and alloys' (eds.: Shonaike G. O., Simon G. P.) Marcel Dekker, New York (1999).

[3] De S. K., Bhowmick A. K.: Thermoplastic elastomers from rubber plastic blends. Horwood, London (1990).

[4] Coran A Y., Patel R., Williams D.: Rubber-thermoplastic compositions. Part V. Selecting polymers for thermoplastic vulcanizates. Rubber Chemistry and Technology, **55**, 116–136 (1982).

[5] Naskar K.: Thermoplastic elastomer based on PP/EPDM blends by dynamic vulcanization – Review. Rubber Chemistry and Technology, **80**, 504–510 (2007).

[6] Walton K. L.: Metallocene catalysed ethylene/alpha olefin copolymers used in thermoplastic elastomers. Rubber Chemistry and Technology, **77**, 552–568 (2004).

[7] McNally T., McShane P., Nally G. M., Murphy W. R., Cook M., Miller A.: Rheology, phase morphology, mechanical, impact and thermal properties of polypropylene/metallocene catalysed ethylene 1-octene copolymer belnds. Polymer, **43**, 3785–3793 (2002).
DOI: 10.1016/S0032-3861(02)00170-2

[8] Da Silva A. L. N., Rocha M. C. G., Coutinho F. M. B., Bretas R., Scuracchio C. J.: Rheological, mechanical, thermal, and morphological properties of polypropylene/ethylene-octene copolymer blends. Journal of Applied Polymer Science, **75**, 692–704 (2000).
DOI: 10.1002/(SICI)1097-4628(20000131)75:5<692::AID-APP12>3.0.CO;2-Y

[9] van Duin M.: Recent developments for EPDM-based thermoplastic vulcanisates. Macromolecular Symposia, **233**, 11–16 (2006).
DOI: 10.1002/masy.200690006

[10] Dluzneski P. R.: Peroxide vulcanization of elastomers. Rubber Chemistry and Technology, **74**, 451–490 (2001).

[11] Naskar K., Noordermeer J. W. M.: Dynamically vulcanized PP/EPDM blends: Effects of different types of peroxide on the properties. Rubber Chemistry and Technology, **76**, 1001–1018 (2003).

[12] Naskar K., Noordermeer J. W. M.: Dynamically vulcanized PP/EPDM blends: Effects of multifunctional peroxides as crosslinking agents. Rubber Chemistry and Technology, **77**, 955–971 (2004).

[13] Naskar K., Gohs U., Wagenknecht U., Heinrich G.: PP-EPDM thermoplastic vulcanisates (TPVs) by electron induced reactive processing. Express Polymer Letter, **3**, 677–683 (2009).
DOI: 10.3144/expresspolymlett.2009.85

[14] Basuli U., Chaki T. K., Naskar K.: Influence of Engage® copolymer type on the properties of engage/silicone rubber-based thermoplastic dynamic vulcanizates. Express Polymer Letters, **2**, 846–854 (2008).
DOI: 10.3144/expresspolymlett.2008.99

[15] Naskar K., Chatterjee K.: Development of thermoplastic elastomers based on maleated ethylene propylene rubber and polypropylene by dynamic vulcanization. Express Polymer Letters, **1**, 527–534 (2007).
DOI: 10.3144/expresspolymlett.2007.75

[16] Lai S-M., Chin F-C., and Chiu T-Y.: Fracture behaviors of PP/mPE thermoplastic vulcanizate via peroxide crosslinking. European Polymer Journal, **41**, 3031–3041 (2005).
DOI: 10.1016/j.eurpolymj.2005.06.003

[17] Babu R. R., Singha N. K., Naskar K.: Studies on the influence of structurally different peroxides in polypropylene/ethylene alpha olefin thermoplastic vulcanizates (TPVs). Express Polymer Letters, **2**, 226–236 (2008).
DOI: 10.3144/expresspolymlett.2008.27

[18] Babu R. R., Singha N. K., Naskar K.: Dynamically vulcanized blends of polypropylene and ethylene octene copolymer: Influence of various coagents on mechanical and morphological characteristics. Journal of Applied Polymer Science, **113**, 3207–3221 (2009).
DOI: 10.1002/app.30000

[19] Babu R. R., Singha N. K., Naskar K.: Melt viscoelastic properties of peroxide cured polypropylene-ethylene octene copolymer thermoplastic vulcanizates. Polymer Engineering and Science, **50**, 455–467 (2010).
DOI: 10.1002/pen.21553

[20] Babu R. R., Singha N. K., Naskar K.: Effects of mixing sequence on peroxide cured polypropylene (PP)/ethylene octene copolymer (EOC) thermoplastic vulcanizates (TPVs). Part I. Morphological, mechanical and thermal properties Journal of Polymer Research, in press (2010).
DOI: 10.1007/s10965-009-9354-z

[21] Flory P. J., Rehner J. J.: Statistical mechanics of cross-linked polymer networks. II. Swelling. Journal of Chemical Physics, **1**, 521–526 (1943).
DOI: 10.1063/1.1723792

[22] Varghese S., Alex S., Kuriakose B.: Natural rubber-isotactic polypropylene thermoplastic blends. Journal of Applied Polymer Science, **92**, 2063–2068 (2004).
DOI: 10.1002/app.20077

[23] Harrats S., Thomas S., Groeninckx G.: Micro and nano structured multiphase polymer blend systems: Phase morphology and interface. CRC Press, Boca Raton (2006).

[24] Paul D. R., Newman S.: Polyolefin blends: Rheology, melt mixing, and applications in polymer blends. Academic Press, New York (1978).

[25] D'Orazio L., Mancarella C., Martuscelli E., Polato F.: Polypropylene/ethylene-co-propylene blends: Influence of molecular structure and composition of EPR on melt rheology, morphology and impact properties of injection-moulded samples. Polymer, **32**, 1186–1194 (1991).
DOI: 10.1016/0032-3861(91)90220-D

[26] Prut E. V., Erina N. A., Karger-Kocsis J., Medintseva T. I.: Effects of blend composition and dynamic vulcanization on the morphology and dynamic viscoelastic properties of PP/EPDM blends. Journal of Applied Polymer Science, **109**, 1212–1220 (2008).
DOI: 10.1002/app.28158

[27] Da Silva A. L. N., Tavares M. I. B., Politano D. P., Coutinho F. M. B., Rocha M. C. G.: Journal of Applied Polymer Science, **66**, 2005–2014 (1997).
DOI: 10.1002/(SICI)1097-4628(19971205)66:10<2005::AID-APP17>3.0.CO;2-2

[28] Bielinski D. M., Ślusaraki L., Wlochowicz A., Ślusarczyk C., Douillard A.: Some aspect of isotactic polypropylene crystallization in an ethylene-propylene-diene rubber matrix. Polymer International, **44**, 161–173 (1997).
DOI: 10.1002/(SICI)1097-0126(199710)44:2<161::AID-PI837>3.0.CO;2-T

[29] Martuscelli E., Silvestre C., Abat G.: Morphology, crystallization and melting behavior of films of isotactic polypropylene blended with ethylene-propylene copolymers and polyisobutylene. Polymer, **23**, 229–237 (1982).
DOI: 10.1016/0032-3861(82)90306-8

[30] Boyce M. C., Yeh O., Socrate S., Kear K., Shaw K.: Micromechanics of cyclic softening in thermoplastic vulcanizates. Journal of Mechanics and Physics of Solids, **49**, 1343–1360 (2001).
DOI: 10.1016/S0022-5096(00)00077-6

[31] Soliman M., Dijk M. V., Es M. V., Shulmeister V.: Deformation mechanism of thermoplastic vulcanisates investigated by combined FTIR and stress-strain measurements. in 'Proceedings of ANTEC '99, New York, USA' vol 2, 1947–1954 (1999).

eXPRESS Polymer Letters Vol.4, No.4 (2010) 210–216
Available online at www.expresspolymlett.com
DOI: 10.3144/expresspolymlett.2010.27

Effect of consolidation on the flexural creep behaviour of all-polypropylene composite

*A. Izer, T. Bárány**

Department of Polymer Engineering, Budapest University of Technology and Economics, H-1111 Budapest, Műegyetem rkp. 3., Hungary

Received 21 December 2009; accepted in revised form 3 February 2010

Abstract. The long-term viscoelastic behaviour of self-reinforced polypropylene composites (SRPPC) was studied by short-term flexural creep tests at different temperatures. As reinforcement a fabric, woven from highly stretched split PP yarns, whereas as matrix materials α and β crystal forms of isotactic PP homopolymer and random copolymer (with ethylene) were selected and used. The composite sheets were produced by film-stacking method and compression moulded at different processing temperatures (5, 20, 35°C above the melting temperatures of the matrices) keeping the holding time and pressure constant. The manufactured specimens were subjected to isothermal creep tests at different temperatures ranging from –20 to 80°C under an applied load. The time-temperature superposition principle was verified for the creep data. An Arrhenius type relationship described the shift data obtained from the creep tests. It was found, that with improving consolidation (increasing processing temperature) the creep compliance decreased and good correlation was found between creep compliance and density/peel strength.

Keywords: *polymer composites, self-reinforced composite, PP, creep*

1. Introduction

Under steady loading components (especially polymers at room temperature) can slowly deform, a phenomenon called creep. When a plastic material is loaded with a constant load, it deforms continuously with time. This time dependent behaviour of materials (viscoelasticity) is an important characteristic of polymers. To know this long-term behaviour of polymers is essential to estimate their life-time under load. Although creep in an anisotropic, multi-phase system, like composites, is very complex, the analysis of creep properties is important for the use of composites in long-term applications. This may be more significant in self-reinforced polymer composites than in classic materials reinforced by glass or basalt fibre, where not only the matrix but the reinforcement is made of polymer. Note that in comparison to the classical composites self-reinforced composites have some advantages in addition to the good mechanical properties: easy and fully recyclability and low density (the same as those of the matrix materials) [1–8].

Earlier works have shown that the creep behaviour of PP fibre reinforced PP composites depends strongly on stress, temperature, void content, and fibre loading [9–11]. It was concluded, that creep resistance decreases if temperature or stress rises. Several other studies investigated the influence of adhesion and density of the composites on the creep behaviour [12–14]. With increasing consolidation (lower void content) the resistance to creep increases.

The great drawback of the creep test is the long time requirement. But a number of observations suggest that the effects of time and temperature are

*Corresponding author, e-mail: barany@pt.bme.hu

equivalent [15, 16]. The influence of high temperature and long time has similar effect on the polymer material. With shifting the single creep curves (measured at different testing temperatures) together (to a selected reference temperature) a master curve can be created. This time-temperature superposition method (TTS) is able to predict the long-term properties of the material from short time creep tests at higher temperature [17–19]. The relation between temperature and the shift factor can generally be described by the Arrhenius Equation (1):

$$\ln a_T = \frac{E}{R}\left(\frac{1}{T} - \frac{1}{T_0}\right) \quad (1)$$

where a_T is the horizontal shift factor, R is the universal gas constant, E is the activation energy, T_0 is the reference temperature and T is the experimental temperature. The Arrhenius equation relates the horizontal shift factor with temperature [20].

Another commonly used empirical equation for TTS that relates a shift in temperature with a shift in time is the Williams-Landel-Ferry (WLF) Equation (2):

$$\ln a_T = -\frac{C_1(T - T_0)}{C_2 + (T - T_0)} \quad (2)$$

where C_1 and C_2 are constants, and T and T_0 are the experimental and reference temperatures. The WLF equation was found empirically to describe the frequency dependence of glass transition temperature in amorphous polymers [20].

In this work, the effect of consolidation of the self-reinforced composite on the creep behaviour was investigated. The applicability of TTS principle to short term creep data was verified in order to predict the long-term creep response of SRPPC.

2. Materials, their processing and testing

2.1. Materials

A plain woven fabric (Stradom S. A., Czestochowa, Poland) composed of highly stretched split PP tapes with a nominal weight of 180 g/m^2 (the thickness is approximately 180 μm) was selected and used as reinforcement. The reinforcing tape has a melting temperature of T_m = 172.4°C (determined by DSC), and a tensile strength of 465±32 MPa (measured on a single tape).

Three kinds of PP were used as matrix materials: i) β form of isotactic PP homopolymer (TIPPLEN H388F, TVK Nyrt., Tiszaújváros, Hungary); ii) random PP copolymer (TIPPLEN R351F TVK Nyrt., Tiszaújváros, Hungary), and iii) β form of the latter. The manufacturing and properties of the matrix films was detailed elsewhere [21]. The melting temperature value of the β-modification was clearly below that of the corresponding α-version, as expected.

2.2. Composite preparation

The matrix films (9 layers) and the reinforcing woven fabrics (8 plies) were laminated according to film-stacking method. Since the properties of the fabrics showed some directional anisotropy, they were assembled adopting a cross-ply lay-up to make the resulting sheets orthotropic. Self-reinforced PP composite (SRPPC) sheets with a thickness of 2.5 mm and a nominal reinforcement (i.e. α-PP fabric) content of 50 wt% (note that this reinforcing content is substantially lower than in case of the commercial products (Curv®, Pure®)) were produced by compression moulding of a film-stacked package at 7 different processing temperatures. They are selected at 5–35°C above the relevant matrix melting temperature. For the latter the DSC melting peak was considered [21]. The consolidation process took place as follows: after heating up the moulds, the film-stacked package was inserted and held for 30 s without pressure and for 90 s under a pressure of 7 MPa, and then it was cooled to 50°C with a cooling rate of 7.5°C/min and demoulded. It is noteworthy that the holding time at processing temperature was kept as short and low, respectively, as possible to prevent shrinkage (relaxation) of the fibres.

2.3. Specimens and their testing

Short-time flexural creep tests were performed using three-point bending mode at different temperatures, ranging from –20 to 80°C, in a DMA Q800 apparatus (TA Instruments, New Castle, USA). In this temperature range, isothermal creep tests were run on the specimens with a stepwise temperature increment of 10°C. Prior to the creep measurement, each specimen was equilibrated for

5 min. at each temperature and then the flexural creep behaviour was tested for 30 min, under a constant load of 5 MPa. Specimens of dimensions 60×15×2.5 mm^3 (length × width × thickness) were used for creep tests. For creep studies, the average of three statistically relevant creep data has been reported.

3. Results and discussion

The flexural creep behaviour of β-rPP-based composites (compression moulded at different temperatures) as a function of time at different testing temperatures is shown in Figures 1–3. It can be clearly seen from the results that with increasing temperature the creep compliance increases (due to increasing polymer chain mobility). With increasing hot pressing temperature, the SRPPCs have higher resistance to creep, particularly at higher testing temperatures. Recall that with increasing hot pressing temperature the consolidation improves and at the highest processing temperature a significant transcrystalline layer forms between the reinforcement and the matrix [21]. Better consolidation provides better mechanical properties, e.g. flexural stiffness and decreases creep compliance.

Figure 4a and 4b show the creep compliance of α-rPP and β-PP at different processing temperatures (determined at 1000 s), as a function of the testing temperature. It can be seen that between –20 and 30°C, there is no significant change in the creep compliance of the SRPPCs with different degrees of consolidation. To compare the composite made at T_m+5°C with the composite made at optimum temperature (T_m+20°C) it can be concluded, that the creep compliance of the well consolidated composite decreases in the whole testing temperature range. Further increase of processing temperature caused no change in the consolidation, clear transcrystalline layer formed between matrix and reinforcement, which decreases further the creep compliance particularly above testing temperature of 30°C. The same tendency can be observed for β-rPP composites as well.

The logarithm of time and temperature has similar effect (based on thermomechanical curves), what is the well known reduction scheme of time-temperature superposition. Therefore single-step short-term creep tests can be further analyzed by superposing

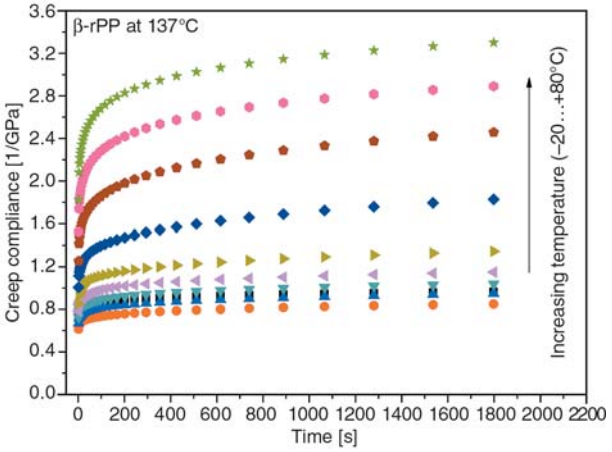

Figure 1. Creep compliance (between –20 and 80°C) of β-rPP composite processed at 137°C

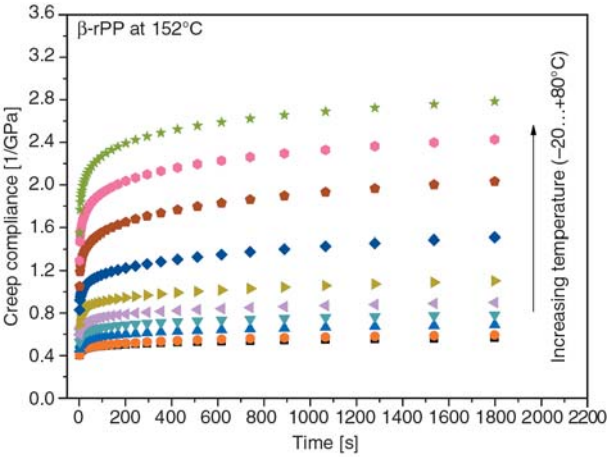

Figure 2. Creep compliance (between –20 and 80°C) of β-rPP composite processed at 152°C

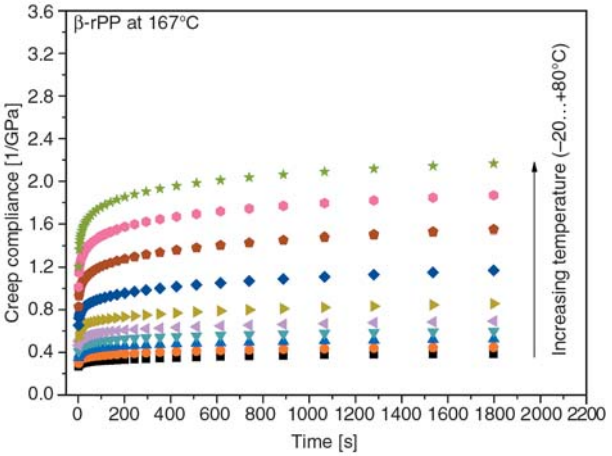

Figure 3. Creep compliance (between –20 and 80°C) of β-rPP composite processed at 167°C

(shifting) the compliance-time data onto master curves, which represent long-term creep behaviour of the material. Generally, from the master curves the behaviour of polymer can be traced over much wider periods of time than those determined exper-

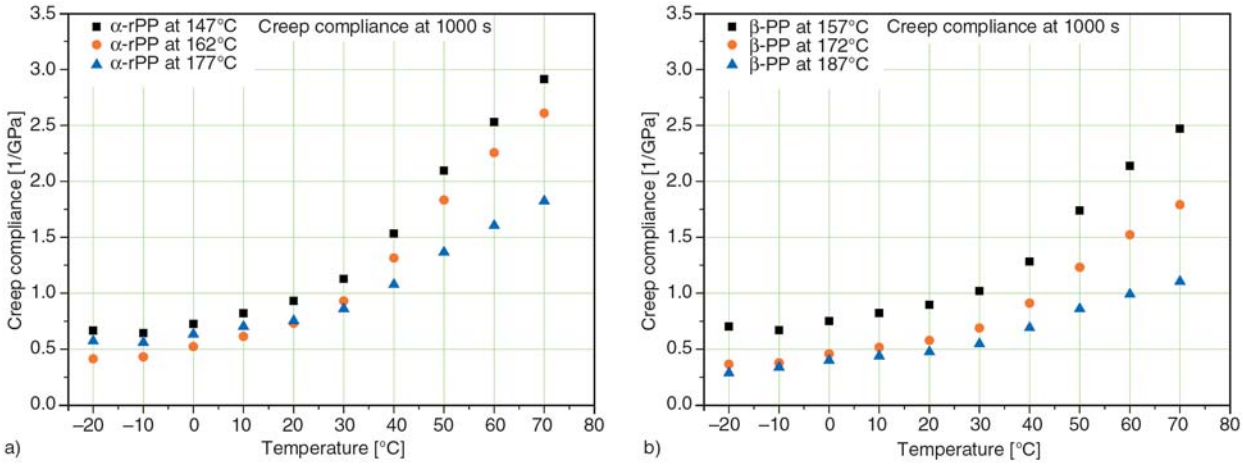

Figure 4. Creep compliance (at 1000 s) of α-rPP-based (a) and β-PP-based (b) composite

imentally. Figures 5–7 show the creep compliance master curves for different composites. The reference temperature was chosen at 30°C in each case. It can be clearly seen, that with increasing processing temperature the creep compliance decreases.

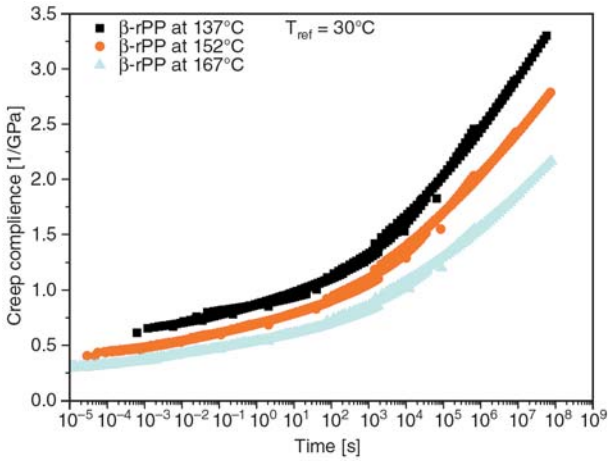

Figure 5. Creep compliance master curves of β-rPP-based composites

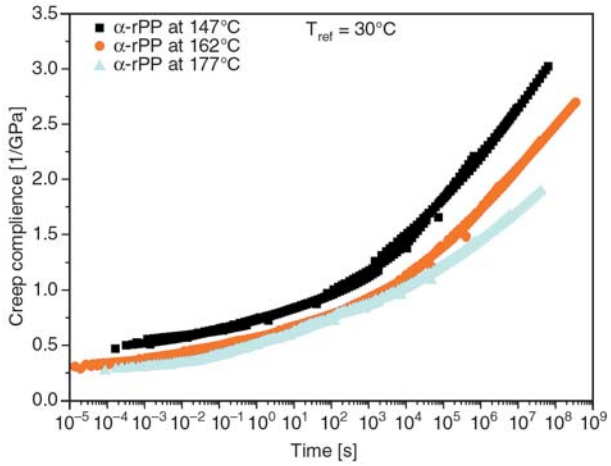

Figure 6. Creep compliance master curves of α-rPP-based composites

Since the current creep test was performed under a small constant load (5 MPa) that can result in a small deformation in the SRPPCs, i.e. the stress is not high enough to cause significant elongation, therefore the consolidation and adhesion between matrix and reinforcement seem to influence the time-dependent deformation. So, the achieved results can be explained by the change of consolidation/adhesion of SRPPCs with increasing hot pressing temperature.

Since the main influence on the creep compliance is the consolidation and adhesion – concluded before; and the peel strength and density reflect well the consolidation, therefore good correlation can be expected between these parameters (these values were described in detail elsewhere [21]) and the creep compliance. Figure 8 shows the creep compliance as a function of peel strength. The value of creep compliance at 1000 s was chosen (according to T_{ref} = 30°C). With increasing peel strength (bet-

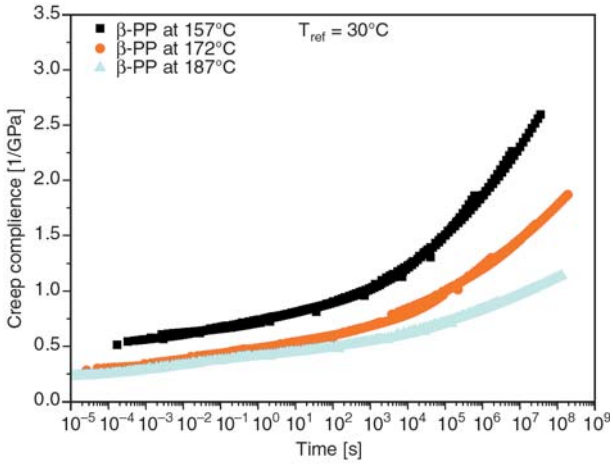

Figure 7. Creep compliance master curves of β-PP-based composites

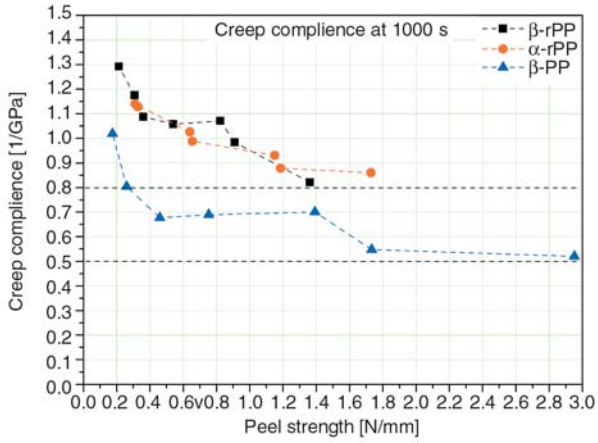

Figure 8. Creep compliance as a function of peel strength for different composites

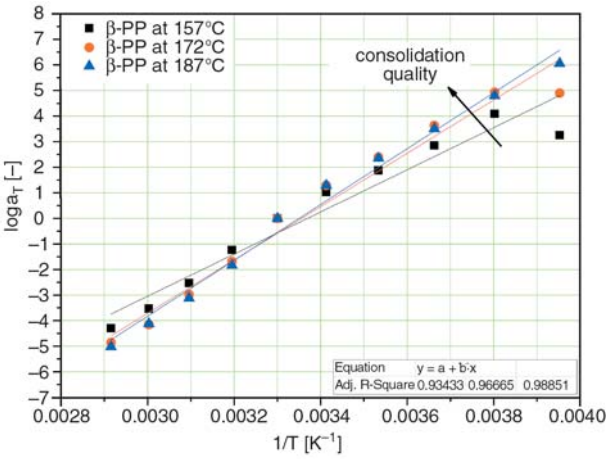

Figure 10. The shift factor follow the Arrhenius equation in the case of β-PP composite

ter consolidation), the creep compliance decreases as expected. It can be seen that each curve tends to a 'saturation' value, i.e. to a creep compliance limit, what might be the theoretical minimum for the given SRPPC. This value is 0.8 1/GPa for rPP-based composites and 0.5 1/GPa for β-PP-based composites.

Many authors explain the creep compliance difference with the change of void content, i.e. with the change of density. Figure 9 shows the creep compliance as a function of density of different matrix based SRPPCs. The values of creep compliance at 1000 s were chosen as before. With increasing processing temperature, the density increases (better consolidation, lower void content), and the creep compliance decreases, as expected. The change is approximately linear, with good tendency.

The shift factor a_T is the extent of shift along the time scale to merge the single creep curves measured at different temperatures into a master curve. The reference temperature was taken as 30°C.

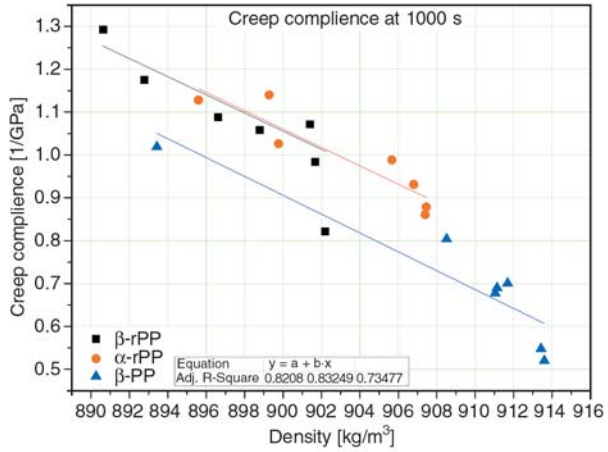

Figure 9. Creep compliance as a function of the density

Because PP is a semicrystalline polymer, therefore it is expected to follow an Arrhenius equation for the major transitions. Figure 10 shows the shift factors as a function of inverse of temperature. It can well be seen, that the shift data can well be described by the Arrhenius equation. Note that, the T_g of the composites is at 0°C in the case of iPP based composites and at –15°C in the case of rPP based composites measured by DMA in our earlier work [8]. The linear regression lines are also shown in Figure 10.

One can see that with increasing consolidation (increasing processing temperature), the activation energy also increases. The activation energy of the deformation process was calculated from the slope of the regression curves (Equation (1)). The activation energy values are listed in Table 1. This data are in harmony with other works [17, 20, 22, 23]. One can see that with increasing activation energy the creep compliance decreases.

Table 1. The activation energy of different SRPPCs

	E_a [kJ/mol]
β-rPP at 137°C	110.6
β-rPP at 152°C	169.7
β-rPP at 167°C	183.8
α-rPP at 147°C	114.4
α-rPP at 162°C	183.1
α-rPP at 177°C	185.0
β-PP at 157°C	133.5
β-PP at 172°C	175.4
β-PP at 187°C	186.9

4. Conclusions

The goal of this paper was to study the effect of consolidation effect on the creep behaviour of different SRPPCs. Single-step short-term creep tests were made on SRPPCs having different consolidation quality, and the creep compliance was superposed onto a master curve. Based on the results it can be concluded, that the creep resistance of the SRPPCs decreases with increasing testing temperature, due to the rising chain mobility at higher temperature. This effect is remarkable above room temperature. The creep resistance strongly depends on the consolidation quality of the composites. From the short-term flexural creep response, the long-term creep behaviour of the SRPPC could be predicted. The main effect on the creep compliance at applied low load is the consolidation. There are good correlations between creep compliance and density or peel strength. The theoretical creep compliance for best consolidated rPP based composite is app. 0.8 1/GPa and for β-PP composite is app. 0.5 1/GPa. An Arrhenius type relationship describes well the time-temperature superposition data.

5. Acknowledgements

The authors want to thank the Hungarian Scientific Research Fund (OTKA K75117). T. Bárány is thankful for the János Bolyai Research Scholarship of the Hungarian Academy of Sciences.

References

[1] Hine P. J., Ward I. M., Jordan N. D., Olley R., Bassett D. C.: The hot compaction behaviour of woven oriented polypropylene fibres and tapes. I. Mechanical properties. Polymer, **44**, 1117–1131 (2003).
DOI: 10.1016/S0032-3861(02)00809-1

[2] Bhattacharyya D., Maitrot P., Fakirov S.: Polyamide 6 single polymer composites. Express Polymer Letters, **3**, 525–532 (2009).
DOI: 10.3144/expresspolymlett.2009.65

[3] Alcock B., Cabrera N. O., Barkoula N. M., Loos J., Peijs T.: The mechanical properties of unidirectional all-polypropylene composites. Composites Part A: Applied Science and Manufacturing, **37**, 716–726 (2006).
DOI: 10.1016/j.compositesa.2005.07.002

[4] Alcock B., Cabrera N. O., Barkoula N-M., Spoelstra A. B., Loos J., Peijs T.: The mechanical properties of woven tape all-polypropylene composites. Composites Part A: Applied Science and Manufacturing, **38**, 147–161 (2007).
DOI: 10.1016/j.compositesa.2006.01.003

[5] Houshyar S., Shanks R. A.: Morphology, thermal and mechanical properties of poly(propylene) fibre-matrix composites. Macromolecular Materials and Engineering, **288**, 599–606 (2003).
DOI: 10.1002/mame.200300023

[6] Houshyar S., Shanks R. A.: Mechanical and thermal properties of flexible poly(propylene) composites. Macromolecular Materials and Engineering, **291**, 59–67 (2006).
DOI: 10.1002/mame.200500306

[7] Bárány T., Izer A., Czigány T.: On consolidation of self-reinforced polypropylene composites. Plastics Rubber and Composites, **35**, 375–379 (2006).
DOI: 10.1179/174328906X128234

[8] Bárány T., Izer A., Karger-Kocsis J.: Impact resistance of all-polypropylene composites composed of alpha and beta modifications. Polymer Testing, **28**, 176–182 (2009).
DOI: 10.1016/j.polymertesting.2008.11.011

[9] Houshyar S., Shanks R. A.: Tensile properties and creep response of polypropylene fibre composites with variation of fibre diameter. Polymer International, **53**, 1752–1759 (2004).
DOI: 10.1002/pi.1569

[10] Houshyar S., Shanks R. A.: Mechanical and thermal properties of toughened polypropylene composites. Journal of Applied Polymer Science, **105**, 390–397 (2007).
DOI: 10.1002/app.25034

[11] Houshyar S., Shanks R. A., Hodzic A.: Tensile creep behaviour of polypropylene fibre reinforced polypropylene composites. Polymer Testing, **24**, 257–264 (2005).
DOI: 10.1016/j.polymertesting.2004.07.003

[12] Greco A., Musardo C., Maffezzoli A.: Flexural creep behaviour of PP matrix woven composite. Composites Science and Technology, **67**, 1148–1158 (2007).
DOI: 10.1016/j.compscitech.2006.05.015

[13] Acha B. A., Reboredo M. M., Marcovich N. E.: Creep and dynamic mechanical behavior of PP-jute composites: Effect of the interfacial adhesion. Composites Part A: Applied Science and Manufacturing, **38**, 1507–1516 (2007).
DOI: 10.1016/j.compositesa.2007.01.003

[14] Kim K. J., Yu W-R., Harrison P.: Optimum consolidation of self-reinforced polypropylene composite and its time-dependent deformation behavior. Composites Part A: Applied Science and Manufacturing, **39**, 1597–1605 (2008).
DOI: 10.1016/j.compositesa.2008.06.005

[15] Chartoff R. P.: Thermoanalytical instrumentation, techniques and methodology. in 'Thermoplastic polymers' (ed.: Turi E. A.) Academic Press, San Diego, 483–743 (1997).

[16] Ferry J. D.: Viscoelastic properties of polymers. Wiley, New York (1980).

[17] Banik K., Abraham T. N., Karger-Kocsis J.: Flexural creep behavior of unidirectional and cross-ply all-poly(propylene) (PURE®) composites. Macromolecular Materials and Engineering, **292**, 1280–1288 (2007).
DOI: 10.1002/mame.200700180

[18] Banik K., Karger-Kocsis J., Abraham T.: Flexural creep of all-polypropylene composites: Model analysis. Polymer Engineering and Science, **48**, 941–948 (2008).
DOI: 10.1002/pen.21041

[19] Chevali V. S., Dean D. R., Janowski G. M.: Flexural creep behavior of discontinuous thermoplastic composites: Non-linear viscoelastic modeling and time-temperature-stress superposition. Composites Part A: Applied Science and Manufacturing, **40**, 870–877 (2009).
DOI: 10.1016/j.compositesa.2009.04.012

[20] Dutta N. K., Edward G. H.: Generic relaxation spectra of solid polymers. 1. Development of spectral distribution model and its application to stress relaxation of polypropylene. Journal of Applied Polymer Science, **66**, 1101–1115 (1997).
DOI: 10.1002/(SICI)1097-4628(19971107)66:6<1101::AID-APP11>3.0.CO;2-4

[21] Izer A., Bárány T., Varga J.: Development of woven fabric reinforced all-polypropylene composites with beta nucleated homo- and copolymer matrices. Composites Science and Technology, **69**, 2185–2192 (2009).
DOI: 10.1016/j.compscitech.2009.06.002

[22] Attalla G., Guanella I. B., Cohen R. E.: Effect of morphology on stress-relaxation of polypropylene. Polymer Engineering and Science, **23**, 883–887 (1983).
DOI: 10.1002/pen.760231605

[23] Alcock B., Cabrera N. O., Barkoula N-M., Reynolds C. T., Govaert L. E., Peijs T.: The effect of temperature and strain rate on the mechanical properties of highly oriented polypropylene tapes and all-polypropylene composites. Composites Science and Technology, **67**, 2061–2070 (2007).
DOI: 10.1016/j.compscitech.2006.11.012

eXPRESS Polymer Letters Vol.4, No.4 (2010) 217–226
Available online at www.expresspolymlett.com
DOI: 10.3144/expresspolymlett.2010.28

Effect of silane treatment of carboxylic-functionalized multi-walled carbon nanotubes on the thermal properties of epoxy nanocomposites

T. Zhou[1,2*], *X. Wang*[1], *X. H. Liu*[1], *J. Z. Lai*[2]

[1]Key Laboratory for Soft Chemistry & Functional Materials of Ministry Education, Nanjing University of Science and Technology, Nanjing 210094, China
[2]Department of Materials Science & Engineering, Nanjing University of Science and Technology, Nanjing 210094, China

Received 22 December 2009; accepted in revised form 6 February 2010

Abstract. The effect of silane treatment of carboxylic-functionalized multi-walled carbon nanotubes (COOH-MWCNTs) on the thermal properties of COOH-MWCNTs/epoxy nanocomposites was studied by comparing the research results on differential scanning calorimetry and thermogravimetric analysis data of silane treated COOH-MWCNTs/epoxy system with those of as-received COOH-MWCNTs/epoxy system. At the initial curing stage, silane treatment of COOH-MWCNTs does not change the autocatalytic cure reaction mechanism of COOH-MWCNTs/diglycidyl ether of bisphenol-A glycidol ether epoxy resin/2-ethyl-4-methylimidazole (COOH-MWCNTs/DGEBA/EMI-2,4) system, however, silane treatment of COOH-MWCNTs has catalytic effect on the curing process, which could help to shorten pre-cure time or lower pre-temperature. Then, at the later curing stage, silane treatment of COOH-MWCNTs promotes vitrification, which would help to shorten post-cure time or lower post-temperature. Therefore, overall, silane treatment of COOH-MWCNTs could bring positive effect on the processing of epoxy nanocomposites. Furthermore, it was also found that silane treatment of COOH-MWCNTs does not affect the thermal degradation pattern of COOH-MWCNTs/DGEBA/EMI-2,4 system, however, decreases the thermal stability of COOH-MWCNTs/DGEBA/EMI-2,4 nanocomposites.

Keywords: *polymer composites, thermal properties, differential scanning calorimetry (DSC), thermogravimetric analysis (TGA)*

1. Introduction

The property enhancements of epoxy nanocomposites filled with carbon nanotubes (CNTs) are far below the expectations based on the excellent properties of CNTs. However, studies suggested that the properties can be further improved if better dispersion and more efficient interfacial adhesion can be achieved. One of the most promising approaches is to chemically modify the surface of CNTs before dispersing CNTs into epoxy [1–7]. Since silane coupling agent can act as a chemical bridge between hydrophilic CNTs and hydrophobic epoxy, silane treatment of CNTs will be efficient to enhance CNTs/epoxy interfacial adhesion, as well as preventing the agglomeration of CNTs. Furthermore, functionalized CNTs are more desirable than non-functionalized CNTs since functionalized CNTs have more functional groups to form chemical bonding with coupling agent and/or epoxy. Therefore, in this study, we filled epoxy with γ-aminopropyl-triethoxysilane (A1100) treated carboxylic-functionalized multi-walled CNTs (COOH-MWCNTs).

Different chemical modification of CNTs would result in differences in the way the epoxy and/or the curing agent reacts with CNTs, which in turn, affect

*Corresponding author, e-mail: ztltianle999@hotmail.com

the cure reaction which determines the resulting properties. Recently some studies have been stimulated to address the effect of functionalized CNTs on the cure reaction of epoxy systems [7–12], however, few efforts have been made to address the effect of silane treatment of functionalized CNTs on the cure reaction of functionalized CNTs/epoxy systems. Furthermore, chemical modification of CNTs may also affect the thermal stability of epoxy nanocomposites [9], but hardly any published papers are available to date on the effect of silane treatment of COOH-MWCNTs on the thermal stability of COOH-MWCNTs/DGEBA/EMI-2,4 nanocomposites.

In this work, by comparing the research results on differential scanning calorimetry (DSC) and thermogravimetric analysis (TGA) data of silane treated COOH-MWCNTs/epoxy system with those of as-received COOH-MWCNTs/epoxy system, the effect of silane treatment of COOH-MWCNTs on the thermal properties of COOH-MWCNTs/epoxy nanocomposites was studied. We do theoretical work, analyzing dynamic DSC data with an isoconversional kinetics method, to obtain the effect of silane treatment of COOH-MWCNTs on the curing kinetics of COOH-MWCNTs/DGEBA/EMI-2,4 nanocomposites. Particular emphasis is given to the study on the variation of activation energy E during the curing process, which is conducive to better understanding of the effect of silane treatment of COOH-MWCNTs on the cure behavior of nanocomposites, and thus will be valuable to provide guidance for choosing proper processing methods. This work is part of a wider investigation on high performance nanocomposites for more demanding applications, such as in nanoelectronics applications.

2. Experimental

2.1. Materials

Epoxy resin used in this work was a nominally difunctional epoxy resin, Epon 828, supplied by Shanghai Resin Co. Ltd., Shanghai, China. Epon 828 is, basically, DGEBA with epoxy value of 0.48–0.52 mol/100 g. Curing agent, EMI-2,4, was offered by Beijing Chemical Reagent Co. Ltd., Beijing, China. COOH-MWCNTs were provided by Chengdu Organic Chemicals Co. Ltd., Chinese Academy of Sciences, Chengdu, China. Details of the as-received COOH-MWCNTs are summarized in Table 1. Before stored in desiccators, COOH-MWCNTs were dried at 110°C for 24 h in vacuum to eliminate the agglomeration caused by hygroscopic absorption, as well as removing surface water, which would hinder the interaction between coupling agent and COOH-MWCNTs. Amino silane coupling agent, A1100, was obtained from Shanghai Chemical Reagent Co. Ltd., Shanghai, China. Other agents utilized were analytically pure grade and supplied by Sinopharm Chemical Reagent Co. Ltd., Shanghai, China.

Table 1. Specification of as-received COOH-MWCNTs (supplied by the manufacturer)

	COOH-MWCNTs
Functionalized rate of surface carbon atom	8–10 mol%
Carboxylic group weight percentum	1–6 wt%
Purity	>95%
Color	black
Outside Diameter	50–80 nm
Inside Diameter	5–15 nm
Length	10–20 μm
Specific Surface Area	>40 m^2/g
Bulk density	0.05 g/cm^3
True density	2.1 g/cm^3
Making method	CVD

2.2. Silane treatment of COOH-MWCNTs

Silane treatment of COOH-MWCNTs using A1100 involved (a) making a silane-absolute ethanol solution at 0.001 g/ml concentration, and the amount of A1100 was 10% by weight of COOH-MWCNTs, (b) adding dried COOH-MWCNTs to the solution, stirring with a magnetic stirrer at 60°C for 30 min, then dispersing the solution by sonication for 1 h, (c) rinsing with absolute ethanol by filtration, then washing silane treated particles with absolute ethanol repeatedly, and (d) drying at 110°C for 1 h in vacuum. Before stored in desiccators, the dried silane treated COOH-MWCNTs were weighted and the amount of silane coupling agent introduced onto the surface of COOH-MWCNTs was about 7.3% by weight of COOH-MWCNTs.

In this study, silane treated COOH-MWCNTs, compared with as-received COOH-MWCNTs, go through an additional treatment of 30 min stir and 1 h sonication during the silane treatment process as introduced in the previous passage. This additional treatment may lead to some defects in the

nanotubes and a decrease of the aspect ratios of COOH-MWCNTs; therefore, besides the effect of functional groups of silane coupling agent, this additional treatment may also contributes to the final effect of silane treatment of COOH-MWCNTs on the thermal properties of epoxy nanocomposites.

Fourier-transform infrared (FTIR) spectra of as-received COOH-MWCNTs and silane treated COOH-MWCNTs are shown in Figure 1. It is obvious that there is a mass of OH, C=O groups on the surface of COOH-MWCNTs, while a lot of C–O–Si bonds are found to exist on the surface of silane treated COOH-MWCNTs, confirming that silane coupling agent has been covalently bonded to COOH-MWCNTs as excepted. Characteristic vibrational bands of the functional groups are shown in the spectra. The intensity of the characteristic peak of OH group decreases with increasing extent of COOH-MWCNTs modification. According to Beer-Lambert Law, the characteristic peak of C=O group can be regarded as the internal standard, and then the extent of COOH-MWCNTs modification can be quantitatively calculated by Equation (1):

$$\eta = 1 - \frac{B'_{OH} / B'_{C=O}}{B_{OH} / B_{C=O}} \quad (1)$$

where B is the absorbance of as-received COOH-MWCNTs, B' is the absorbance of silane treated COOH-MWCNTs, and the OH and C=O subscripts represent OH and C=O groups, respectively. In this study, the extent of COOH-MWCNTs modification is calculated to be ~56%. Furthermore, the FTIR result (–CH stretching) shows that COOH-MWCNTs contain defects. These defects may be formed during the COOH-MWCNTs manufacturing, and the silane treatment of COOH-MWCNTs has no obvious effect on the –CH peak, as shown in Figure 1.

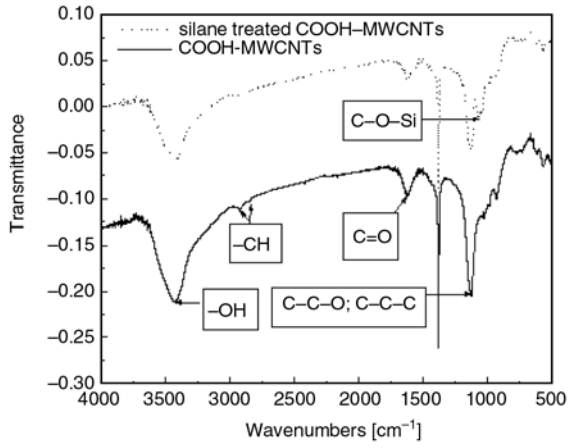

Figure 1. FTIR spectra of as-received COOH-MWCNTs and silane treated COOH-MWCNTs

2.3. Composites preparation

The COOH-MWCNTs/DGEBA/EMI-2,4 nanocomposites were prepared by solution blending and casting method, which involved (a) stirring

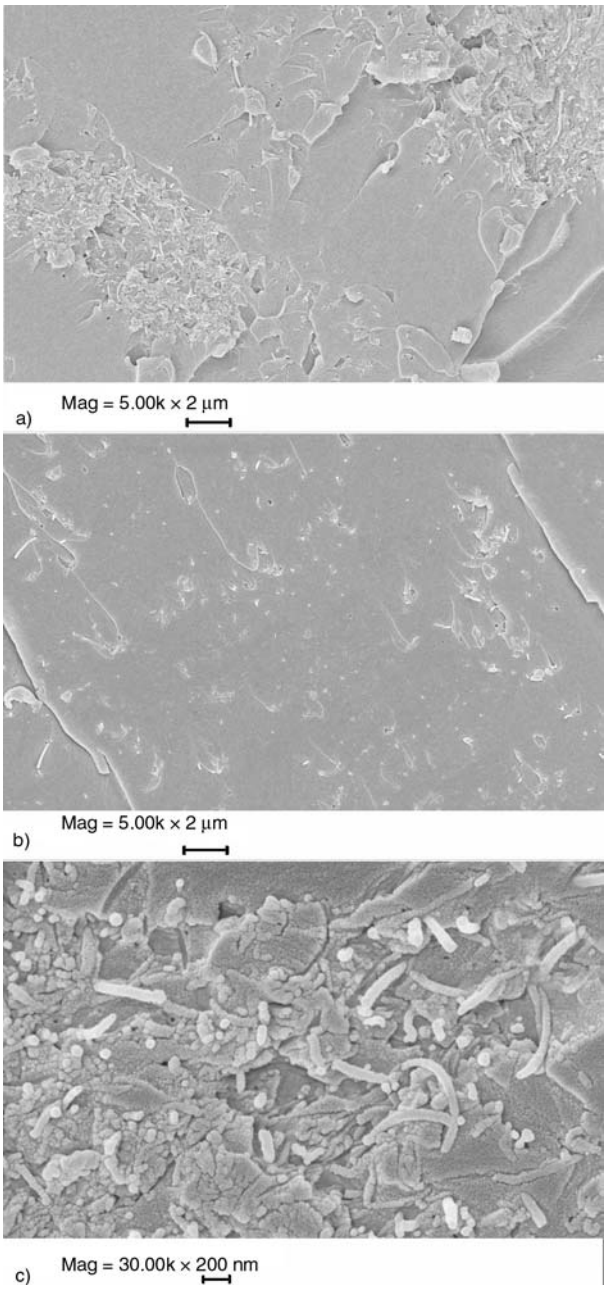

Figure 2. Micrographs of as-received 3%COOH-MWCNTs/DGEBA/EMI-2,4 nanocomposite (a) 5k× and silane treated 3%COOH-MWCNTs/DGEBA/EMI-2,4 nanocomposite (b) 5k× and (c) 30k×

DGEBA-absolute ethanol solution at 80°C with magnetic stirrer for 20 min, (b) adding appropriate amount of silane treated or untreated COOH-MWCNTs to the solution and continuing stir for 30 min, then sonicating the solution for 1 h to ensure good homogeneity, (c) cooling to 60°C, (d) adding EMI-2,4, which is 6% by weight of DGEBA, to the mixture and continuing stir for 10 min, (e) casting the mixture in mould, (f) repeatedly degassing the mixture in vacuum drying oven at 60°C until no air bubble appears on the surface of the mixture, (g) curing the mixture at 65°C for 1 h, 120°C for 1.5 h, and 160°C for 1.5 h, (h) cooling to room temperature, then demoulding.

Figure 2 shows the FE-SEM micrographs of 3%COOH-MWCNTs/DGEBA/EMI-2,4 nanocomposites. As shown in Figure 2a, as-received COOH-MWCNTs agglomerate severely, however, silane treated COOH-MWCNTs in Figure 2b are seen to be better dispersed and their distribution in matrix is relatively homogeneous, therefore silane treatment is indeed effective in improving the dispersion of COOH-MWCNTs in the epoxy matrix. Since silane treated COOH-MWCNTs' agglomeration still exists, as shown in Figure 2c, the dispersion of COOH-MWCNTs in the matrix still needs to be improved by some means in future work. Besides, naked nanotubes are observed on the fracture surface and some nanotubes are pulled out of the surface instead of being embedded and tightly held to the matrix, indicating interfacial bonding between the COOH-MWCNTs and epoxy also needs to be improved by some means in future work.

2.4. Characterization

FTIR spectra were recorded in KBr pellets on a VECTOR22 spectrometer (Bruker Co., Germany). Blank scanning was performed before measurements to eliminate the influence of water vapor and CO_2 in air.

The specimens with the compositions listed in Table 2 were prepared at ambient temperature. The base polymer formulation was prepared by mixing DGEBA and EMI-2,4 with a weight ratio of 100:6 for 15 min. A specified quantity of COOH-MWCNTs was added into the base polymer and the mixture was dispersed by sonication for 1.5 h. A sample of approximately 4 mg was weighted accurately into an aluminum DSC sample pan, and then covered with an aluminum lid.

Dynamic DSC measurements with a DSC-Q20 (TA Instruments, USA) system which was calibrated with an indium standard were performed at different heating rates of 10, 15 and 20°C/min over a temperature range of 30–300°C. The reaction was considered to be complete when the rate curve leveled off to a baseline. The exotherm was measured under a nitrogen flow rate of 10 ml/min. The exotherm baseline was corrected via data in the empty chamber. The cured sample was left in the DSC cell and cooled to 30°C, and then the cured sample was scanned at 20°C/min to determine the glass transition temperature (T_g) of the reacted product. The initial temperature of the heat flow step of the second diagram was taken to be the T_g. The total area under the exotherm curve, based on the extrapolated baseline at the end of the reaction, was used to calculate the heat of reaction, ΔH [J/g].

Morphological studies of the fracture surfaces of the nanocomposites were carried out using FE-SEM (LEO1550, LEO Electron Microscopy Ltd., Cambridge, UK). The nanocomposites were fractured in liquid nitrogen and then the fracture surfaces were coated with a thin gold layer before FE-SEM.

Thermal degradation studies were performed using TGA (STA-449C system, NETZSCH Instruments Co., Germany) at a scan rate of 10°C/min to 750°C in N_2 atmosphere. Five specimens from each system (neat epoxy, C3 and S3) were tested and the average was reported.

Table 2. Compositions of tested specimens (by weight)

System	DGEBA/EMI-2,4	COOH-MWCNTs	Silane treated COOH-MWCNTs
Neat epoxy	100/6	0	0
C1	100/6	1	0
C3	100/6	3	0
C5	100/6	5	0
S1	100/6	0	1
S3	100/6	0	3
S5	100/6	0	5

3. Results and discussion

It is known that activation energy E represents the potential barrier of cure reaction. The study on the variation of E during the curing process is conducive to better understanding on the effect of silane treatment of COOH-MWCNTs on the cure behavior of COOH-MWCNTs/epoxy nanocomposites. In this work, we use Friedman kinetics method, a differential isoconversional kinetics method which assumes that E is a function of fractional extent of conversion α, i.e., curing degree, to analyze dynamic DSC data for obtaining the variation of E during the curing process.

The curing mechanism of DGEBA/EMI-2,4 system involves two stages consisting of adduct and etherification reactions. The O^-/OH adducts are believed to be the catalyst that initiates the etherification reactions which cross-link the epoxy and determine the final properties. Previous work showed that the adduct formation is necessary prior to the etherification reactions [13–15]. Thus, low EMI-2,4 concentrations can be used to analyze the etherification reactions by suppressing the adduct formation. The objective criterion of meeting this specification is that the heat of reaction, ΔH, approaches a constant. It is shown that the variation amplitude of ΔH is small when the concentration of EMI-2,4 is between 3 and 10% by weight of DGEBA, as the cure reaction is incomplete when the content of EMI-2,4 is below 3 wt% [16]. In this work, the concentration of EMI-2,4 is 6 wt% which falls within the range of 3–10 wt%, therefore the heat of reaction for the etherification reaction peak is approximately the total heat of cure reaction. Furthermore, relative to the magnitude of ΔH, the heat released during the chemical reaction between amino silane coupling agent and epoxy is small, e.g., ΔH of S3 and C3 system are 355.7 and 345.6 J/g, respectively (as listed in Table 3). Thus, in this work, the etherification reactions dominate the curing process and ΔH can be considered as a constant over the whole cure reaction. Then, the rate of the cure reaction is $d\alpha/dt = (dH/dt)/\Delta H$ where dH/dt is the heat flow above the baseline.

Table 3. Total heats of reaction (ΔH) and exothermic peak temperatures (T_p) at 10°C/min heating rate, inflexions of the curves of E_α, and glass transition temperatures (T_g) of the cured systems

System	ΔH [J/g]	T_p [°C]	Inflexions of the curves of E_α	T_g [°C]
Neat epoxy	361.8	126.56	0.50	154
C1	357.2	113.74	0.50	144
C3	345.6	107.41	0.65	137
C5	343.9	104.82	0.70	131
S1	363.6	112.49	0.45	146
S3	355.7	104.64	0.60	141
S5	351.3	101.54	0.60	137

Friedman kinetics method starts with the basic equation that relates $d\alpha/dt$ to some function of the concentration of reactants. For the thermosetting resins, $d\alpha/dt$ is usually expressed by Equation (2):

$$\frac{d\alpha}{dt} = Ae^{-E/RT} f(\alpha) \tag{2}$$

where A is the frequency factor, E is the activation energy, $f(\alpha)$ is a function of the fractional extent of conversion α and is associated with a certain reaction mechanism, R is the gas constant and T is the absolute temperature at time t.

From Equation (2) Equation (3) is obtained:

$$\ln\left(\frac{d\alpha}{dt}\right) = \ln A - \frac{E}{RT} + \ln f(\alpha) \tag{3}$$

Let $Af(\alpha) = F(\alpha)$, then from Equation (3) Equation (4) follows:

$$\ln\left(\frac{d\alpha}{dt}\right) = -\frac{E}{RT} + \ln F(\alpha) \tag{4}$$

From Equation (4), a plot of $\ln(d\alpha/dt)$ vs. $1/T$ at the same α from a series of dynamic DSC experiments at different heating rates would result in a straight line with a slope of $-E/R$. Repeating this procedure, E_α values corresponding to different α from the dynamic DSC curing curves can be obtained. Thus the relationship of E_α vs. α can be decided [17].

Figures 3–5 are the plots of $\ln(d\alpha/dt)$ vs. $1/T$ of neat epoxy, Ci and Si (i = 1, 3, 5) systems for various

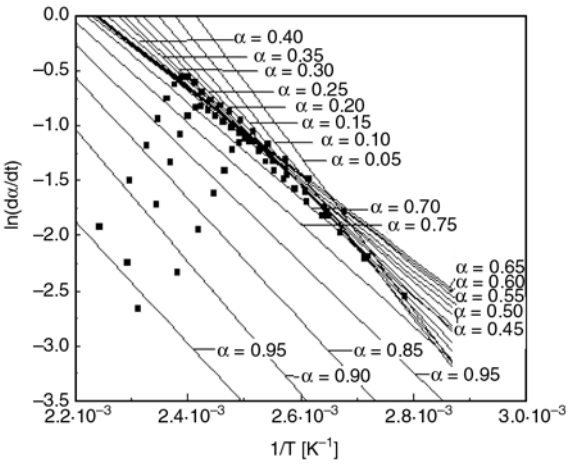

Figure 3. Plots of $\ln(d\alpha/dt)$ vs. $1/T$ of neat epoxy system

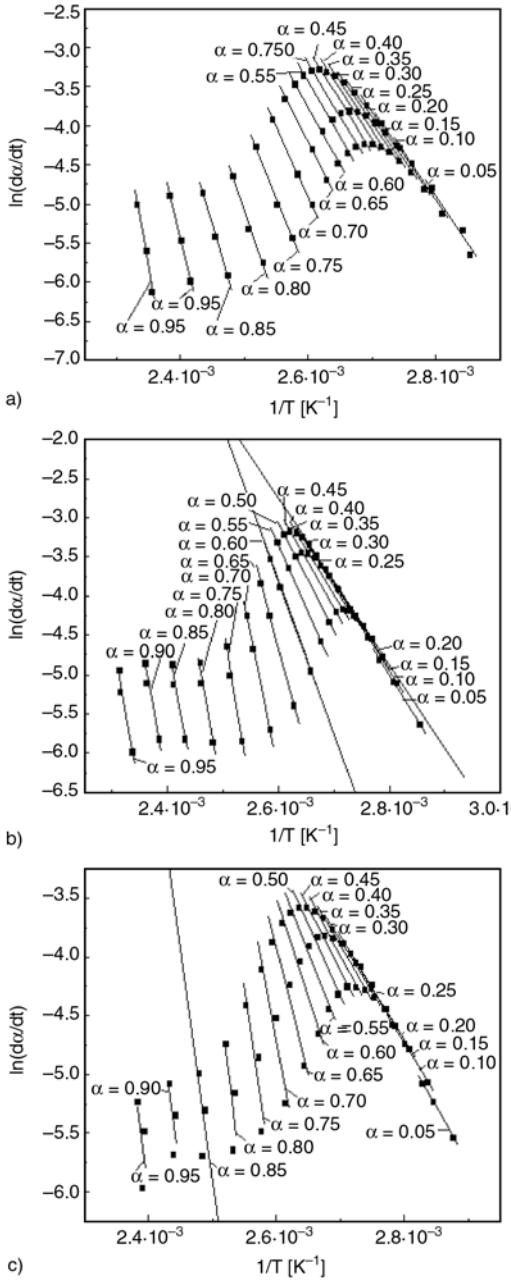

Figure 4. Plots of ln(dα/d*t*) vs. 1/*T* of (a) C1, (b) C3 and (c) C5 systems

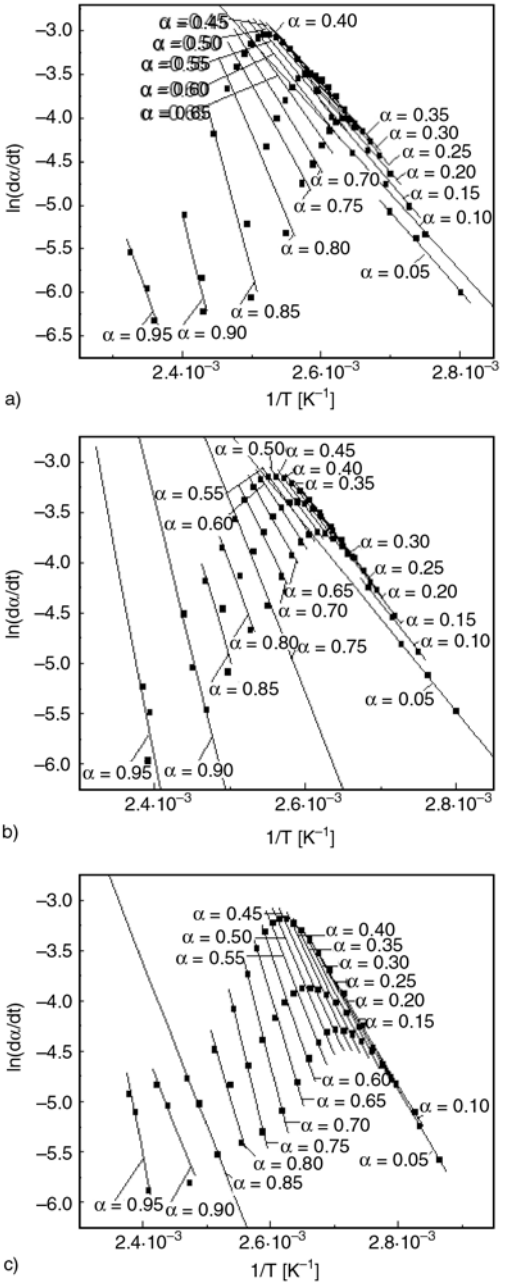

Figure 5. Plots of ln(dα/d*t*) vs. 1/*T* of (a) S1, (b) S3 and (c) S5 systems

values of α (α = 0.05, 0.10, 0.15, …, 0.90, 0.95) covering the experimental range, respectively. Fitting linear regression lines, the groups of E_α values of each system were obtained. Figure 6 shows the plots of E_α vs. α of neat epoxy, Ci and Si (*i* = 1, 3, 5) systems. It can be seen that, for all the studied systems, *E* initially decreases at low conversions, and then increases as the curing process proceeds.

The cure reaction of DGEBA/EMI-2,4 system is autocatalytic. The O^-/OH adducts are not consumed since they are continually regenerated during the following etherification reactions, it is therefore reasonable to expect a decrease in *E*, as compared to the very beginning of the curing process where no autocatalyzed reaction occurs. As is shown in Figure 6, at the initial curing stage, values of *E* of all the studied systems decrease with increasing α, demonstrating that the introduction of COOH-MWCNTs does not change the autocatalytic cure reaction mechanism of DGEBA/EMI-2,4 system and silane treatment of COOH-MWCNTs also does not change the autocatalytic cure reaction mechanism of COOH-MWCNTs/DGEBA/EMI-2,4 system. Additionally, it can be seen that

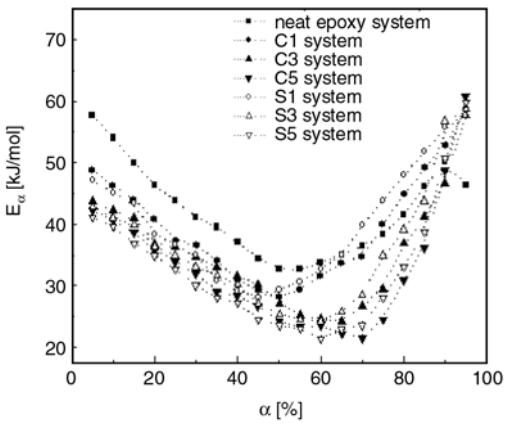

Figure 6. Plots of E_α vs. α of neat epoxy, C1, C3, C5, S1, S3 and S5 systems. Dotted lines are given only for showing the tendency.

increasing COOH-MWCNTs content and silane treatment of COOH-MWCNTs decrease *E*, so both COOH-MWCNTs and silane treatment of COOH-MWCNTs have catalytic effect on the initial curing process, which can also be evidenced by decreased exothermic peak temperature T_p, as shown in Table 3. Moreover, the decrease effect on *E* and T_p is already noticeable at the lowest content of COOH-MWCNTs investigated (1 wt%) with slightly further effect at higher concentrations, proving a saturation of catalyzing action at higher contents investigated (3 and 5 wt%), possibly due to the physical hindrance of COOH-MWCNTs to the mobility of epoxy monomers [18].

The catalytic effect of non-functionalized CNTs at the initial curing stage was also found in previous works [19–23] and the accelerating effect observed was primarily ascribed to the extremely high thermal conductivity of CNTs [22, 23]. In this study, besides the high thermal conductivity of CNTs, the catalytic effect of COOH-MWCNTs can also be attributed to the carboxyl groups (–COOH) which would function as O^-/OH adducts, exert a catalytic effect for epoxide ring opening, and react with the epoxide hydroxyl group creating the ether link, i.e., C–O–C bonds. Furthermore, the catalytic effect of silane treatment of COOH-MWCNTs can be attributed to the amino group ($–NH_2$) end of the coupling agent which would function as EMI-2,4 and accelerate the cure reaction.

As the curing process proceeds, the system undergoes gelation (liquid-to-rubber) and vitrification (rubber-to-glass) transitions. As the glass transition temperature (T_g) increases over the curing temperature (T_c), the system vitrifies. At the glassy state, the small amount of free volume only allows local motions of the chain segments. To initiate translational motion of the segments, it requires a great degree of cooperativity between the chain segments, which is associated with a large energy barrier as reflected in the great value of *E*, so when the system vitrifies, the value of *E* begins to increase. It can be seen in Figure 6 and Table 3 that the inflexions of the curves of *E*, i.e., the fractional extents of conversion α where *E* begins to increase, increase with increasing COOH-MWCNTs content, so COOH-MWCNTs prevent from vitrification at the later curing stage, however, there is a slight reduction of inflections for the Si (*i* = 1, 3, 5) systems in comparison with the Ci (*i* = 1, 3, 5) systems, so silane treatment of COOH-MWCNTs decreases the inflexions, implying that silane treatment of COOH-MWCNTs promotes vitrification.

The phenomena can be interpreted by Table 3 that T_gs of COOH-MWCNTs/epoxy systems decrease with increasing COOH-MWCNTs content, thus make it difficult for T_g to increase over T_c, consequently prevents from vitrification, on the other hand, there is a slight increase of T_gs for the Si (*i* = 1, 3, 5) systems in comparison with the Ci (*i* = 1, 3, 5) systems, so silane treatment of COOH-MWCNTs increases the T_gs of COOH-MWCNTs/epoxy systems, thus promotes vitrification.

Usually T_g decreases with decreasing crosslinking density and increased chain mobility [22]. The high COOH-MWCNTs/epoxy interface creates extra free volume and therefore extra chain mobility and lower T_g compared with neat epoxy. At higher loadings, the difficulty to disperse COOH-MWCNTs remarkably increases and agglomeration can occur. Agglomeration decreases the surface-to-volume ratio of the nanoparticles and therefore increases T_g, however, the final effect is that T_g of the COOH-MWCNTs/epoxy systems decreases with increasing loading, as shown in Table 3.

Silane treatment of COOH-MWCNTs improves the compatibility between COOH-MWCNTs and epoxy matrix, and thus results in a more 'compact' structure and increased T_gs, thereby resulting in promoted vitrification.

For the development of nanocomposites, the cure acceleration effect caused by COOH-MWCNTs and silane treatment of COOH-MWCNTs could bring positive effect on the processing of nanocom-

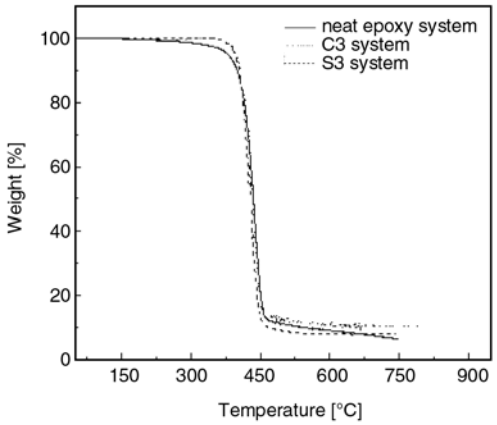

Figure 7. TGA curves of neat epoxy, C3 and S3 systems

posites since it needs shorter pre-cure time or lower pre-temperature, the hindrance effect to vitrification of COOH-MWCNTs would bring negative effect as it needs longer post-cure time or higher post-temperature, however, silane treatment of COOH-MWCNTs promotes vitrification, which would help to shorten post-cure time or lower post-temperature.

Since silane treatment of COOH-MWCNTs could bring positive effect on the processing of nanocomposites, silane treatment of COOH-MWCNTs on the thermal stability of the nanocomposites was also evaluated. TGA curves of neat epoxy, C3 and S3 systems are shown in Figure 7. The curves in Figure 7 are similar, indicating that the introduction of COOH-MWCNTs does not affect the thermal degradation pattern of DGEBA/EMI-2,4 system and silane treatment of COOH-MWCNTs does not affect the thermal degradation pattern of COOH-MWCNTs/DGEBA/EMI-2,4 system.

All the TGA curves have only one step degradation and it is a common practice to consider the peak degradation temperature as the thermal stability for such cases [24]. In this study, the thermal degradation onset temperature T_{onset}, determined from the intersection of two tangents at the first inflection point, and the char residual at 750°C were summarized in Table 4. The difference in T_{onset} of C3 and S3 is not noticeable, however, the difference in T_{onset} of neat epoxy and C3 is really noticeable and the addition of COOH-MWCNTs increases T_{onset}, so the addition of COOH-MWCNTs would delay the thermal degradation of DGEBA/EMI-2,4 system. In addition, the half-weight-loss temperature T_{half} was also summarized in Table 4. It is a common practice to consider T_{half} as an indicator for the beginning of structural decomposition [24]. The difference in T_{half} of neat epoxy and C3 is not really noticeable, however, the difference in T_{half} of C3 and S3 is noticeable and silane treatment of COOH-MWCNTs decreases T_{half}, so silane treatment of COOH-MWCNTs decreases the thermal stability of COOH-MWCNTs/DGEBA/EMI-2,4 nanocomposites.

Table 4. Thermal stabilities of neat epoxy, C3 and S3 systems as determined from TGA curves

System	T_{onset} [°C]	T_{half} [°C]	Char residual at 750°C [%]
Neat epoxy	404.9±0.2	433.4±0.1	6.03±0.12
C3	410.8±0.3	434.9±0.2	10.23±0.13
S3	410.2±0.2	430.1±0.2	7.58±0.15

When COOH-MWCNTs are introduced into system, there would, on the one hand, result in a decrease in thermal stability, which can be due to the weakened Van der Waals interaction between polymer chains [25] and the lowered T_g shown in Table 3. On the other hand, the addition of COOH-MWCNTs can also increase the thermal stability due to their hindering effect to the thermal motion of polymer molecular chains [26]. However, the final result of COOH-MWCNTs on the thermal stability, arising from the antagonistic competition of these two effects, is that the addition of COOH-MWCNTs slightly improves the thermal stability of DGEBA/EMI-2,4 system.

Silane treatment of COOH-MWCNTs enhances the interactions between COOH-MWCNTs and epoxy, weakening Van der Waals interaction between polymer chains, resulting in decreased thermal stability, but its effect of enhanced T_g would lead to increased thermal stability, however, the final result is that silane treatment of COOH-MWCNTs decreases the thermal stability of COOH-MWCNTs/DGEBA/EMI-2,4 nanocomposites.

4. Conclusions

By comparing the research results on DSC and TGA data of silane treated COOH-MWCNTs/epoxy system with those of as-received COOH-MWCNTs/epoxy system, the effect of silane treatment of COOH-MWCNTs on the thermal properties of COOH-MWCNTs/epoxy system was obtained.

At the initial curing stage, the introduction of COOH-MWCNTs does not change the autocatalytic cure reaction mechanism of DGEBA/EMI-2,4 system and silane treatment of COOH-MWCNTs does not change the autocatalytic cure reaction mechanism of COOH-MWCNTs/DGEBA/EMI-2,4 system. Both COOH-MWCNTs and silane treatment of COOH-MWCNTs have catalytic effect on the curing process. Then, at the later curing stage, COOH-MWCNTs prevent from vitrification; however, silane treatment of COOH-MWCNTs promotes vitrification.

The cure acceleration effect caused by COOH-MWCNTs and silane treatment of COOH-MWCNTs could bring positive effect on the processing of epoxy nanocomposites since it needs shorter pre-cure time or lower pre-temperature, the hindrance effect to vitrification of COOH-MWCNTs would bring negative effect as it needs longer post-cure time or higher post-temperature, however, silane treatment of COOH-MWCNTs promotes vitrification, which would help to shorten post-cure time or lower post-temperature.

The introduction of COOH-MWCNTs does not affect the thermal degradation pattern of DGEBA/EMI-2,4 system and silane treatment of COOH-MWCNTs does not affect the thermal degradation pattern of COOH-MWCNTs/DGEBA/EMI-2,4 system. The addition of COOH-MWCNTs would delay the thermal degradation of DGEBA/EMI-2,4 system and silane treatment of COOH-MWCNTs decreases the thermal stability of COOH-MWCNTs/DGEBA/EMI-2,4 nanocomposites.

Acknowledgements

The authors are grateful for the financial support of National Natural Science Foundation of China (No.10776014, No.50808101), China Postdoctoral Science Foundation funded project (No.20080431103), High Technical Foundation of Jiangsu Province of China (No.BG2007047), Natural Science Foundation of Jiangsu Province of China (No.BK2008407, No.BK2008417), Jiangsu Planned Projects for Postdoctoral Research Funds (No.0801023B), Special Foundation for Young Scholars of Nanjing University of Science & Technology (No.AB41339).

References

[1] Abdalla M., Dean D., Adibempe D., Nyairo E., Robinson P., Thompson G.: The effect of interfacial chemistry on molecular mobility and morphology of multiwalled carbon nanotubes epoxy nanocomposite. Polymer, **48**, 5662–5670 (2007).
DOI: 10.1016/j.polymer.2007.06.073

[2] Xie X-L., Mai Y-W., Zhou X-P.: Dispersion and alignment of carbon nanotubes in polymer matrix: A review. Materials Science and Engineering R: Reports, **49**, 89–112 (2005).
DOI: 10.1016/j.mser.2005.04.002

[3] Zhu J., Kim J., Peng H., Margrave J. L., Khabashesku V. N., Barrera E. V.: Improving the dispersion and integration of single-walled carbon nanotubes in epoxy composites through functionalization. Nano Letters, **3**, 1107–1113 (2003).
DOI: 10.1021/nl0342489

[4] Zhu J., Peng H., Fernando R-M., Margrave J. L., Khabashesku V. N., Imam A. M., Lozano K., Barrera E. V.: Reinforcing epoxy polymer composites through covalent integration of functionalized nanotubes. Advanced Functional Materials, **14**, 643–648 (2004).
DOI: 10.1002/adfm.200305162

[5] Theodore M., Hosur M., Thomas J., Jeelani S.: Effect of functionalization on the properties of multi-waited carbon nanotubes. in 'International SAMPE Symposium and Exhibition, Baltimore, USA, vol 52, 15–18 (2007).

[6] Shen J., Huang W., Wu L., Hu Y., Ye M.: Thermophysical properties of epoxy nanocomposites reinforced with amino-functionalized multi-walled carbon nanotubes. Composites Part A: Applied Science and Manufacturing, **38**, 1331–1336 (2007).
DOI: 10.1016/j.compositesa.2006.10.012

[7] Abdalla M., Dean D., Robinson P., Nyairo E.: Cure behavior of epoxy/MWCNT nanocomposites: The effect of nanotube surface modification. Polymer, **49**, 3310–3317 (2008).
DOI: 10.1016/j.polymer.2008.05.016

[8] Yang K., Gu M., Jin Y., Mu G., Pan X.: Influence of surface treated multi-walled carbon nanotubes on cure behavior of epoxy nanocomposites. Composites Part A: Applied Science and Manufacturing, **39**, 1670–1678 (2008).
DOI: 10.1016/j.compositesa.2008.07.011

[9] Yang K., Gu M., Jin Y.: Cure behavior and thermal stability analysis of multiwalled carbon nanotube/epoxy resin nanocomposites. Journal of Applied Polymer Science, **110**, 2980–2988 (2008).
DOI: 10.1002/app.28898

[10] Terenzi A., Vedova C., Lelli G., Mijovic J., Torre L., Valentini L., Kenny J. M.: Chemorheological behaviour of double-walled carbon nanotube-epoxy nanocomposites. Composites Science and Technology, **68**, 1862–1868 (2008).
DOI: 10.1016/j.compscitech.2008.01.005

[11] Zhou T., Wang X., Wang T.: Cure reaction of multi-walled carbon nanotubes/diglycidyl ether of bisphenol A/2-ethyl-4-methylimidazole (MWCNTs/DGEBA/EMI-2,4) nanocomposites: Effect of carboxylic functionalization of MWCNTs. Polymer International, **58**, 445–452 (2009).
DOI: 10.1002/pi.2558

[12] Zhou T., Wang X., Zhu H., Wang T.: Influence of carboxylic functionalization of MWCNTs on the thermal properties of MWCNTs/DGEBA/EMI-2,4 nanocomposites. Composites Part A: Applied Science and Manufacturing, **40**, 1792–1797 (2009).
DOI: 10.1016/j.compositesa.2009.08.019

[13] Heise M. S., Martin G. C.: Mechanisms of 2-ethyl-4-methylimidazole in the curing of the diglycidyl ether of bisphenol A. Journal of Polymer Science Part C: Polymer Letters, **26**, 153–157 (1988).
DOI: 10.1002/pol.1988.140260305

[14] Heise M. S., Martin G. C.: Curing mechanism and thermal properties of epoxy-imidazole systems. Macromolecules, **22**, 99–104 (1989).
DOI: 10.1021/ma00191a020

[15] Heise M. S., Martin G. C.: Analysis of the cure kinetics of epoxy/imidazole resin systems. Journal of Applied Polymer Science, **39**, 721–738 (1990).
DOI: 10.1002/app.1990.070390321

[16] Zhou T., Gu M., Jin Y., Wang J.: Mechanism and kinetics of epoxy-imidazole cure studied with two kinetic methods. Polymer Journal, **37**, 833–840 (2005).
DOI: 10.1295/polymj.37.833

[17] Xiong Y., Boey F. Y. C., Rath S. K.: Kinetic study of the curing behavior of bismaleimide modified with diallylbisphenol A. Journal of Applied Polymer Science, **90**, 2229–2240 (2003).
DOI: 10.1002/app.12885

[18] Akatsuka M., Takezawa Y., Amagi S.: Influences of inorganic fillers on curing reactions of epoxy resins initiated with a boron trifluoride amine complex. Polymer, **42**, 3003–3007 (2001).
DOI: 10.1016/S0032-3861(00)00669-8

[19] Zhou T., Wang X., Liu X., Xiong D.: Influence of multi-walled carbon nanotubes on the cure behavior of epoxy-imidazole system. Carbon, **47**, 1112–1118 (2009).
DOI: 10.1016/j.carbon.2008.12.039

[20] Tao K., Yang S., Grunlan J. C., Kim Y-S., Dang B., Deng Y., Thomas R. L., Wilson B. L., Wei X.: Effects of carbon nanotube fillers on the curing processes of epoxy resin-based composites. Journal of Applied Polymer Science, **102**, 5248–5254 (2006).
DOI: 10.1002/app.24773

[21] Xie H., Liu B., Yuan Z., Shen J., Cheng R.: Cure kinetics of carbon nanotube/tetrafunctional epoxy nanocomposites by isothermal differential scanning calorimetry. Journal of Polymer Science Part B: Polymer Physics, **42**, 3701–3712 (2004).
DOI: 10.1002/polb.20220

[22] Puglia D., Valentini L., Armentano I., Kenny J. M.: Effects of single-walled carbon nanotube incorporation on the cure reaction of epoxy resin and its detection by Raman spectroscopy. Diamond and Related Materials, **12**, 827–832 (2003).
DOI: 10.1016/S0925-9635(02)00358-8

[23] Puglia D., Valentini L., Kenny J. M.: Analysis of the cure reaction of carbon nanotubes/epoxy resin composites through thermal analysis and Raman spectroscopy. Journal of Applied Polymer Science, **88**, 452–458 (2003).
DOI: 10.1002/app.11745

[24] Reneé M. R., Hassan M., Vijaya K. R., Nathaniel C., Shaik J.: Infusion of SiC nanoparticles into SC-15 epoxy: An investigation of thermal and mechanical response. Macromolecular Materials and Engineering, **290**, 423–429 (2005).
DOI: 10.1002/mame.200400202

[25] Chisholm N., Mahfuz H., Rangari V. K., Ashfaq A., Jeelani S.: Fabrication and mechanical characterization of carbon/SiC-epoxy nanocomposites. Composite Structures, **67**, 115–124 (2005).
DOI: 10.1016/j.compstruct.2004.01.010

[26] Reddy C. S., Das C. K.: Polypropylene-nanosilica-filled composites: Effects of epoxy-resin-grafted nanosilica on the structural, thermal, and dynamic mechanical properties. Journal of Applied Polymer Science, **102**, 2117–2124 (2006).
DOI: 10.1002/app.24131

eXPRESS Polymer Letters Vol.4, No.4 (2010) 227–233
Available online at www.expresspolymlett.com
DOI: 10.3144/expresspolymlett.2010.29

Synergistic flame retardant effects between sepiolite and magnesium hydroxide in ethylene-vinyl acetate (EVA) matrix

N. H. Huang[1,2*], *Z. J. Chen*[1,2], *C. H. Yi*[1,2], *J. Q. Wang*[3]

[1]Key Laboratory of Green Processing and Functional Textiles of New Textile Materials, Ministry of Education, Wuhan University of Science and Engineering, Wuhan, 430073, P.R. China
[2]Department of Polymer Science and Engineering, Wuhan University of Science and Engineering, Wuhan, 430073, P.R. China
[3]National Laboratory of Flame Retardant Materials, Beijing Institute of Technology, Beijing, 100081, P.R. China

Received 11 December 2009; accepted in revised form 9 February 2010

Abstract. Some customers are reluctant to change, because the halogen-free solutions may have higher cost. This is one of the reasons that the synergistic effect is always the subject for researchers to pursue. The synergy between sepiolite and magnesium hydroxide (MH) in halogen-free flame retardant ethylene-vinyl acetate (EVA) copolymer was investigated in the paper through some common facilities, such as limiting oxygen index (LOI), UL-94 test, thermogravimetric analysis (TGA), differential thermal analysis (DTA) and cone calorimeter test (CCT). In the wake of the positive results from the LOI and UL-94 tests, the CCT data indicated not only the reduction of heat release rate (HRR) and mass loss rates (MLR), but also prolonged ignition time (TTI) and depressed smoke release (SR) were observed during combustion. Simultaneously, the tensile strength and Young's modulus of the system were also much better improved with the increase of sepiolite added due to the hydrogen bonds between silanol groups attached to the sepiolite molecules and the ester groups of EVA. The synergistic mechanism has been discussed in the paper in terms of the barrier mechanism in the condensed phase.

Keywords: *polymer composites, synergistic effect, flame retardant EVA copolymer, sepiolite, magnesium hydroxide*

1. Introduction

Ethylene-vinyl acetate (EVA) copolymers with different acetate contents are widely used in many fields, particularly in the wire and cable industry as excellent jacketing materials with the required physical and mechanical properties [1, 2]. Due to their facile flammability and awful smoke emission while burning, their practical application has been strictly limited. To achieve the required flame retardant grade of low smoke and non-toxic character, metal hydroxides, e.g. magnesium hydroxide (MH) or aluminum hydroxide, should be added in a great amount, say, up to 50–60% mass fraction, in general. However, high filler loading leads always without exception to a deterioration of the mechanical performance in the composites. One of the appropriate ways is to bring all the synergistic factors into play, i.e. the full use of synergistic agents (or additives) in the system in order to reduce the amount of flame retardant as much as possible.

In recent years, many researches have published similar results related e.g. to zinc borate [3–5], multiwalled carbon nanotubes [6], Fe-MMT[7], layered double hydroxide [8], rubber [9], organo-modified montmorillonite [10], silicon [11], fumed silica [1], talc [12], expandable graphite [13], zinc

*Corresponding author, e-mail: nhhuang1223@yahoo.com.cn

hydroxystannate [14] and ammonium polyphosphate [15], combined with MH. Nevertheless, very few publications appear in the literature concerning the sepiolite used in combination with MH in EVA matrix.

Sepiolite is a family of fibrous hydrated magnesium silicate with the theoretical half unit-cell formula $Si_{12}O_{30}Mg_8(OH)_4(OH_2)_4 \cdot 8H_2O$ [16], similar to the 2:1 layered structure of montmorillonite, consisting of two tetrahedral silica sheets enclosing a central sheet of octahedral magnesia except that the layers lack continuous octahedral sheets [16–21]. The discontinuity of the silica sheets gives rise to the presence of silanol groups (Si–OH) at the edges of the tunnels, which are the channels opened to the external surface of the sepiolite particles. The presence of silanol groups (Si–OH) can enhance the interfacial interaction between sepiolite and polar polymers.

In this paper, the synergistic effects of sepiolite and MH on the flame retardant and thermal properties of the EVA/MH/sepiolite composites have been accomplished through limiting oxygen index (LOI), UL-94 test, thermal analysis (TG/DTA), cone calorimeter test and the measurement of mechanical properties.

2. Experimentals

2.1. Materials

The EVA copolymer used was a commercial grade Evatane® 28 03 (Arkema), with a vinyl acetate content of 28% mass fraction and a melt flow index of 3.6 g/10 min. Magnesium hydroxide(MH), with an average particle size 2 μm, was obtained from Liaoning Gaizhou Inorganic Chemical Plant, China. Micronized pristine sepiolite (SP) was kindly supplied by Tolsa SA (Spain). The formulations are listed in Table 1.

Table 1. Formulation of EVA composites

Sample code	EVA [%]	MH [%]	SP [%]
EVA	100	0	0
EVA1	45	55	0
EVA2	45	54	1
EVA3	45	53	2
EVA4	45	52	3
EVA5	45	51	4
EVA6	45	50	5
EVA7	45	47	8

2.2. Sample preparation

Prior to mixing and getting the sepiolite dried the sample was heated first at 100°C for 4 h and cooled slowly then to room temperature under vacuum for 16 h. All samples were melt-mixed via a twin-roll mill (XK-160, made in Jiangdu company, China) at 150°C for 15 min, and then hot-pressed under 10 MPa for 5 min at 140°C taking the shape of sheets according to the prescriptive requirements.

2.3. Characterization

2.3.1. Limiting oxygen index (LOI)

The LOI measurements were carried out using a JF-3 type instrument (Jiangning Analysis Instrument Factory, China) according to GB 2406-80 (ASTM D 2863-77). The samples used for the test were of dimensions 130 mm×6.5 mm×3 mm.

2.3.2. UL-94 test

The UL-94 vertical test was measured on a CZF-2 type instrument (Jiangning Analysis Instrument Factory, China) with sample dimensions of 127 mm×12.7 mm×3 mm according to ASTM D 635-77. UL-94 test results are classified by burning ratings V-0, V-1 or V-2. V-0 rating represents the best flame retardancy of polymeric materials.

2.3.3. Thermal analysis

All runs were carried out on a standard TG-DTA instrument (STA 449C, manufactured by Netzsch, Germany). The samples were examined in Al_2O_3 crucibles (6 mm in diameter and 4 mm in height) in direct contact with the heat-flux plate. Sample weight was approximately 8 mg and the runs carried out in high purity N_2, flowing at 20 cm^3/min. The heating rate was 10°C/min over the range 25–700°C.

2.3.4. Cone calorimeter test

Combustion experiments were performed in a cone calorimeter (Fire Testing Technology, UK) at an incident heat flux of 35 kW/m^2 according to ISO 5660. The bottom and edges of each specimen with a dimension of 100 mm×100 mm×3 mm are wrapped with aluminum foil. All samples were run in duplicate and the average value is reported. Var-

ious parameters can be measured including time to ignition (TTI), heat release rate (HRR) as a function of time, peak of heat release rate (PHRR), mass loss rate, and so on. The experimental error of data from the cone calorimeter was about 5%.

2.3.5. Mechanical properties testing

The tensile strength and elongation at break were measured with an Instron Universal Tester Machine (model 5566) at (25±2)°C with a crosshead speed of 50 mm/min, according to ASTM D 638. In the above-mentioned several measurements, five samples for each test were usually analyzed in order to obtain reproducible results and determine the average values.

3. Results and discussion

3.1. Thermal analysis

To exemplify the thermal behaviour the TG and DTG curves of virgin EVA, MH, EVA/MH and EVA/MH/SP 3% composites are shown in Figures 1 and 2, respectively. On heating the virgin EVA decomposes within the temperature range of 270~520°C in N_2 atmosphere: The first stage (270–395°C) is attributed to the evolution of acetic acid due to the decomposition of vinyl acetate groups

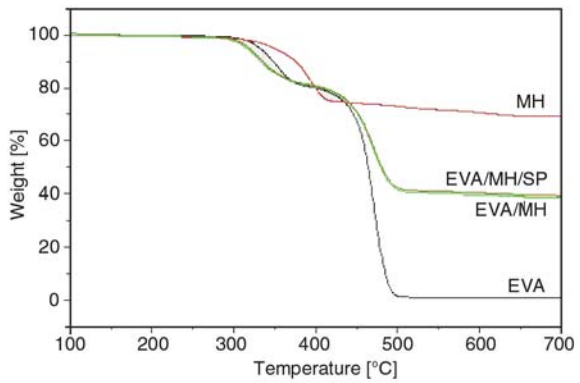

Figure 1. TG curves of virgin EVA, MH, EVA/MH and EVA/MH/SP 3% composites in N_2 at a heating rate of 10°C/min

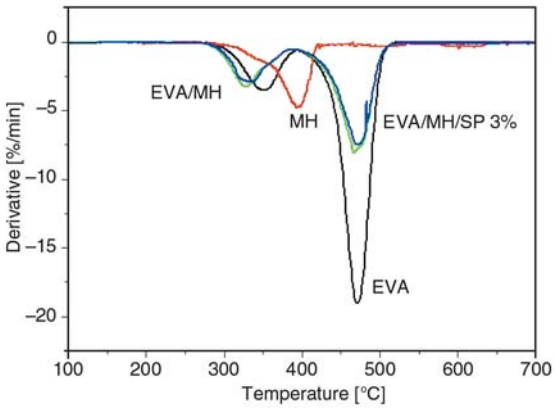

Figure 2. DTG curves of virgin EVA, MH, EVA/MH and EVA/MH/SP 3% composites in N_2 at heating rate of 10°C/min

[22]; the second step (395–520°C) corresponds to the degradation of the polyethylene chains. As reported, the first step of weight loss for EVA/MH composite occurs in the range of 276–388°C due to the dehydration reaction of MH and the loss acetic acid in the EVA at the range of 270–395°C. The second step of weight loss occurs within the temperature range of 388–520°C due to the degradation of the polyethylene chains. In the experiment, the EVA/MH/SP 3% composite shows the same degradation steps as EVA/MH composite.

The 5% mass loss temperature ($T_{5\%}$), the maximum mass loss temperature (T_{max1} and T_{max2}), the maximum rate of weight loss (R_{max}) and residue yield values at 650°C are summarized in Table 2.

As revealed in Table 2 the $T_{5\%}$ for both EVA/MH and EVA/MH/SP 3% composites are similar to one another and deviated about 15°C from the virgin EVA. Regarding the differences in T_{max1} and T_{max2} for both composites, they are only 8 and 5°C, respectively. To access the two composites of EVA/MH and EVA/MH/SP 3% the variation of the R_{max1} (from 3.3 to 2.9%/min) and R_{max2} (from 8.1 to 7.5%/min) and the residue yield at 650°C (from 38.0 to 39.8%) it is true indeed that the participation of sepiolite does decrease the rate of weight loss.

Table 2. TGA data of virgin EVA, MH and their composites under N_2 at heating rate of 10°C/min

Sample	$T_{5\%}$ [°C]	T_{max1}/T_{max2} [°C]	R_{max1}/R_{max2} [%/min]	Residue yield at 650°C [wt%]
EVA	331	351/471	3.5/19.0	0.9
MH	348	396	4.7	69.4
EVA/MH	316	327/467	3.3/8.1	38.9
EVA/MH/SP 3%	317	335/472	2.9/7.5	39.8

$T_{5\%}$ is the temperature at 5% weight loss; T_{max} is the temperature at which the rate of weight loss reaches a maximum.
R_{max} is the maximum rate of weight loss.

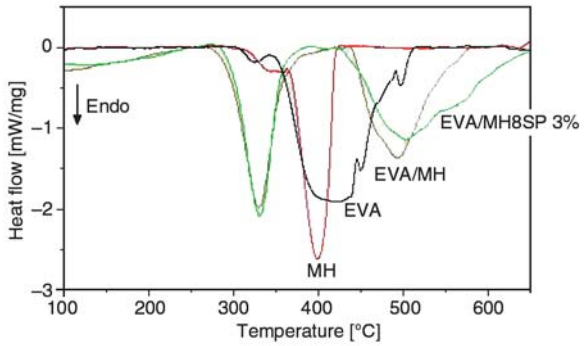

Figure 3. DTA curves of virgin EVA, MH, EVA/MH and EVA/MH/SP 3% composites in N_2 at a heating rate of 10°C/min

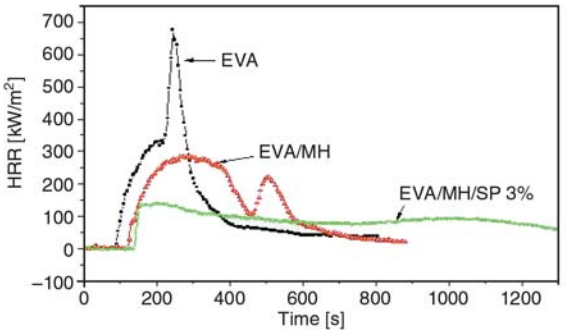

Figure 4. HRR vs time curves for virgin EVA and flame retarded EVA composites (35 kW/m^2)

Four DTA curves are collected in Figure 3. For virgin MH two peaks can be observed, i.e. a shoulder peak at 339°C followed by a strong endothermic peak (maximum at 398°C) due to the dehydration of magnesium hydroxide. EVA curve gives two endothermic peaks within the range of 270–500°C. As for the composite of EVA/MH two endothermic peaks at 328°C corresponding to the dehydration of MH and the peak at 491°C corresponding to the decarboxylation of EVA and thermal decomposition of the polyethylene chains. The DTA curve of the EVA/MH/SP 3% composite almost overlaps with that of the EVA/MH composite in the range of 270–650°C. More specifically, it has been noticed that the second endothermic DTA curves for both composites (Figure 3) are somewhat inconsistent with those in TG and DTG results (Figure 2). According to Tartaglione *et al.* [21], pristine sepiolite undergoes a multi-step dehydration process on heating in the range 50–850°C. Some changes seem to occur and affect the interaction in the system. Further investigation is still ongoing in the lab.

3.2. Cone calorimeter study

Based on the oxygen consumption principle the small-scale cone calorimeter has widely been used to evaluate the characteristics of materials on combustion with the aid of some parameters, like, time to ignition (TTI), peak heat release rate (PHRR) and fire performance index (FPI) (defined as a ratio of TTI/PHRR) [23]. Surely, the greater the FPI value, the better the fire resistance.

Figure 4 presents three HRR curves, of which all data were listed in Table 3. The curve of virgin EVA sample obviously consists of two peaks. The former corresponds to the acetic acid emitted from the thermal decomposition. The latter peak with sharpness (PHRR of 677 kW/m^2) corresponds to the decomposition of the residual ethylenic chain appears over the range of 200~400 s.

The sample EVA1 (55% mass fraction of MH, see Table 1) gives 271 kW/m^2 (PHRR) dramatic declination in HRR with in contrast with virgin EVA. For EVA4 (EVA/MH/SP 3%) the combustion time is extended to 730 s from the 715 s of virgin EVA. EVA4, which is 132 kW/m^2, lower than 271 kW/m^2 of the EVA1 which does not contain sepiolite (Table 3). Among these samples the EVA/MH/SP 3% composite shows the lowest EHC, longest TTI and the highest FPI value 1.045, implying the best fire retardance. The above data indicate that sepiolite has good synergistic flame retardant effect with MH in the EVA/MH/SP composites. From the these results, the synergistic mechanism of sepiolite and MH in the EVA is probably due to the physical process in the condensed phase leading to the formation of a more stable barrier, which efficiently prevents the heat and mass transfer in fire.

The mass loss rate (MLR) is another parameter of importance in the study of combustion. As depicted in Figure 5 quite similar trends for both HRR and MLR curves are seen. Again the EVA/MH/SP 3%

Table 3. Cone data of virgin EVA and flame retardant EVA composites

Sample	TTI [s]	PHRR [kW/m^2]	FPI [m^2·s/kW]	Average EHC [MJ/kg]	Combustion time [s]
EVA	84	677	0.124	28.3	715
EVA1	127	271	0.469	23.4	730
EVA4	138	132	1.045	21.8	1160

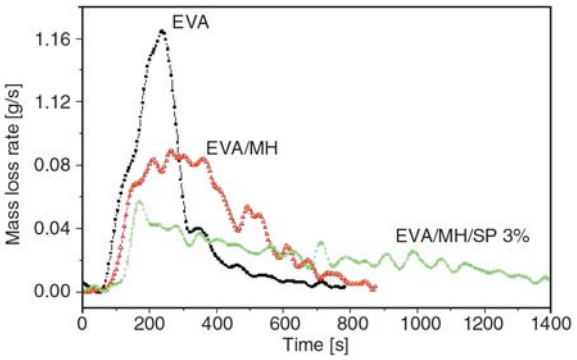

Figure 5. MLS curves for virgin EVA and flame retarded EVA composites (35 kW/m^2)

composite gives lower MLR values than the EVA/MH composite does. These results indicate again that the flame retardant synergistic effects of sepiolite with MH apparently decrease the MLR value of the EVA/MH/SP composite.

Figure 6 shows another plot for total heat release (THR) of all samples. Similar conclusion can be drawn that the THR goes down while the flame retardant MH and MH/SP were incorporated in. Consequently, it is also suggested that the synergistic effect between MH and sepiolite is well deserved in the system.

The emission of smoke is recognized as another important focus in the halogen-free flame retardant system. The mean specific extinction area (SEA), total smoke release (TSR), the mean carbon monoxide yield and carbon dioxide yield derived from cone calorimetry are summarized in Table 4.

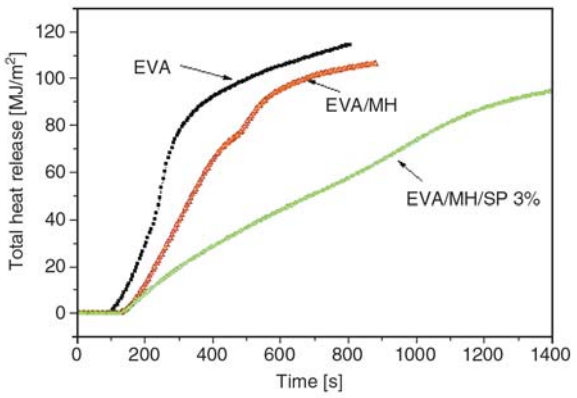

Figure 6. Total heat release (THR) curves for virgin EVA and flame retarded EVA at a heat flux of 35 kW/m^2

It clearly shows that both the smoke emission and carbon oxides yielded during combustion process are depressed by the incorporation of sepiolite.

3.3. LOI and UL 94 testing

Table 5 presents the LOI values and UL 94 testing results of the flame retarded EVA composites at the total amount of 55% mass fraction additives kept constant. As can be seen from Table 5 the LOI value of sample EVA1 containing 55% MH mass fraction shows a value of 31.2% contrasting to the value of 17.8% for the virgin EVA. At 3% mass fraction of sepiolite the LOI reaches up to the maximum of 33.6% and passed the grade V-0. The LOI values begin to drop down since then along with further increase of the sepiolite. Apparently, even at 8% loading the sepiolite seems to be still working, although the LOI value decreases somehow to 32.2%. With 1 and 2% mass fraction of sepiolite the samples reach to pass the grade V-2 and V-1 respectively. Further increasing to 3 and 4%, they are able to pass the V-0 rating as revealed by samples EVA4 and EVA5. It indicates that an appropriate amount of sepiolite may cause the synergistic effect in the EVA/MH/SP composites more efficient.

Table 5. LOI and UL94 test results

Sample code	LOI [%]	UL 94
EVA	17.8	Fail, flame dripping
EVA1	31.2	Fail, flame dripping
EVA2	32.8	V-2
EVA3	33.2	V-1
EVA4	33.6	V-0
EVA5	33.3	V-0
EVA6	33.0	V-1
EVA7	32.2	V-2

3.4. Mechanical properties

At the cutting edge is the mechanical properties of the system, which is of vital importance in applications and may possess itself of some relevance to other properties, say, thermal and/or flame retardant properties. The mechanical properties of vir-

Table 4. Data of smoke obtained from the cone calorimetry

Sample	Mean SEA [m^2/kg]	TSR [m^2/m^2]	Mean CO yield [m^2/m^2]	mean CO_2 yield [m^2/m^2]	CO/CO_2 ratio
EVA	285	1015	0.048	2.35	0.0204
EVA1	269	913	0.039	2.07	0.0188
EVA4	227	689	0.027	1.93	0.0140

Table 6. Mechanical properties of virgin EVA and flame retardant EVAcomposites

Sample code	EVA [%]	MH [%]	SP [%]	Tensile strength [MPa]	Elongation at break [%]	Young's modulus [MPa]
EVA	100	0	0	26.0	960	13.6
EVA1	45	55	0	8.6	148	50.2
EVA2	45	54	1	8.7	114	58.2
EVA3	45	53	2	8.9	118	85.9
EVA4	45	52	3	9.4	201	86.8
EVA5	45	51	4	10.7	136	88.1
EVA6	45	50	5	11.4	168	94.3
EVA7	45	47	8	11.9	146	115.1

gin EVA and formulations with and without sepiolite are given in Table 6.

Taking EVA1 as an example, the addition of MH by great amount into EVA matrix strongly reduces the tensile strength and elongation at break, but oppositely for the Young's modulus. A remarkable change is observed for the Young's modulus, while a small amount of sepiolite is incorporated. The fact that sepiolite has little effect on the elongation at break of the EVA/MH/SP composites, but distinct effect on the Young's modulus probably ascribed to the complex interactions between the polar EVA and the silanol groups of the high aspect-ratio of the sepiolite [24]. Hydrogen bonding may also be expected to take part in between the ester groups of EVA and the characteristic silanol groups.

4. Conclusions

The profitable participation of sepiolite in the EVA/$Mg(OH)_2$ turns out to be a fair opportunity of appearing in public to show the importance of synergistic effect, supported by a many tested techniques, such as, TGA, DTA, CONE calorimetry, LOI, UL 94, etc. An appropriate amount, say 3% mass fraction, of sepiolite enables some properties to be improved, if compared with the case without sepiolite. The synergistic flame retardant mechanism can be explained primarily in terms of the barrier mechanism in the condensed phase, which prevents the happening of heat and mass transfer through the barrier in the fire. In this respect the strengthened mechanical properties through the interactions between the ester groups of EVA and the characteristic silanol groups of the sepiolite, is likely the premise for the improved flame retardance of the composites.

References

[1] Fu M., Qu B.: Synergistic flame retardant mechanism of fumed silica in ethylene-vinyl acetate/magnesium hydroxide blends. Polymer Degradation and Stability, **85**, 633–639 (2004). DOI: 10.1016/j.polymdegradstab.2004.03.002

[2] Riva A., Camino G., Fomperie L., Amigouët P.: Fire retardant mechanism in intumescent ethylene vinyl acetate compositions. Polymer Degradation and Stability, **82**, 341–346 (2003). DOI: 10.1016/S0141-3910(03)00191-5

[3] Carpentier F., Bourbigot S., Bras M. L., Delobel R., Foulon M.: Charring of fire retarded ethylene vinyl acetate copolymer – Magnesium hydroxide/zinc borate formulations. Polymer Degradation and Stability, **69**, 83–92 (2000). DOI: 10.1016/S0141-3910(00)00044-6

[4] Carpentier F., Bourbigot S., Bras M. L., Delobel R.: Rheological investigations in fire retardancy: Application to ethylene-vinyl-acetate copolymer-magnesium hydroxide/zinc borate formulations. Polymer International, **49**, 1216–1221 (2000). DOI: 10.1002/1097-0126(200010)49:10<1216::AID-PI515>3.0.CO;2-S

[5] Durin-France A., Ferry L., Cuesta J. L., Crespy A.: Magnesium hydroxide/zinc borate/talc compositions as flame-retardants in EVA copolymer. Polymer International, **49**, 1101–1105 (2000). DOI: 10.1002/1097-0126(200010)49:10<1101::AID-PI523>3.0.CO;2-5

[6] Ye L., Wu Q., Qu B.: Synergistic effects and mechanism of multiwalled carbon nanotubes with magnesium hydroxide in halogen-free flame retardant EVA/MH/MWNT nanocomposites. Polymer Degradation and Stability, **94**, 751–756 (2009). DOI: 10.1016/j.polymdegradstab.2009.02.010

[7] Zhang Y., Hu Y., Song L., Wu J., Fang S.: Influence of Fe-MMT on the fire retarding behavior and mechanical property of (ethylene-vinyl acetate copolymer/magnesium hydroxide) composite. Polymers for Advanced Technologies, **19**, 960–966 (2008). DOI: 10.1002/pat.1059

[8] Zhang G., Ding P., Zhang M., Qu B.: Synergistic effects of layered double hydroxide with hyperfine magnesium hydroxide in halogen-free flame retardant EVA/HFMH/LDH nanocomposites. Polymer Degradation and Stability, **92**, 1715–1720 (2007).
DOI: 10.1016/j.polymdegradstab.2007.06.004

[9] Gui H., Zhang X., Dong W., Wang Q., Gao J., Song Z., Lai J., Liu Y., Huang F., Qiao J.: Flame retardant synergism of rubber and $Mg(OH)_2$ in EVA composites. Polymer, **48**, 2537–2541 (2007).
DOI: 10.1016/j.polymer.2007.03.019

[10] Laoutid F., Gaudon P., Taulemesse J. M., Cuesta J. M., Velasco J. I., Piechaczyk A.: Study of hydromagnesite and magnesium hydroxide based fire retardant systems for ethylene-vinyl acetate containing organo-modified montmorillonite. Polymer Degradation and Stability, **91**, 3074–3082 (2006).
DOI: 10.1016/j.polymdegradstab.2006.08.011

[11] Huang H., Tian M., Liu L., He Z., Chen Z., Zhang L.: Effects of silicon additive as synergists of $Mg(OH)_2$ on the flammability of ethylene vinyl acetate copolymer. Journal of Applied Polymer Science, **99**, 3203–3209 (2006).
DOI: 10.1002/app.22494

[12] Clerc L., Ferry L., Leroy E., Cuesta J. M.: Influence of talc physical properties on the fire retarding behaviour of (ethylene-vinyl acetate copolymer/magnesium hydroxide/talc) composites. Polymer Degradation and Stability, **88**, 504–511 (2005).
DOI: 10.1016/j.polymdegradstab.2004.12.010

[13] Li Z., Qu B.: Flammability characterization and synergistic effects of expandable graphite with magnesium hydroxide in halogen-free flame-retardant EVA blends. Polymer Degradation and Stability, **81**, 401–408 (2003).
DOI: 10.1016/S0141-3910(03)00123-X

[14] Cross M. S., Cusack P. A., Hornsby P. R.: Effects of tin additives on the flammability and smoke emission characteristics of halogen-free ethylene-vinyl acetate copolymer. Polymer Degradation and Stability, **79**, 309–318 (2003).
DOI: 10.1016/S0141-3910(02)00294-X

[15] Bourbigot S., Duquesne S., Sebih Z., Segura S., Delobel R.: Synergistic aspects of the combination of magnesium hydroxide and ammonium polyphosphate in flame retardancy of ethylene vinyl acetate copolymer. Fire and polymers IV: Materials and concepts for hazard prevention. in 'ACS symposium series' (eds.: Wilkie C. A., Nelson G. L.) Oxford University Press, Washington, vol 922, 200–212 (2006).

[16] Zheng Y., Zheng Y.: Study on sepiolite-reinforced polymeric nanocomposites. Journal of Applied Polymer Science, **99**, 2163–2166 (2006).
DOI: 10.1002/app.22337

[17] Tartaglione G., Tabuani D., Camino G., Moisio M.: PP and PBT composites filled with sepiolite: Morphology and thermal behaviour. Composites Science and Technology, **68**, 451–460 (2008).
DOI: 10.1016/j.compscitech.2007.06.023

[18] Alkan M., Benlikaya R.: Poly(vinyl alcohol) nanocomposites with sepiolite and heat-treated sepiolites. Journal of Applied Polymer Science, **112**, 3764–3774 (2009).
DOI: 10.1002/app.29830

[19] Chen H., Zheng M., Sun H., Jia Q.: Characterization and properties of sepiolite/polyurethane nanocomposites. Materials Science and Engineering A, **445–446**, 725–730 (2007).
DOI: 10.1016/j.msea.2006.10.008

[20] Ma J., Bilotti E., Peijs T., Darr J. A.: Preparation of polypropylene/sepiolite nanocomposites using supercritical CO_2 assisted mixing. European Polymer Journal, **43**, 4931–4939 (2007).
DOI: 10.1016/j.eurpolymj.2007.09.010

[21] Tartaglione G., Tabuani D., Camino G.: Thermal and morphological characterization of organically modified sepiolite. Microporous and Mesoporous Materials, **107**, 161–168 (2008).
DOI: 10.1016/j.micromeso.2007.04.020

[22] Costache M. C., Jiang D. D., Wilkie C. A.: Thermal degradation of ethylene-vinyl acetate copolymer nanocomposites. Polymer, **46**, 6947–6958 (2005).
DOI: 10.1016/j.polymer.2005.05.084

[23] Schartel B., Hull T. R.: Development of fire-retarded materials – Interpretation of cone calorimeter data. Fire and Materials, **31**, 327–354 (2007).
DOI: 10.1002/fam.949

[24] Bilotti E., Zhang R., Deng H., Quero F., Fischer H. R., Peijs T.: Sepiolite needle-like clay for PA6 nanocomposites: An alternative to layered silicates? Composites Science and Technology, **69**, 2587–2595 (2009).
DOI: 10.1016/j.compscitech.2009.07.016

eXPRESS Polymer Letters Vol.4, No.4 (2010) 234–243
Available online at www.expresspolymlett.com
DOI: 10.3144/expresspolymlett.2010.30

Electrical response and functionality of polymer matrix-titanium carbide composites

*C. G. Raptis, A. Patsidis, G. C. Psarras**

Department of Materials Science, School of Natural Sciences, University of Patras, Patras 26504, Hellas (Greece)

Received 21 December 2009; accepted in revised form 12 February 2010

Abstract. The dielectric response and conductivity of polymer matrix-titanium carbide composites was examined by means of Broadband Dielectric Spectroscopy in the frequency range of 10^{-1}–10^{7} Hz and over the temperature range of 40–150°C, varying the filler content. Dielectric data were analyzed via the electric modulus formalism. Recorded relaxations were attributed to interfacial polarization, glass to rubber transition and local motions of polar side groups. Alternating current conductivity varies up to seven orders of magnitude with both frequency and temperature. Direct current conductivity increases with temperature, although the rate of its alteration does not remain constant in the examined temperature range. In the low temperature region (up to 60°C) increases at a higher rate, while right afterwards approaches rather constant values. Finally, in the high temperature range (above 90°C) conductivity raises again but at a lower rate. This behaviour adds functionality to the composites' performance and could be exploited in developing self-current regulators.

Keywords: *polymer composites, dielectric properties, conductivity, titanium carbide*

1. Introduction

Polymer matrix ceramic filler composites receive, recently, increased attention because of their interesting electrical, electronic and functional properties [1–6]. Integrated decoupling capacitors, acoustic emission sensors, electronic packaging, self-current regulators, self-heating systems, elements for circuit protection, electrostriction artificial muscles or skins and memory switches are some possible applications [1–6]. Moreover, electrical properties such as dielectric permittivity and conductivity can be suitably adjusted by simply controlling the type and the amount of ceramic inclusions.

Titanium carbide is an important material for technological applications because of its high melting point, hardness, elastic modulus, electrical conductivity and low coefficient of thermal expansion. Composite systems consisting of a polymer matrix and conductive particles of titanium carbide have been considered as a novel class of smart materials, because of their ability to switch from negative to positive temperature coefficient of conductivity [7–9]. Negative temperature coefficient of conductivity (NTCC) is useful in applications such as self-controlled heaters, current limiters, sensors, thermistors and over current protectors, while it is considered as detrimental in cable engineering [10]. On the other hand, positive temperature coefficient of conductivity (PTCC) is important in electromagnetic shielding and in antistatic materials [11, 12]. Switching, between NTCC to PTCC and vice versa under controlled conditions adds functionality to the performance of the composite systems and by that increases their technological impact.

In the present study, polymer matrix – ceramic TiC composites were prepared at different filler concentrations. Their electrical response was examined by means of Broadband Dielectric Spectroscopy (BDS), over a wide temperature range (40 to 160°C) and in the frequency range of 10^{-1} Hz to 10 MHz.

*Corresponding author, e-mail: G.C.Psarras@upatras.gr

Dielectric data are analyzed by means of electric modulus and ac conductivity formalisms.

2. Experimental

2.1. Samples preparation

Composite specimens were prepared by employing commercially available materials. In particular a low viscosity epoxy resin (Epoxol 2004A, Neotex S.A., Athens, Greece) was used as a prepolymer, with Epoxol 2004B as curing agent, operating at a slow rate, supplied by the same company. Titanium carbide was purchased by Sigma-Aldrich. The mean particle diameter was less than 2 μm. The preparation procedure involved mixing of the resin with the curing agent in a 2:1 [w/w] ratio and then adding, while the polymer system was still in the liquid state, various amounts of the ceramic powder. Stirring at a low rate and degassing the mixtures in a vacuum-oven were also included in the preparation procedure. The content of titanium carbide in the produced specimens was 20, 30, 40 and 50 parts per hundred [phr] of resin and hardener. The initial curing took place at ambient for a week, followed by post-curing at 100°C for 4 hours. The density of the produced samples is listed in Table 1. The morphology of the produced samples was checked for voids and clusters, by means of Scanning Electron Microscopy (Leo Supra 35VP). In all cases, the distribution of the ceramic particles is considered as satisfactory.

2.2. Thermal characterisation

A Diamond (Perkin Elmer, Shelton, USA) Differential Scanning Calorimeter operating at a scan rate of 10°C/min was used to characterise thermal transitions of the employed epoxy resin and composite systems. Samples were placed within an aluminum crucible, while an empty aluminum crucible was serving as reference material. Temperature was varied from ambient to 200°C. Glass transition temperature (T_g) was determined via the point of inflexion of the transition, by employing suitable software supplied by Perkin Elmer. T_g of pure epoxy resin was found to be 56.6°C. Table 1 summarizes glass transition temperature for all the examined systems.

Table 1. Density and glass transition temperature for all the examined systems

Sample	Density [g/cm^3]	Glass transition temperature, T_g [°C]
Epoxy	1.046	56.6
Epoxy + 20 phrTiC	1.092	52.1
Epoxy + 30 phr TiC	1.236	51.5
Epoxy + 40 phr TiC	1.362	50.7
Epoxy + 50 phr TiC	1.400	50.5

2.3. Dielectric measurements

Dielectric measurements were conducted by means of Broadband Dielectric Spectroscopy (BDS) in the frequency range of 0.1 Hz to 10 MHz, using Alpha-N Frequency Response Analyser, supplied by Novocontrol Technologies (Hundsagen, Germany). The dielectric cell was a three terminal guarded system constructed according to the ASTM D150 specifications. The samples being tested were put between metal electrodes and problems arising from possible electrode polarisation were excluded by analysing data by means of electric modulus formalism [3, 13, 14]. Experimental data were obtained by conducting isothermal frequency scans, for each of examined specimens, from ambient to 150°C with a temperature step of 10°C. The amplitude of the applied test voltage was kept constant at 1000 mV, while the mean sample thickness was approximately 3 mm. In the present study, dc conductivity is considered as equal to the value of $\sigma(\omega)$ at $f = 0.1$ Hz.

3. Results and discussion

Figure 1 depicts images from Scanning Electron Microscopy for all the examined composites. As it can be seen the distribution of TiC particles appears to be a homogeneous, while some agglomerates are present even at low concentration of the ceramic filler.

The variation of the real part of dielectric permittivity with frequency at 50°C for all the tested systems is depicted in Figure 2. Permittivity diminishes with frequency, because of the inertia of the permanent and induced dipoles to follow the alternation of the alpplied field, reflecting the reduction of polarization. Values of (ε') increase with filler content, since the composites become more conductive, their heterogeneity raises, charges accumulate at the interfaces of the system and thus interfacial polarization enhances.

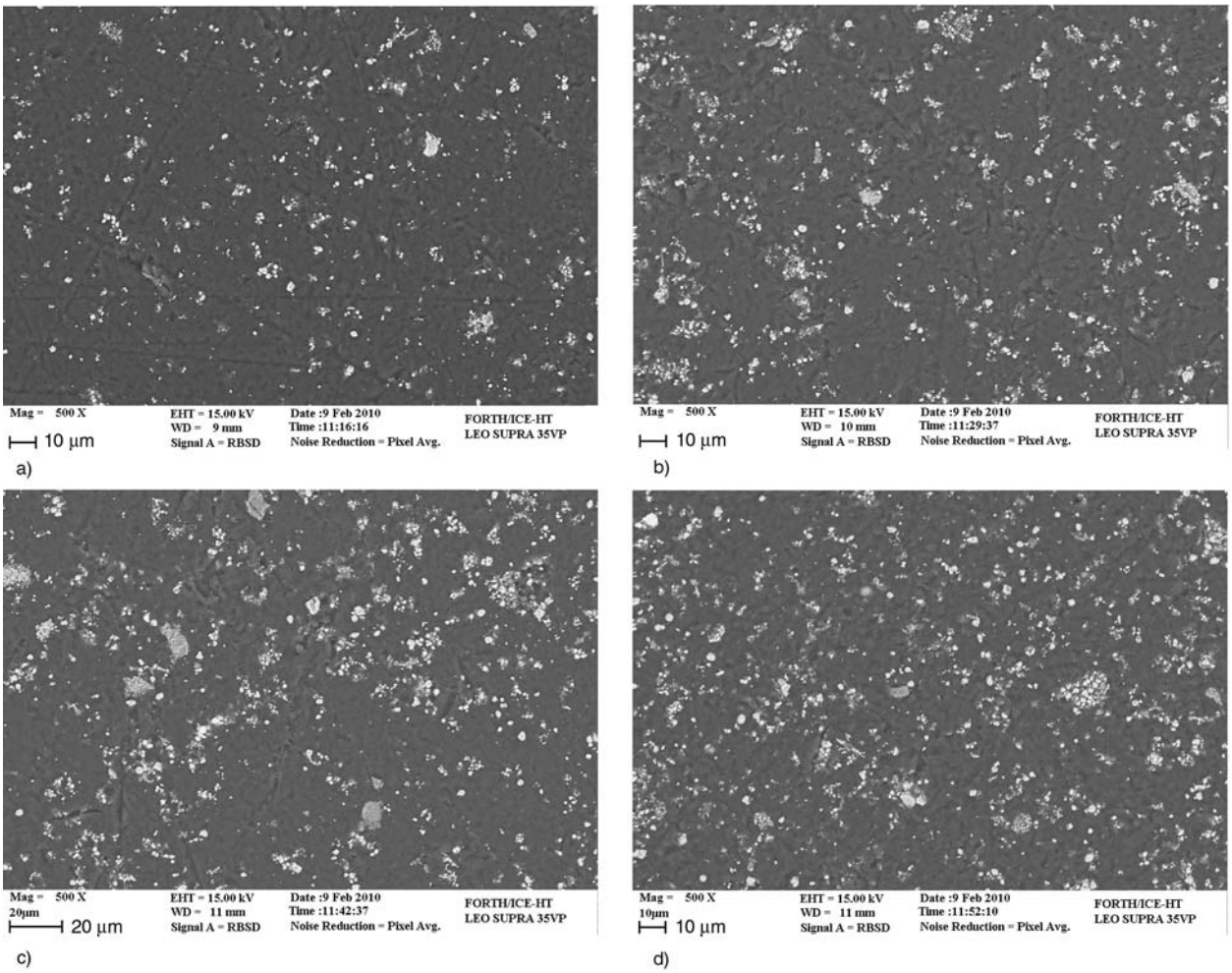

Figure 1. Scanning electron microscopy images of the specimens with (a) 20 phr, (b) 30 phr, (c) 40 phr and (d) 50 phr in TiC content

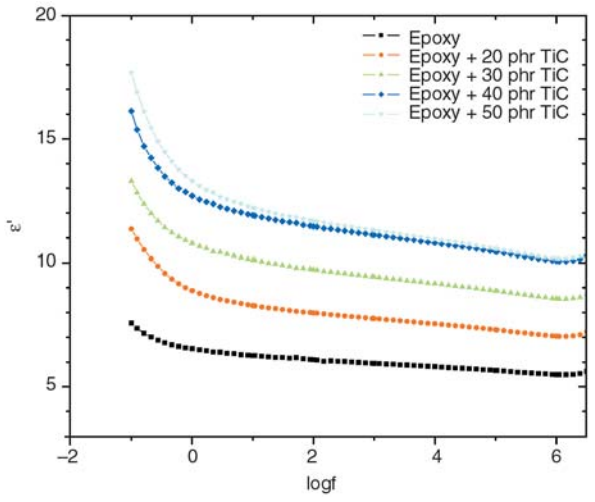

Figure 2. Real part of permittivity versus frequency for all the tested specimens at 50°C

In polymer composite systems dielectric relaxation effects arise from both the polymer matrix and the interaction with the reinforcing phase. In the present study dielectric data were first expressed in terms of real and imaginary part of dielectric permittivity and then transformed via Equation (1) to the electric modulus presentation. Different formalisms, such as dielectric permittivity, electric modulus and ac conductivity, are able to describe electrical phenomena present in composite systems. However, under some circumstances a specific formalism could prove to be more efficient in extracting information concerning the occurring physical mechanisms. In this study, the dielectric response of all the examined systems was investigated via the electric modulus formalism. Arguments for the resulting benefits of the electric modulus presentation have been exhibited and discussed elsewhere [13–15]. Electric modulus is defined as the inverse quantity of complex permittivity, as shown in Equation (1):

$$M^* = \frac{1}{\varepsilon^*} = \frac{1}{\varepsilon' - j\varepsilon''} = \frac{\varepsilon'}{\varepsilon'^2 + \varepsilon''^2} + j\frac{\varepsilon''}{\varepsilon'^2 + \varepsilon''^2} = M' + jM'' \quad (1)$$

where ε′, M' and ε″, M'' are the real and the imaginary parts of dielectric permittivity and electric modulus respectively.

Figures 3 and 4 present isothermal scans of the real and imaginary part of electirc modulus for the composites with 20 and 50 phr in TiC particles, at temperatures varying from 40 to 150°C. The existence of a clear 'step-like' transition from low to high values of (M'), at moderate frequencies, is evident in Figures 3a and 4a. Two additional transitions are detected in the high and the low frequency region respectively. The latter becomes more evident at high temperatures. All three transitions are related to dipolar relaxations effects occurring in the examined systems, and thus should be accompanied by the formation of dielectric loss peaks in the respective $M'' = F(\log f)$ plots. In Figures 3b and 4b loss peaks can be observed in the frequency range where transitions occur. Note that at the high frequency edge a tendency for the formation of the third peak is recorded. Because of frequency-temperature superposition, loss peaks shift to higher frequencies as the temperature is raised. Shift rate of the main peak, in the intermediate frequency zone, appears to be constant in the temperature interval from 50 to 100°C, while at higher temperatures peak shift rate diminishes with the simultaneous increase of the loss modulus maxima. Figure 5 depicts comparative plots of the real and imaginary part of electric modulus as a function of frequency, for all the examined composites, at 150°C. The presence of, at least, two relaxation processes is evident. Loss maxima of the relaxation process recorded in the intermediate frequency region diminish monotically with filler concentration. The Cole-Cole plots of all the examined specimens, at 150°C, are presented in Figure 6. In the Cole-Cole presentation, each relaxation process corresponds to a semicircle, which might appear completed or even uncompleted. In Figure 6, two distinct semi-

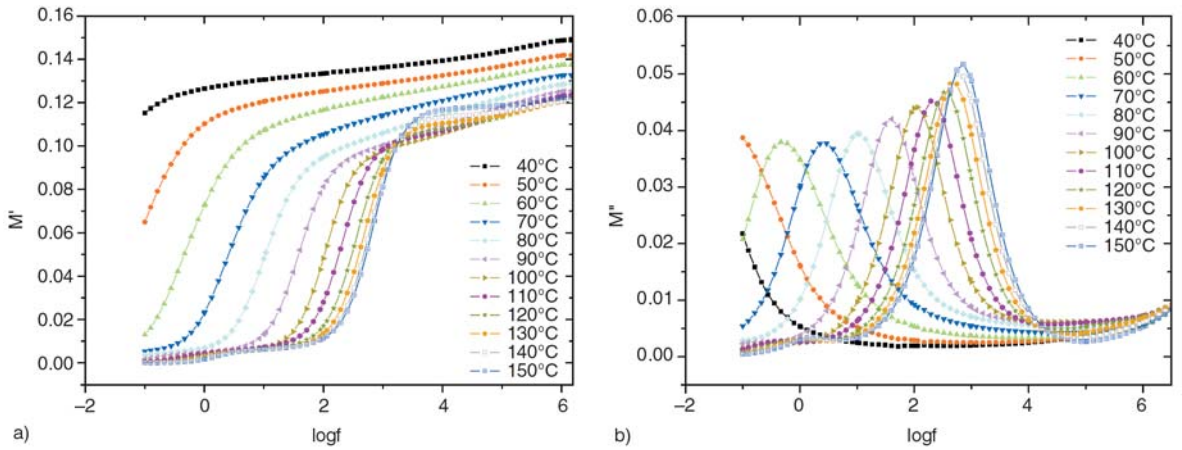

Figure 3. Real (a) and imaginary (b) part of electric modulus versus frequency for the specimen with 20 phr in TiC content

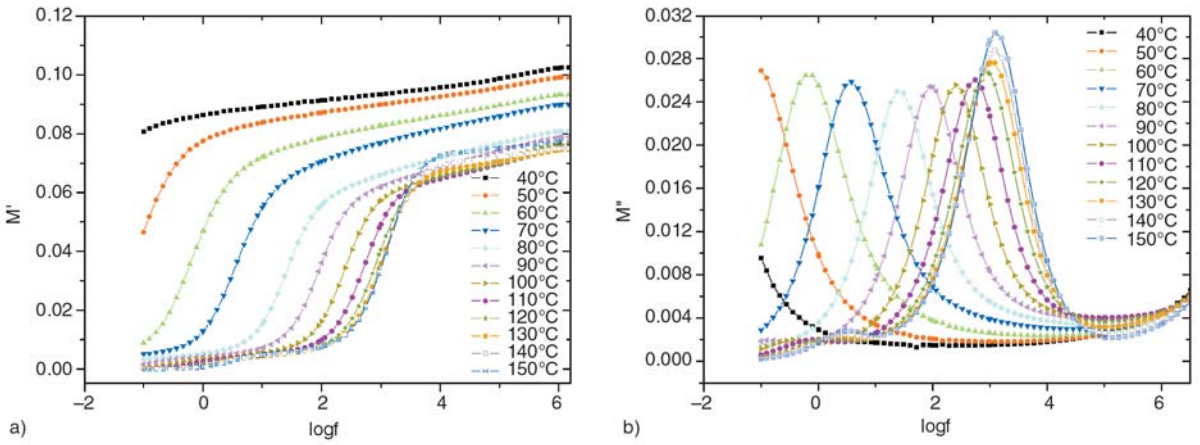

Figure 4. Real (a) and imaginary (b) part of electric modulus versus frequency for the specimen with 50 phr in TiC content

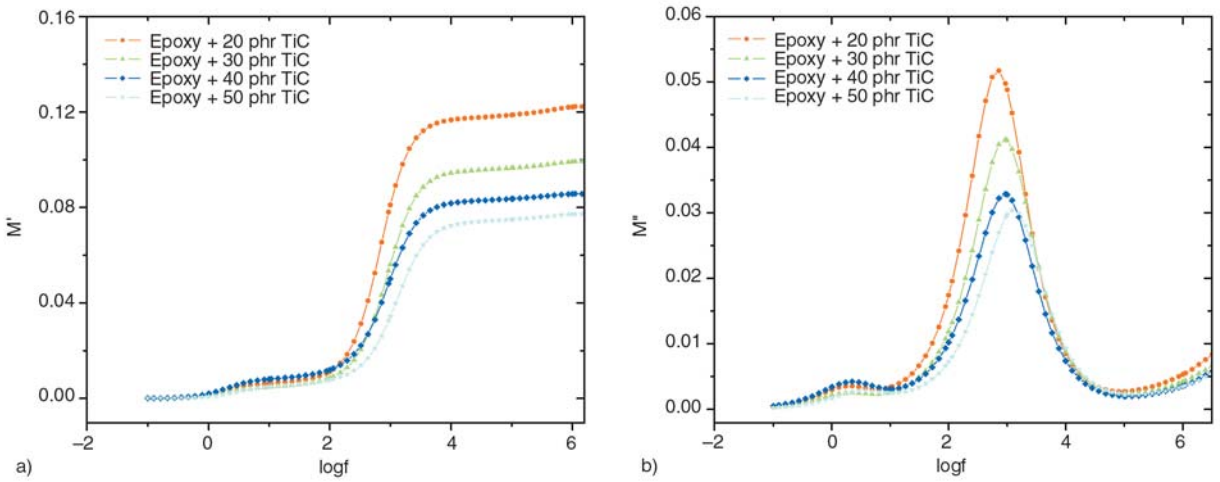

Figure 5. Real (a) and imaginary (b) part of electric modulus versus frequency for all the tested composites at 150°C

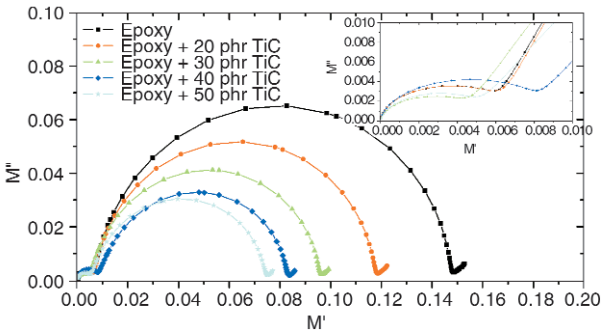

Figure 6. Cole-Cole plots for all the tested specimens at 150°C

circles are clearly formed, in the low and intermediate frequency zone, while in the high frequency edge the initiation of a third semicircle is evident. In the low frequency range, traces of the small semicircle (inset of Figure 6) pass from the origin of the graph, implying that this is the slowest relaxation process present in the examined systems.

Assigning dielectric relaxation processes to specific physical mechanisms is not an easy procedure and presupposes experience and an overall inspection of the dielectric performance. Aforementioned remarks lead to the following assignment of dielectric processes. Ascending frequency, at constant temperature, the recorded relaxation processes are attributed to Interfacial Polarization (IP) known also as Maxwell-Wagner-Sillars (MWS) effect, glass to rubber transition (α-mode) of the polymer matrix and local rearrangements of polar side groups of the main polymer chain (β-mode). Interfacial polarization is present in heterogeneous systems, and its origin is attributed to the accumulation of mobile charges at the interface of the composite system. Charges at the polymer matrix/TiC particles interface form large dipoles, which attempt to align themselves parallel to the applied field. However, induced dipoles exhibit inertia in following the alternation of the applied field, and thus the resulting relaxation process is characterised by enhanced relaxation time and recorded at low frequencies and high temperatures.

The temperature dependence of electric modulus loss index (M''), at constant frequency, for all the examined systems is presented in Figure 7. The main dielectric loss peak, which is recorded in the dielectric spectra of all specimens in the intermediate frequency region, is now formed in the vicinity of 55°C for the unfilled epoxy resin, and a few degrees lower in the case of the composite systems, at $f = 0.1$ Hz in Figure 7a. In dielectric loss versus temperature spectra is a rule of thumb to determine glass transition temperature from the position of the relative loss peak (α-relaxation process) at constant frequency equal to 0.1 Hz [16–19]. Derived value for glass transition temperature, via DSC measurements, of pure polymer matrix (56.6°C) appears to be very close with the position of loss peak in Figure 7a, supporting further the assignment of this process to glass to rubber transition of the epoxy resin. At temperatures near T_g, polymer acquire sufficient thermal energy, allowing large parts of macromolecular chains to relax simultaneously in a cooperative motion and thus giving rise to α-relaxation process. As already stated the corresponding peak of composite systems in Figure 7a, is formed at slightly lower temperatures and appears not to vary with the filler content. In polymer matrix/ceramic filler composites variation of glass transition temperature between pure polymer and com-

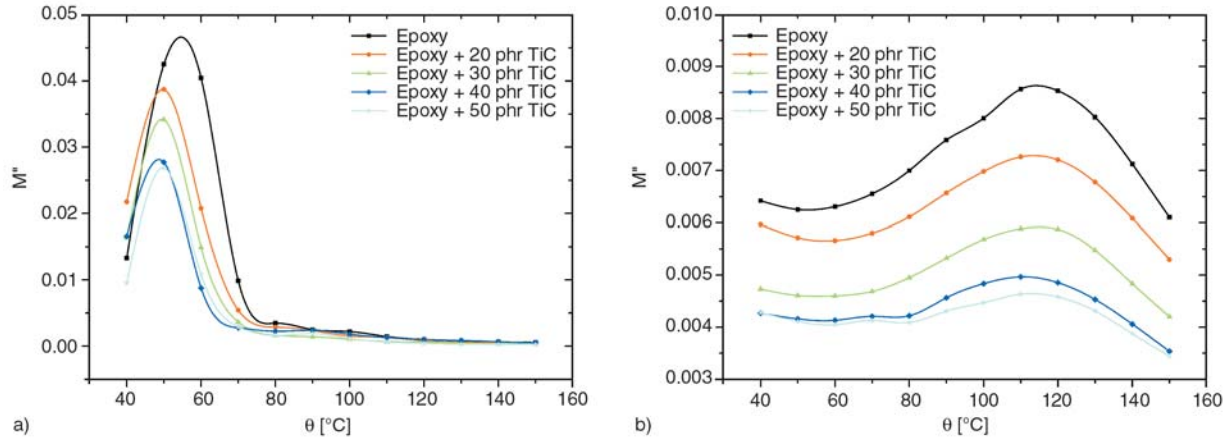

Figure 7. Imaginary part of electric modulus as a function of temperature, for all the tested specimens, at (a) $f = 0.1$ Hz and (b) $f = 1$ MHz

posite systems have been observed and reported [20–22]. These variations have been attributed to interactions between polymer matrix/ceramic filler and to the wetting level of inclusions. Figure 7b depicts the variation of loss modulus index with temperature, at 1 MHz. The presence of a weak relaxation mechanism becomes evident via the formation of a broad peak, which maxima diminish with filler content. This is a fast relaxation process, characterised by a sort relaxation time, which is attributed to rearrangement of polar side groups of the polymer chain (β-mode). It is also evident in the spectrum of pure matrix and becomes weaker with filler content, indicating that ceramic particles may exert restrictions on local motions.

Figure 8 presents the temperature dependence of loss peak position, or in other words the relaxation rate, for both IP and α-relaxation processes. Because of the frequency and temperature superposition, loss peaks shift to higher frequencies when temperature is raised (Figures 3 and 4). However, peak shift rate varies from process to process, although in some cases this rate is constant and the relative process appears to be temperature independent [23]. Interfacial polarization follows Arrhenius type behaviour, described by Equation (2):

$$f_{\max} = f_0 \exp\left(-\frac{E_A}{k_B T}\right) \tag{2}$$

where E_A is the activation energy of the process, f_0 pre-exponential factor, k_B the Boltzmann constant and T the absolute temperature. Peak shift rate of α-relaxation process is not constant and can be described via Vogel-Fulcher-Tamann equation, which considers that relaxation rate increases rapidly at lower temperatures because of the reduction of free volume. The following relation expresses VFT equation (Equation (3)):

$$f_{\max} = f_0 \exp\left(-\frac{AT_0}{T - T_0}\right) \tag{3}$$

where f_0 is a pre-exponential factor, A a constant being the measure of activation energy, T_0 the Vogel temperature or ideal glass transition temperature and T the absolute temperature. Values of activation energy for IP process calculated via linear regression of Equation (2) for all the examined systems, as well as fitting parameters for α-mode determined via Equation (3), are listed in Table 2. It should be noted that activation energy of the IP (MWS) process increases with TiC content, with the only exception of the specimen with 30 phr titanium carbide. The increase of activation energy

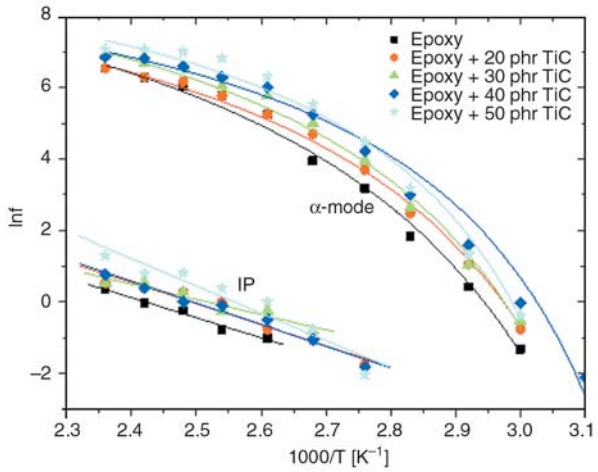

Figure 8. Loss peak position as a function of the reciprocal temperature for the IP and α-relaxation processes, for all the examined systems

Table 2. Values of activation energy, calculated via Equation (2), for the IP process, and fitting parameters of Equation (3) for α-mode

Sample	α-mode		IP/E_A [eV]
	T_0 [K]	A	
Epoxy	285	2.1	0.485
Epoxy + 20 phr TiC	280	1.7	0.511
Epoxy + 30 phr TiC	278	1.6	0.369
Epoxy + 40 phr TiC	277	1.3	0.525
Epoxy + 50 phr TiC	271	1.3	0.660

signifies enhanced heterogeneity. The maximum value of the parameter T_0, for the α-mode, corresponds to the unfilled epoxy, and then decreases gradually with filler content, being in qualitative accordance with the results of Figure 7a. Finally, the parameter A diminishes systematically with filler content, indicating that the required amount of thermal energy for the agitation of α-relaxation process decreases with TiC concentration. Recalling Figure 7a, it seems that the reduction of both activation energy (via parameter A) and glass transition temperature in the composite systems, compared to the corresponding values of pure polymer matrix, is in accordance with the $M'' = F(\theta)$ data. This behaviour could be considered as indirect indication for the existence of weak interactions between ceramic filler and polymer macromolecules, and at the same time for moderate adhesion of TiC particles by the matrix.

The dispersion of ac conductivity with frequency and temperature for the systems with 20 and 50 phr in TiC particles is depicted in Figure 9. Alternating current conductivity has been calculated from the dielectric loss, according to Equation (4):

$$\sigma_{AC} = \varepsilon_0 \omega \varepsilon'' \tag{4}$$

where $\varepsilon_0 = 8.854 \cdot 10^{-12}$ F/m is the permittivity of free space, (ε'') the permittivity loss index and ω the angular frequency of the applied field. The examined systems exhibit a strong dispersion of ac conductivity with frequency and temperature approaching seven orders of magnitude. At low frequencies σ_{AC} remains constant or tends to acquire constant values. At higher frequencies becomes strongly frequency dependent, varying approximately as a power of the frequency. When the frequency of the applied field is low, charge carries are forced to drift over large distances addressing difficulties because of the insulating nature of the matrix. On the other hand, when the frequency of the applied field is high the mean displacement of the charges is significantly reduced and at the same time the transport rate between adjacent conductive sites is raised leading to enhanced conductivity. The formed peaks in the intermediate frequency zone are attributed to the presence of dielectric relaxation processes. Finally, the influence of temperature is more evident in the low frequency region. Variation of ac conductivity with frequency at low and high frequencies is in accordance with Equation (5), which is also known as the 'ac universality law' [24], which is expressed mathematically as:

$$\sigma_{AC} = \sigma_{DC} + K\omega^s \tag{5}$$

where σ_{DC} is the $\omega \to 0$ limiting value of σ_{AC} and K, s parameters depending on temperature and filler content [25]. Deviations occurring in the intermediate frequency region are attributed to the unsuit-

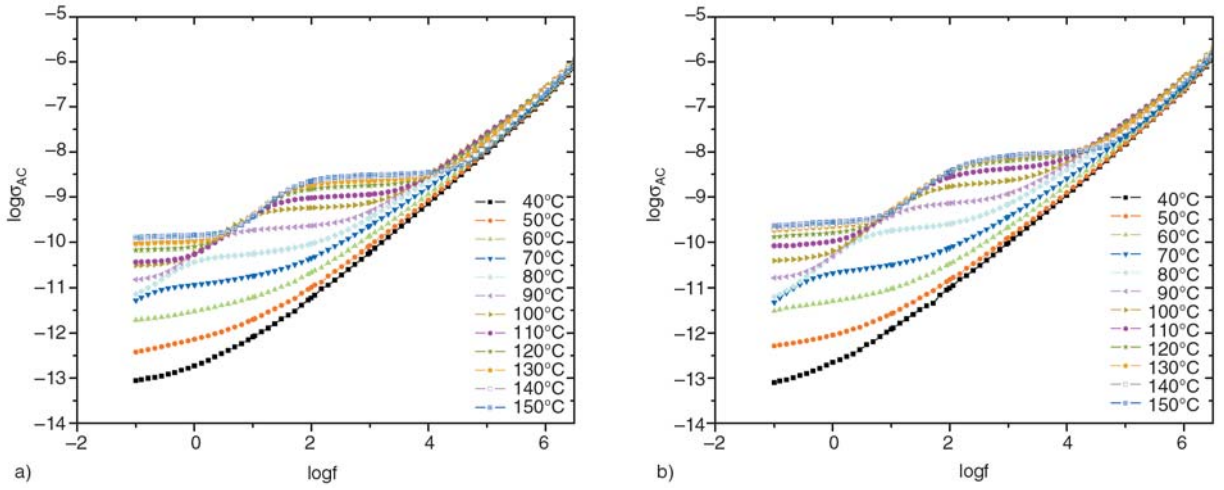

Figure 9. Ac conductivity versus frequency for the specimens with (a) 20 phr and (b) 50 phr in TiC content, at various temperatures

ability of 'ac universality law' to describe dielectric phenomena. Analogous deviations in different type polymer matrix composites have been reported in the past [26, 27].

Figure 10a presents the influence of temperature upon dc conductivity. Extrapolation of ac conductivity to zero frequency enables the evaluation of dc conductivity. In this study, dc conductivity is considered as equal to the value of $\sigma(\omega)$ at the lowest measured frequency ($f = 0.1$ Hz). Up to 60°C, a temperature very close to T_g, conductivity increases with temperature ($d\sigma/d\theta > 0$) indicating a typical insulating or semiconductive behaviour. At intermediate temperatures, higher than the glass transition temperature of the matrix, conductivity stops increasing approaching a plateau, which extends to a range of 30°C (almost from 60 to 90°C). The thermal expansion of the polymer matrix and the consecutive disruption of conductive paths could be considered as responsible for this behaviour. At higher temperatures conductivity raises again. In this temperature range, polymer's mobility is further increased. Transport of charges is facilitated since they are subjected to higher thermal activation and the enhanced mobility of macromolecules allows the formation of new conductive paths. The dependence of conductivity on the reciprocal temperature for all the examined systems is depicted in Figure 10b. The temperature dependence of conductivity in insulators and semiconductors follows the Equation (6) [28, 29]:

$$\sigma(T) = \sigma^0 \exp\left[-\frac{E_A}{k_B T}\right] \quad (6)$$

where σ^0 is a pro-exponential factor, E_A the activation energy of the process, k_B the Boltzmann constant and T the absolute temperature. Assuming, at first approximation, that data can be described by Equation (6) in the regions of low and high temperatures, the activation energies of the occurring processes at these two ranges can be evaluated. Obtained values for each of the examined systems are listed in Table 3. As it can be seen, at temperatures well above T_g, conduction process appears to be easier, and is characterised by smaller activation energies. Finally, charge transport process in the low temperature range requires increased amount of thermal agitation for its own onset.

In the examined set of composites no NTCC effect was observed. However, the variation of the curvatures in the $\sigma_{DC} = F(T)$ plots for all composite specimens, at the same temperature range (60–90°C), and the existence of a common point of inflexion at 80°C offer functionality to the composites performance. The latter is related to the possibility to tune the conductivity of the composites via controlling temperature, without any external adjusting device or circuit. This behaviour could be proved very useful in developing self-current regulating systems. Under this point of view more research should be

Table 3. Values of activation energy, calculated via Equation (6), for the conduction processes at low and high temperatures

Sample	E_A [eV] (40–70°C)	E_A [eV] (80–150°C)
Epoxy	1.540	0.531
Epoxy + 20 phr TiC	1.287	0.525
Epoxy + 30 phr TiC	1.369	0.500
Epoxy + 40 phr TiC	1.175	0.477
Epoxy + 50 phr TiC	1.306	0.661

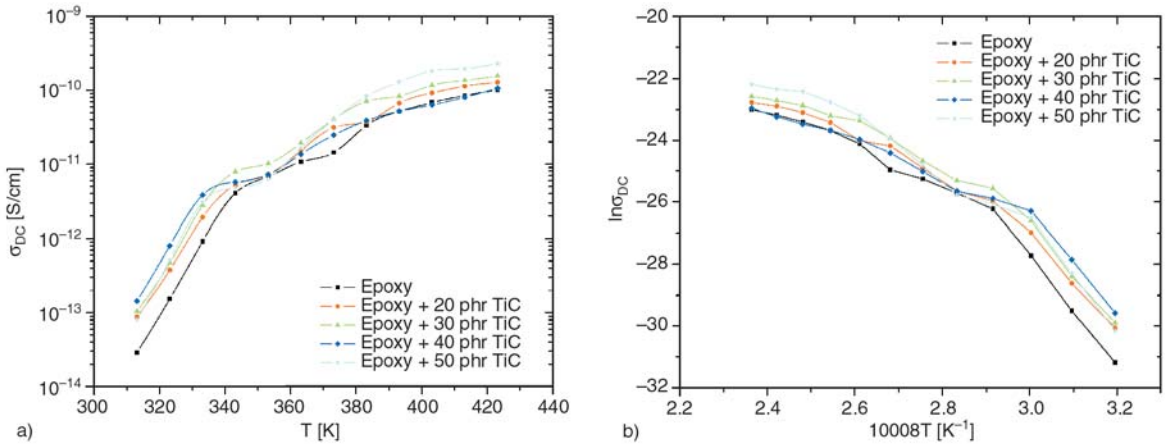

Figure 10. Dc conductivity as a function of (a) temperature and (b) reciprocal of temperature for all the tested systems

carried out on this topic in order to clarify the occurring physical mechanisms.

4. Conclusions

Based on the experimental data of dielectric behaviour and conductivity of the tested epoxy resin/TiC composites, the following conclusions can be drawn.

– Ascending frequency, at constant temperature, the recorded processes are attributed to interfacial polarization, glass to rubber transition of the polymer matrix and local motions of polar side groups.
– Decreasing of T_g in polymer composites is attributed to enhancement in cooperative segmental mobility resulting from weak interactions between polymer chains and TiC particles and to the moderate adhesion level of the inclusions by the matrix.
– All systems exhibit strong dispersion of ac conductivity (up to 7 orders of magnitude) with frequency and temperature.
– Direct current conductivity of the composites is temperature dependent and, in general, increases with temperature. In the low temperature range conductivity alters with temperature at a higher rate, while in the intermediate zone appears to remain constant, and in the high temperature region conductivity increases again, but at lower rate. Tuning conductivity with temperature offers functionality to the composite systems, which could be exploited in high tech applications.

References

[1] Chahal P., Tummala R. R., Allen M. G., Swaminathan M.: A novel integrated decoupling capacitor for MCM-L technology. IEEE Transactions on Components Packaging and Manufacturing Technology Part B-Advanced Packaging, **21**, 184–193 (1998). DOI: 10.1109/96.673707

[2] Dias C. J., Igreja R., Marat-Mendes R., Inacio P., Marat-Mendes J. N., Das-Gupta D. K.: Recent advances in ceramic-polymer composite electrets. IEEE Transactions on Dielectrics and Electrical Insulation, **11**, 35–40 (2004). DOI: 10.1109/TDEI.2004.1266314

[3] Kontos G. A., Soulintzis A. L., Karahaliou P. K., Psarras G. C., Georga S. N., Krontiras C. A., Pisanias M. N.: Electrical relaxation dynamics in TiO_2-polymer matrix composites. Express Polymer Letters, **1**, 781–789 (2007). DOI: 10.3144/expresspolymlett.2007.108

[4] Chanmal C. V., Jog J. P.: Dielectric relaxations in PVDF/$BaTiO_3$ nanocomposites. Express Polymer Letters, **2**, 294–301 (2008). DOI: 10.3144/expresspolymlett.2008.35

[5] Patsidis A., Psarras G. C.: Dielectric behaviour and functionality of polymer matrix-ceramic $BaTiO_3$ composites. Express Polymer Letters, **2**, 718–726 (2008). DOI: 10.3144/expresspolymlett.2008.85

[6] Wang F., Zhou D., Gong S.: Dielectric behavior of TiC-PVDF nanocomposites. Physica Status Solidi Rapid Research Letters, **3**, 22–24 (2009). DOI: 10.1002/pssr.200802232

[7] Liu Y., Oshima K., Yamauchi T., Shimomura M., Miyauchi S.: Temperature-conductivity characteristics of the composites consisting of fractionated poly(3-hexylthiophene) and conducting particles. Journal of Applied Polymer Science, **77**, 3069–3076 (2000). DOI: 10.1002/1097-4628(20000929)77:14<3069::AID-APP70>3.0.CO;2-B

[8] Sung Y. K., El-Tantawy F.: Novel smart polymeric composites for thermistors and electromagnetic wave shielding effectiveness from TiC loaded styrene-butadiene rubber. Macromolecular Research, **10**, 345–358 (2002).

[9] El-Tantawy F.: New double negative and positive temperature coefficients of conductive epdm rubber TiC ceramic composites. European Polymer Journal, **38**, 567–577 (2002). DOI: 10.1016/S0014-3057(01)00208-7

[10] El-Tantawy F.: Joule heating treatments of conductive butyl rubber/ceramic superconductor composites: A new way for improving the stability and reproducibility? European Polymer Journal, **37**, 565–574 (2001). DOI: 10.1016/S0014-3057(00)00134-8

[11] Kataoka M., Masuko T.: PTC characteristics of (TiC/polyethylene) conductive composites in relation to their particle-filled structures. Electrical Engineering in Japan, **152**, 1–9 (2005). DOI: 10.1002/eej.20115

[12] Ghosh P., Chakrabarti A.: Conducting carbon black filled EPDM vulcanizates: Assessment of dependence of physical and mechanical properties and conducting character on variation of filler loading. European Polymer Journal, **36**, 1043–1054 (2000). DOI: 10.1016/S0014-3057(99)00157-3

[13] Tsangaris G. M., Psarras G. C., Kouloumbi N.: Electric modulus and interfacial polarization in composite polymeric systems. Journal of Materials Science, **33**, 2027–2037 (1998). DOI: 10.1023/A:1004398514901

[14] Psarras G. C., Manolakaki E., Tsangaris G. M.: Electrical relaxations in polymeric particulate composites of epoxy resin and metal particles. Composites Part A: Applied Science and Manufacturing, **33**, 375–384 (2002).
DOI: 10.1016/S1359-835X(01)00117-8

[15] Psarras G. C., Gatos K. G., Karahaliou P. K., Georga S. N., Krontiras C. A., Karger-Kocsis J.: Relaxation phenomena in rubber/layered silicate nanocomposites. Express Polymer Letters, **1**, 837–845 (2007).
DOI: 10.3144/expresspolymlett.2007.116

[16] Hedvig P.: Dielectric spectroscopy of polymers. Adam Hilger, Bristol (1977).

[17] McCrum N. G., Read B. E., Williams G.: Anelastic and dielectric effects in polymer solids. Wiley, London (1967).

[18] Ngai K. L.: Test of expected correlation of polymer segmental chain dynamics with temperature-dependent time-scale shifts in concentrated solutions. Macromolecules, **24**, 4865–4870 (1991).
DOI: 10.1021/ma00017a023

[19] Korzhenko A., Tabellout M., Emery J. R.: Influence of a metal-polymer interfacial interaction on dielectric relaxation properties of polyurethane. Polymer, **40**, 7187–7195 (1999).
DOI: 10.1016/S0032-3861(99)00055-5

[20] Grohens Y., Brogly M., Labbe C., David M-O., Schultz J.: Glass transition of stereoregular poly(methyl methacrylate) at interfaces. Langmuir, **14**, 2929–2932 (1998).
DOI: 10.1021/la971397w

[21] Grohens Y., Hamon L., Reiter G., Soldera A., Holl Y.: Some relevant parameters affecting the glass transition of supported ultra-thin polymer films. The European Physical Journal E: Soft Matter and Biological Physics, **8**, 217–224 (2002).
DOI: 10.1140/epje/i2001-10088-4

[22] Hartmann L., Gorbatschow W., Hauwede J., Kremer F.: Molecular dynamics in thin films of isotatctiv poly(methyl methacrylate). The European Physical Journal E: Soft Matter and Biological Physics, **8**, 145–154 (2002).
DOI: 10.1140/epje/i2001-10073-y

[23] Soulintzis A., Kontos G., Karahaliou P. K., Psarras G. C., Georga S. N., Krontiras C. A.: Dielectric relaxation processes in epoxy resin-ZnO composites. Journal of Polymer Science Part B: Polymer Physics, **47**, 445–454 (2009).
DOI: 10.1002/polb.21649

[24] Jonscher A. K.: Universal relaxation law. Chelsea Dielectric Press, London (1996).

[25] Tsangaris G. M., Psarras G. C., Manolakaki E.: DC and AC conductivity in polymeric particulate composites of epoxy resin and metal particles. Advanced Composites Letters, **8**, 25–29 (1999).

[26] Psarras G. C., Manolakaki E., Tsangaris G. M.: Dielectric dispersion and ac conductivity in – iron particles loaded – polymer composites. Composites Part A: Applied Science and Manufacturing, **34**, 1187–1198 (2003).
DOI: 10.1016/j.compositesa.2003.08.002

[27] Psarras G. C.: Hopping conductivity in polymer matrix-metal particles composites. Composites Part A: Applied Science and Manufacturing, **37**, 1545–1553 (2006).
DOI: 10.1016/j.compositesa.2005.11.004

[28] Psarras G. C.: Charge transport properties in carbon black/polymer composites. Journal of Polymer Science Part B: Polymer Physics, **45**, 2535–2545 (2007).
DOI: 10.1002/polb.21278

[29] Psarras G. C.: Conduction processes in percolative epoxy resin/silver particles composites. Science of Advanced Materials, **1**, 101–106 (2009).
DOI: 10.1166/sam.2009.1015

eXPRESS Polymer Letters Vol.4, No.4 (2010) 244–251
Available online at www.expresspolymlett.com
DOI: 10.3144/expresspolymlett.2010.31

Study of the stress oscillation phenomenon in syndiotactic polypropylene/montmorillonite nanocomposites

*D. E. Mouzakis**

Technological Educational Institute of Larisa, Department of Mechanical Engineering, A.T.E.I of Larisa, GR-411 10, Larisa, Hellas (Greece)

Received 5 October 2009; accepted in revised form 17 February 2010

Abstract. The phenomenon of Stress Oscillation (SO) was studied in syndiotactic polypropylene and syndiotactic polypropylene nanocomposites with montmorillonite. The effect was provoked by varying the crosshead speed during tensile testing of thin stripes. The internal morphology of the stress oscillated specimens was studied by scanning electron microscopy on chemically etched samples revealing that cavitation prevails inside the opaque stripes of the yielded areas. Differential scanning calorimetry proved that there exists virtually no crystallinity differentiation between the characteristic alternating opaque/transparent stripes that mark the stress oscillation during necking. Finally a simple finite element model of the necking area of the specimens revealed non-uniform internal stress distributions of yield-point magnitudes.

Keywords: *nanocomposites, polymers, stress oscillation, syndiotactic polypropylene, material testing*

1. Introduction

The stress oscillation phenomenon, which occurs at the phase of cold drawing of tensile specimens during testing, was observed in 1924 for the first time, for thin metal sheet, deformed at low temperatures [1]. Stress oscillation (SO) is usually observed during the stable propagation of the neck in polymers under tensile loading. The phenomenon begins with a sudden fluctuation of the normally constant or slightly rising necking stress, resulting in a periodic stress-strain variation. This stress fluctuation is accompanied by the appearance of alternating transparent/opaque zones in the necking area of the specimen [2]. The stress oscillation effect can appear either during semi-static [2] or tensile impact loading [3–5], spontaneously [2–4] or provoked [6], by an abrupt change in the specimen loading speed. It can be observed for both amorphous and semi-crystalline polymers too. Amorphous but crystallisable polymers like poly(ethylene terephtalate) also exhibit this effect [7]. Moreover, it was also observed in amorphous non-crystallizable polymers like polycarbonate (PC) [6]. Quite a lot of effort has been invested by different researchers, employing different approaches to interpret this phenomenon. However the exact mechanism behind this phenomenon remains elusive. Adrianova *et al*. [8] has suggested that the formation of the alternating opaque/transparent zones is related to differential heat diffusion. Temperature at the necking region tends to fluctuate, because of the polymer poor heat conductivity and this causes a reduction in the local elastic modulus of the material, triggering thus stress oscillation. One of the most plausible explanations was proposed by Karger-Kocsis *et al.* [3]. He proposed that a combined effect of crystallization due to cold drawing of the polymer in the necking region accompanied by heat dissipation due to plastic flow leads to a 'stick/slip' mechanism of plastic deformation

*Corresponding author, e-mail: mouzakis@teilar.gr

which results in the appearance of the alternating zones. The same author proposed that in syndiotactic polypropylene (sPP) samples [2] a local elasto-plastic deformation network is being created, characterized by trans-planar crystallized segments. These segments cause a strain-hardening effect during the material necking which leads to stress fluctuation. Gatos *et al.* [9] have successfully shown that the result of the stress oscillation in sPP is a differentiating crystallization scheme in the opaque and the transparent zones of the specimens. According to Bazhenov *et al.* [10, 11], pores which are created in the plastic deformation region and polymer heat conductivity are the main factors influencing the mechanism of stress oscillation. Toda *et al.* [12] have worked on a variety of polymers with regard to stress oscillation. They utilized Barenblatt's thermomechanical model [13] and by using an infrared camera they observed that during the necking of polymers local temperature can overshoot the glass transition temperature. In this way they have concluded that local temperature peaks can lead to local enhancements in the polymer crystallinity which could result in strain hardening and therefore stress oscillation phenomena. Recently, Ronkay and Czigány [14] recognized the existence of cavitational yielding within the stress oscillated area of specimens. They proposed that micro-voids form in the presence of shear stresses acting in the area where the neck propagates in the bulk polymer. However the exact mechanism of microvoid formation has not been clarified yet.

This work focuses on the stress oscillation phenomenon as it was observed for specimens manufactured by hot pressing of sPP and its nanocomposites with montmorillonite. The stress oscillation phenomenon was provoked by alterations of the crosshead speed. Stress oscillated areas of these specimens where studied by means of differential scanning calorimetry and scanning electron microscopy in order to reveal valuable evidence on the stress oscillation mechanism. Finite element modeling of the necking area of the specimens helped simulate the stress fields acting in the area where the stress oscillation takes place.

2. Materials and methods

Syndiotactic polypropylene (sPP) of high purity (M_w = 135 000 g/mol, tacticity 68%) from Fina Oil and Chemical Co. (USA) was used in this study. Nanocomposite films were manufactured by melt mixing of an organically modified (quaternary ammonium salt) montmorillonite (Cloisite®20A, Southern Clay, Inc, USA) with the polymer matrix and subsequent hot pressing. sPP and nanoclay were mechanically mixed for 3 min prior to a 3 min melting phase at 170°C. The final melt mixing took 3 more minutes. Afterwards, the mixture was hot-pressed at 170°C with a pressure of 20 bar for ca. 10 min and was finally quenched at 0°C. Thin films (200 μm) of sPP nanocomposites with several compositions of montmorillonite, 0, 0.5, 1, 2, 3 and 4 wt% were produced in this way. Prior to testing all specimens were isothermally annealed at 80°C for 20 min to ensure high crystallinity which favors stress oscillation in sPP [15].

Specimens of both pure sPP and its nanocomposites with montmorillonite in the form of rectangular stripes of 80×7.5×0.34 mm^3, were cut from press-molded sheet for tensile testing. Tensile tests were performed on a Hounsfield HK20-W (Tinius Olsen, Surrey, England) desktop machine. Force-elongation curves were digitally recorded for further processing. During tensile testing, the crosshead speed was varied by the operator in order to trigger the stress-oscillation effect. Crosshead speeds used were: 5 mm/min in order to produce a well pronounced necked area of the polymer and consequently speed was varied from 20 to 40 mm/min in order to trigger the initiation of stress oscillation effect.

Differential Scanning Calorimetry (DSC) experiments were conducted in a DSC Q100 (TA Instruments, New Castle, Delaware, USA) system. Samples were cut from the a) undeformed, b) white/opaque and c) transparent zones of the tensile specimens with respect to Figure 1, in order to establish changes in the crystallization behavior due to the

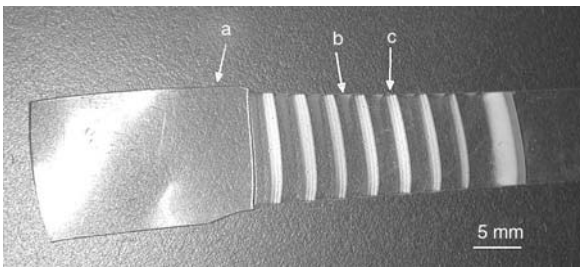

Figure 1. Optical photography of a sPP tensile specimen after stress oscillation: a) unstretched area, b) transparent zone και, c) opaque zone

stress/oscillation effect. Specimen heat/cool rate was 10°C and a heat/cool/heat scheme was applied to all specimens. Three repetitions were run for each different specimen. Specimen crystallinity was calculated from Equation (1) where $\Delta H_m^0 =$ 190.4 J/g is the well known heat of fusion of sPP crystals [6] (Equation (1)):

$$x = \frac{\Delta H_m - \Delta H_c}{\Delta H_m^0} = \frac{\Delta H_m - \Delta H_c}{190} \quad (1)$$

where, x is the % of crystallinity, ΔH_m and ΔH_c, melt and crystallization enthalpies respectively.

In order to study the internal structure of the necked area of the stress oscillated specimens samples were studied by a LEO SUPRA 35VP Field Emission (Carl Zeiss AG, Jena, Germany and a JEOL (Jeol Ltd, Tokyo, Japan) Scanning Electron Microscope. Some samples were selectively etched for 2 hours by using a 60/40 wt% acidic mixture of H_2SO_4/HNO_3 to which 2 wt% of $KMnO_4$ was added. Prior to SEM examination, specimens where covered with a layer of 20 nm Au in a BALZERS SCD 050 (Leica Microsystems, Liechtenstein) sputtering device.

3. Results and discussion

In Figure 1, the digital picture of the stress oscillated area of a sPP tensile specimen is shown. The specimen exhibits the typical characteristic specifications of such specimens: alternating opaque and transparent stripes. Figure 2 shows the load-displacement curve of that specimen. Initially, the specimen was subjected to a 5 mm/min crosshead speed and it has yielded in a normal mode as shown in this figure. Subsequently, the crosshead speed was changed to 40 mm/min causing an unstable stress oscillation event which soon attenuated (point *A* of the diagram). A few moments later, the crosshead speed was altered again to 30 mm/min (point *B* of the diagram) and this change triggered a smooth stress oscillation effect up to specimen rupture. Stripes in Figure 1 correspond to the latter phase *B* of the force-elongation curve of Figure 2. In both areas *A* and *B* where tensile speed was changed, it is evident that force rises to a maximum (strain hardening) prior to the initiation of stress oscillation. This strain hardening effect leading to stress oscillation is probably the key to understanding this phenomenon. It should be mentioned here, that only the 0.5 wt% in montmorillonite nanocomposite with sPP matrix, produced stress oscillations when subjected to the change of tensile speed. The force-elongation curve of such a specimen is shown in Figure 3. The stress oscillation for that specimen was provoked by initially starting at a crosshead speed of 20 mm/min and by sudden increase at 30 mmm/min. The stress oscillation here denoted by arrows in Figure 3 was unstable, with alternating force superimposed on typical strain hardening as seen in Figure 3. So, if more strain hardening can appear during plastic deformation then it must be localized in the oscillating area. All other concentrations, namely 1, 2, 3, and 4 wt% in montmorillonite yielded a typical force-elongation behavior of ductile polymers without any stress oscillation characteristics. In conclusion, the stress oscillation phenomenon from a yielding mechanism point of view appears to be an alternating procedure between strain hardening and plastic flow of the

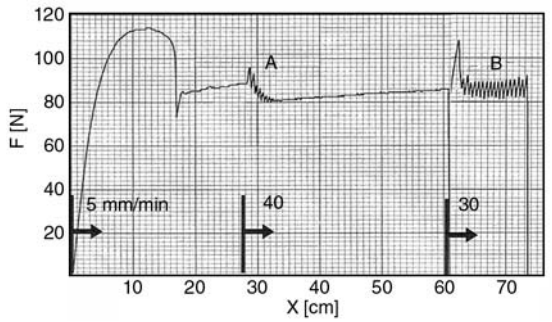

Figure 2. Stress oscillation scheme under crosshead speed variations in a sPP specimen: Region A: Crosshead speed switching from 5 to 40 mm/min, Region B: Crosshead speed switching from 40 to 30 mm/min

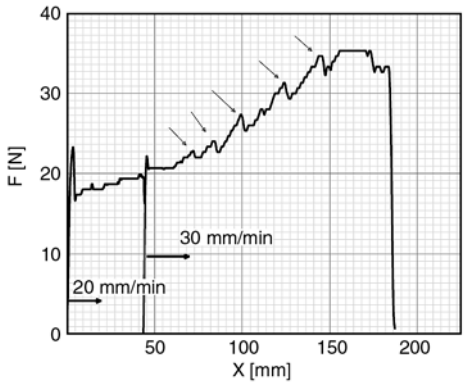

Figure 3. Stress oscillation scheme under crosshead speed variations in a nanocomposite sPP+0.5 wt% Cloisite 20A specimen. Arrows mark unstable oscillation peaks

necking area of the specimen as Karger-Kocsis has already suggested [5].

3.1. Crystallization behavior of the stress oscillation bands

Figure 4 presents the thermal behavior (heat flux) during the heating phase of the pure sPP specimen stress oscillated areas. Both the opaque and transparent stripes appear to have the same thermal response. Pure sPP shows a small endothermic peak at 100°C, which owes its existences to helical form I crystalline phase [6, 9]. In both opaque and transparent zones this peak is being suppressed as seen in Figure 3. This can be attributed the partial transformation of helical I to the trans-planar III conformation due to mechanical drawing of the polymer [6, 9].

Figure 5 shows the typical thermal behavior during heating of the 0.5 wt% montmorillonite nanocomposite stress oscillated samples. A small endothermic lump can be observed in all cases for these specimens at ca. 50°C which is typical for the partial melting of the unstable trans-planar III conformation [9] of the sPP matrix. A well pronounced helical I phase melting at 100°C is seen for the unstretched samples. This peak is being suppressed by cold drawing during the neck extension procedure.

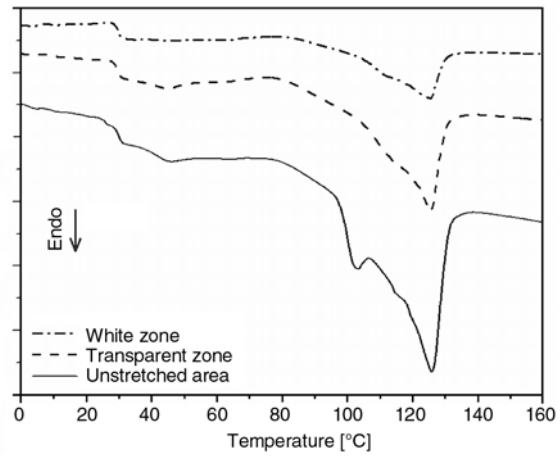

Figure 4. Differential Scanning Calorimetry during heating of sPP stress oscillated specimens

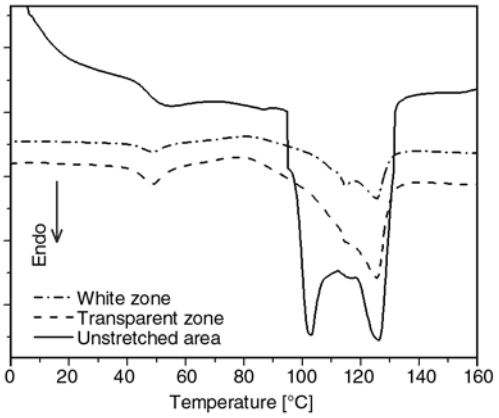

Figure 5. Differential Scanning Calorimetry during heating of a sPP+0.5% Cloisite 20A stress oscillated nanocomposite specimen

It is easy to conclude from Figure 5 that the thermal response of the opaque and transparent zones does not differentiate as observed for the pure sPP samples.

In Table 1 the results from the DSC experiments are summarized. There appears no significant impact of stress oscillation on the melting temperature of pure sPP. Also the overall crystallinity was calculated by Equation (1) of the opaque and transparent samples remains almost the same, whereas the unstretched samples yielded a little lower data. This implies that the effect of stress oscillation is a small rise due to orientation (cold drawing) in the material crystallinity. This has been also verified by García Gutiérrez *et al.* [15] by means of synchrotron-μSAXS who found no significant change in the crystallinity degree between opaque and transparent zones but only in the conformational order of the polymer. The corresponding crystallinity results for the 0.5 wt% montmorillonite nanocomposites are also shown in Table 1. Again, the results of the opaque and transparent zones exhibit the same amount of crystallization. Interestingly, the crystallinity of the nanocomposite-unstretched samples is almost 400% higher than the stress oscillated areas. Probably, this is the effect of the montmorillonite [16], which favours the crystal-

Table 1. DSC Crystallinity results for the pure sPP and sPP+0.5 wt% modified nanoclay content samples from stress oscillation tensile experiments

	Pure sPP			**sPP+0.5 wt% Cl.20A**		
	Opaque zones	**Transparent zones**	**Unstretched area**	**Opaque zones**	**Transparent zones**	**Unstretched area**
T_m [°C]	125.6±0.2	125.6±0.3	126.8±0.2	125.6±0.7	125.6±0.5	126.6±1.1
ΔH_m [J/g]	50.9±0.2	49.2±0.9	45.3±0.9	9.2±0.5	10.3±0.2	39.8±1.0
Crystallinity [%]	26.7±0.1	25.8±0.5	23.6±1.5	4.8±1.1	5.3±0.4	20.9±0.5

lization of helical form I of sPP [9, 16] during the isothermal crystallization phase. However, as seen from Figure 5 these conformations tend to vanish when mechanical stress is imposed. Probably, the mechanically re-oriented macromolecules lose their preferential form I conformation under mechanical loading.

3.2. Internal morphology and structure

SEM pictures assisted in determining the internal structure of the stress oscillated specimens. Between nanocomposites and pure sPP samples, no difference in the structure was observed, so the internal morphology of the latter is being discussed here. Figure 6, shows both the fracture surface and the edge-on side view of a stress oscillated sPP tensile specimen; many interesting observations can be made on the topography of the specimen. Firstly, the outer surface of the sample in Figure 6a shows an undulation pattern. Also, the fracture surface of the specimen which was separated exactly at the beginning of an opaque zone shows a distinct difference between the outer layers and internal core structure, as presented in the frame of Figure 6b. The outer skins of the oscillation zone surround an elliptical zone of different morphology, i.e. a skin-core structure is made visible. So, an important conclusion can be drawn here: stress oscillation phenomenon does not appear uniformly, not only in an optical manner, showing opaque and transparent zones but also exhibits non-uniformity across the specimens' thickness. However, it is rather unlikely that this shall produce differences in crystallinity, since the outer layer is common to both opaque and transparent zones. It is the core which produces the difference if any, due to cavitation procedure [14]. This finding required a deeper insight, so it was decided that some samples should

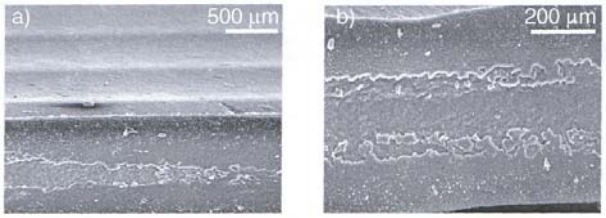

Figure 6. SEM microphotographs (fracture surface) of a stress oscillated sPP specimen which shows surface undulations (a) and skin-core cross-sectional morphology (b)

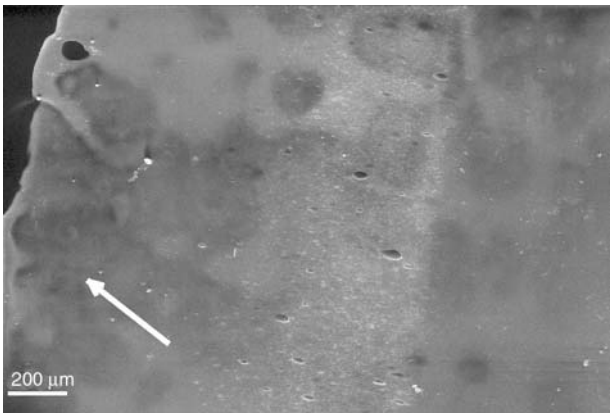

Figure 7. SEM microphotography of a stress oscillated sPP specimen after chemical etching. Arrow shows direction of tensile loading.

be chemically etched in order to remove the outer skin layers, in order to reveal the inner structure.
Up to this moment, researchers which have studied the internal morphology of the cross-section of stress oscillated tensile specimens proved the cavitational yielding mode of the white zones [14]. Therefore, some specimens where etched chemically as shown in parallel to the tensile direction. Figure 7 presents the top view aspect of a sPP tensile specimen as seen in the SEM after the chemical etching procedure has taken place. The white arrow on the left indicates the direction to which the tensile load was applied. A distinct bright grey zone can be seen in the middle of the specimen surrounded by two darker ones. This zone corresponds to one of the white zones of the specimen surrounded by the transparent ones. At this far field view, some cavities can be observed inside and in the vicinity of the white zone. So, the bright area corresponds to a white zone, being brighter to SEM

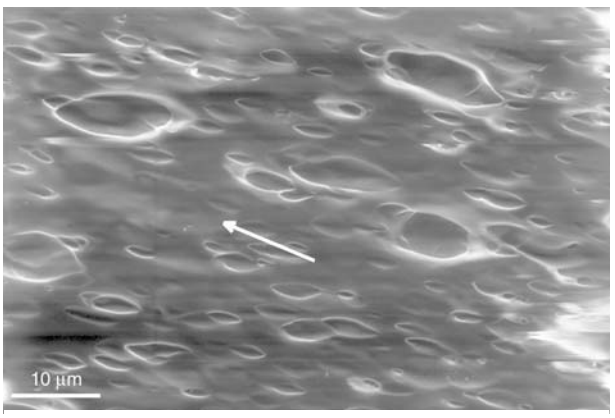

Figure 8. SEM microphotograph of the opaque (white) zone of a sPP tensile specimen. Arrow shows direction of tensile loading

because more electrons are reflected from cavity edges. As seen in Figure 8, which shows a part of the white zone of Figure 7 in higher magnification, the white zone is dominated by cavitational yielding. In other words, stress oscillation appears to invoke a secondary yielding mechanism during plastic flow (yielding) of the neck: cavitation. SEM frames of Figures 7 and 8 show larger and smaller cavities which are of elliptical shape. The arrows mark the tensile strain direction. It is most probable, that the elliptical shape of the cavities owes to tensile strain, since the main axes of these ellipses and tensile axis are the same as shown in that picture. On the other hand, it has been confirmed by numerous workers [17] that cavitational yielding is one of the major mechanisms of stress whitening in polymers and polymer matrix composites. So, perhaps the reason behind the formation of the opaque zones is a type of overstressing of the necking area of the specimen. Polymer cavitates in order to provide a relaxation mechanism to 3D stress fields acting in that area. Once the stresses have been accommodated and the excess elastic energy is dissipated into heat through cavitational yielding, the polymer returns into normal plastic flow forming a transparent zone. Further: strain hardening leads into overstressing again and once more another opaque zone forms by cavitation. This cycle is repeated many times until specimen fails or the phenomenon stops. The above scenario based on our SEM findings however, demands some theoretical modeling of the stress fields acting in the necking area of the tensile specimen by analytical or arithmetic techniques.

On the left, side of the white zone of Figure 7 the borderline between opaque and transparent zone appears to be more diffuse, whereas on the left the two areas are more distinctively separated. There appears to be an area in which there is a transition from the opaque to the transparent zone and vice versa. In every white (opaque) zone of the specimen one side is diffuse and the other is clearly separated from the adjacent transparent one. In order to confirm this finding, another different stress oscillated tensile specimen area was etched and examined in the JEOL 5400 SEM. This is the view given in the corresponding Figure 9. The area of transition (diffuse cavitation) is on the right side of the specimen, whereas on the left of the white–cavitated zone the separation between transparent zone

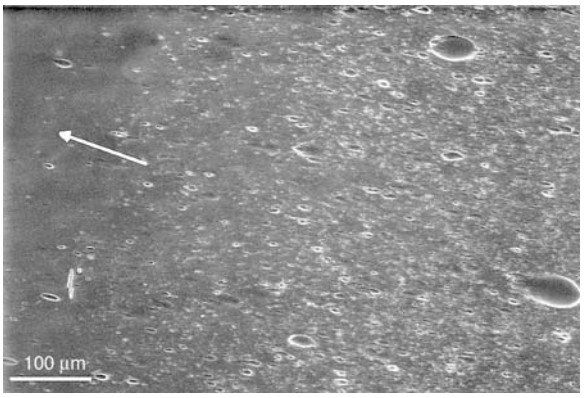

Figure 9. SEM microphotography of the transitional area (opaque to transparent) of a stress oscillated tensile specimen of sPP

and opaque is unmistakable. So our finding is confirmed: in some stage of the stress oscillation procedure a transitional area between opaque and transparent areas is being formed. The authors could not detect evidence whereas this transitional area forms when a transparent zone gives its place to an opaque one, or vice-versa.

3.3. Finite Element Modelling

In order to obtain some idea on the stress field acting during loading of a necked sPP specimen, a rough model was constructed and solved by employing ANSYS v.11 software (licensed to T.E.I. of Larisa). As shown in Figure 10, wedge-type geometry was chosen to represent the transitional area from necked/yielded to non-yielded specimen. The model was solved for half of the specimen due to symmetry. Of course this model was quasi-static and meant only to obtain some idea of the stress fields in necked sPP specimens; the ideal solution would be a dynamic model, but this is very difficult to perform due to the stress oscillation phenomenon. Due to the anisotropy of the stress fields expected here, owing to both the

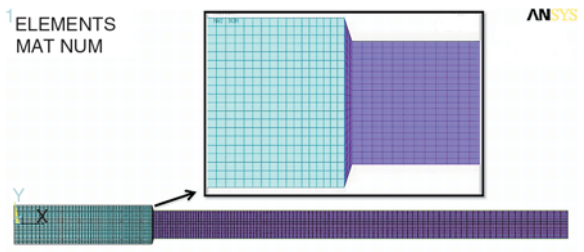

Figure 10. Finite Element Model of the dumbbell specimen of s-PP. Inset view shows the necking area in magnification.

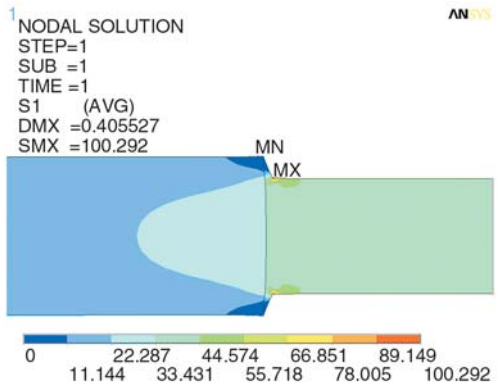

Figure 11. Principal stress results (*x*-direction) in the necking area of a tensile specimen of s-PP as calculated by FEM

geometry and the properties of the yielded/non-yielded areas of the specimen, principal stresses across the *x*-direction are depicted.

As seen in the contour plot of Figure 11 anisotropy in the distribution of stresses around the necked area is evident. Moreover, overstressing of the non-yielded area above the sPP yield point (ca. 20 MPa) is also observed (hyperbolic stress field left of the necked area). Also, some points of high stresses can be seen where the end of the wedge type region meets the necked specimen, but this is only due to the wedge steep angle. From the above analysis, though simplistic, an important conclusion can be drawn: In the non-yielded/non necked area of the sPP specimens, non uniform stress fields act, imposing stresses higher or in the magnitude of the yield point. Naturally, that finding requires further detailed modeling taking into account the exact geometry features of the transitional necking area (i.e. differences in thickness and curvature of the wedge).

4. Conclusions

Based on the above discussion on the stress oscillation experimental observations and FEM results following conclusions can be drawn.

– The SO phenomenon was verified to initiate when test speed was altered for both sPP and its nanocomposite with nanoclay.
– The crystallinity within the stress oscillated area does not differentiate between transparent and opaque zones for both pure sPP and nanocomposite.
– The opaque stripes exhibit a skin-core morphology featuring an external skin covering the stress-whitened/cavitated core.
– Finite Element Modeling showed non-uniform overstressing, ahead of the neck propagation area requiring further investigation.

Acknowledgements

The author is grateful to Mr. Angelos Mintzas of the Department of Engineering Science, University of Oxford, for his kind assistance in the procedure of Finite Elements Modelling. Thanks are also due to Dr V. Gregoriou's team in ICEHT-FORTH, Patras-Greece for providing the materials under study.

References

[1] Portevin A., Le Chatelier F.: Heat treatment of aluminium-copper alloys. Transactions of the American Society for Steel Treating, **5**, 457–478 (1924).

[2] Karger-Kocsis J., Shang P. P.: A modulated DSC study on the stress oscillation phenomenon in a syndiotactic polypropylene. Journal of Thermal Analysis and Calorimetry, **69**, 499–507 (2002).
DOI: 10.1023/A:1019903605228

[3] Karger-Kocsis J., Benevolenski O. I., Moskala E. J.: Toward understanding the stress oscillation phenomenon in polymers due to tensile impact loading. Journal of Material Science, **36**, 3365–3371 (2001).
DOI: 10.1023/A:1017935323058

[4] Mouzakis D. E., Karger-Kocsis J.: Effects of gasoline absorption on the tensile impact response of HDPE/Selar™ laminar microlayer composites. Journal of Applied Polymer Science, **68**, 561–569 (1998).
DOI: 10.1002/(SICI)1097-4628(19980425)68:4<561::AID-APP7>3.0.CO;2-K

[5] Karger-Kocsis J., Czigány T., Moskala E. J.: Stress oscillation in amorphous copolyesters due to tensile impact. Polymer Engineering and Science, **39**, 1404–1411 (1999).
DOI: 10.1002/pen.11531

[6] Gregoriou V. G., Kandilioti G., Gatos K. G.: An infrared spectroscopic approach to the polymorphic behavior of syndiotactic polypropylene and its crystal-crystal transformation during mechanical stretching. Vibrational Spectroscopy, **34**, 47–53 (2004).
DOI: 10.1016/j.vibspec.2003.08.004

[7] Ebener H., Pleuger B., Petermann J.: Stress and strain oscillations in syndiotactic polypropylene and in poly(ethylene terephthalate). Journal of Applied Polymer Science, **71**, 813–817 (1999).
DOI: 10.1002/(SICI)1097-4628(19990131)71:5<813::AID-APP15>3.0.CO;2-P

[8] Andrianova G. P., Kechekyan A. S., Kargin V. A.: Self-oscillation mechanism of necking on extension of polymers. Journal of Polymer Science Part A 2: Polymer Physics, **9**, 1919–1933, (1971).
DOI: 10.1002/pol.1971.160091101

[9] Gatos K. G., Kandilioti G., Galiotis C., Gregoriou V. G.: Mechanically and thermally induced chain conformational transformations between helical form I and trans-planar form III in syndiotactic polypropylene using FT-IR and Raman spectroscopic techniques. Polymer, **45**, 4453–4464 (2004).
DOI: 10.1016/j.polymer.2004.03.095

[10] Bazhenov S. L., Rodionova Yu. A., Kechek'yan A. S., Rogozinskii A. K.: On the role of thermal conductivity in the formation of self-excited oscillation in poly(ethylene terephthalate). Polymer Science, Series A, **47**, 692–699 (2005).

[11] Kechek'yan A. S., Rodionova Yu. A., Bazhenov S. L.: On the role of pore formation in oscillatory neck propagation in poly(ethylene terephthalate). Polymer Science, Series A, **47**, 126–133 (2005).

[12] Toda A., Tomita C., Hikosaka M., Hibino Y., Miyaji H., Nonomura C., Suzuki T., Ishihara H.: Thermo mechanical coupling and self-excited oscillation in the neck propagation of PET films. Polymer, **43**, 947–951 (2002).
DOI: 10.1016/S0032-3861(01)00625-5

[13] Barenblatt G. I.: Neck propagation in polymers. Rheologica Acta, **13**, 924–933 (1974).
DOI: 10.1007/BF01526675

[14] Ronkay F., Czigány T.: Cavity formation and stress-oscillation during the tensile test of injection molded specimens made of PET. Polymer Bulletin, **57**, 989–998 (2006).
DOI: 10.1007/s00289-006-0670-8

[15] García Gutiérrez M. C., Karger-Kocsis J., Riekel C.: Stress oscillation-induced modulated phase transformation and yielding in syndiotactic polypropylene. Chemical Physics Letters, **398**, 6–10 (2004).
DOI: 10.1016/j.cplett.2004.09.023

[16] Mouzakis D. E., Kandilioti G., Elenis A., Gregoriou V. G.: Ultraviolet radiation induced cold chemi-crystallization in syndiotactic polypropylene clay-nanocomposites. Journal of Macromolecular Science Part A: Pure and Applied Chemistry, **43**, 259–267 (2006).
DOI: 10.1080/10601320500437110

[17] Karger-Kocsis J., Fakirov S.: Nano- and micromechanics of polymer blends and composites. Hanser, Munich (2009).

eXPRESS Polymer Letters Vol.4, No.4 (2010) 252–262
Available online at www.expresspolymlett.com
DOI: 10.3144/expresspolymlett.2010.32

Effect of layered silicate nanoclay on the properties of silane crosslinked linear low-density polyethylene (LLDPE)

H. Azizi[1*], *J. Morshedian*[1], *M. Barikani*[1], *M. H. Wagner*[2]

[1]Iran Polymer and Petrochemical Institute, P.O.Box 14965/115, Tehran, Iran
[2]Polymertechnik/Polymerphysik, TU-Berlin, Fasanenstr. 90 D, 10623, Berlin, Germany

Received 23 December 2009; accepted in revised form 17 February 2010

Abstract. In the present work, the effect of pristine layered silicate montmorillonite (MMT) nanoclay on the properties of silane-crosslinked LLDPE prepared by melt compounding is investigated. The effect of the sequence of feeding additives (nanoclay and grafting agent) into the mixer on gel content, thermal and mechanical properties were studied. Results demonstrate that the sequence of feeding additives influences the final properties of nanocomposites. For samples prepared by first grafting of silane on LLDPE followed by incorporation of nanoclay into the polymer matrix, the gel content and the rate of crosslinking increased, while the elongation at break decreased. For samples prepared by first mixing nanoclay into the LLDPE matrix followed by the grafting reaction, the rate of crosslinking and the tensile properties did not change significantly. The gel content increased with increasing content of nanoclay for both process routes due to an enhanced permeation of water molecules into the polymer matrix in the presence of polar montmorillonite particles. Wide angle X-ray scattering (WAXS) results proved the intercalation/partial exfoliation morphology of nanoclay in the silane-grafted LLDPE matrix. Differential scanning calorimetry (DSC) data showed multiple melting behaviour for crosslinked samples which is indicative for different crystalline structures of the sol and gel part of the LLDPE matrix.

Keywords: *nanocomposites, LLDPE, silane crosslinking, layered silicate, gel content*

1. Introduction

Linear low-density polyethylene (LLDPE) is a versatile material for application in cable and film manufacturing industries. The silane crosslinking process converts the virgin polyethylene to a new material with improved upper service temperature, chemical and environmental stress cracking resistance (ESCR) and electrical properties [1–3]. Crosslinked linear low-density polyethylene (XLLDPE) is used for low-to-medium voltage power cable insulation and heat shrinkable films. The use of mineral fillers to adjust the properties of silane – crosslinked polyethylene is well established. Metal hydroxides such as magnesium hydroxide and aluminium tri-hydrate are usually used to improve the flame retardancy of crosslinked polyethylene. Calcium carbonate is also used to adjust price and elastic modulus. However, to achieve desirable properties, a high loading of mineral fillers should be used which may lead to a dramatic decrease in mechanical properties and an increase of the density of the final product [4–9]. Also, the effect of aluminium hydroxide, antimony trioxide and EVA on the properties of silane crosslinked LDPE was investigated [10].

It has been reported that using layered silicates with large aspect ratios (a few nanometer thick but hundreds to thousands of nanometers long) in a polymer matrix improves mechanical properties [11–13], reduces thermal expansion coefficient [14], gas permeability [15] and flammability [16, 17] of the polymer. These improvements can be achieved

*Corresponding author, e-mail: h.azizi@ippi.ac.ir

by using small amounts of nanofiller (≤5%) compared to ~40% for micro-fillers. The main problem in the preparation of PE/layered silicate nanocomposites is the difference in the polarity of nonpolar polyethylene versus polar filler leading to weak interfacial adhesion between polymer matrix and nanofiller. Several strategies have been followed to improve the intercalation of polyethylene into the layers of nanoclay including *in situ* polymerization of polymer in the presence of nanoclay, modification of nanoclay with non-polar groups [18, 19], solvent blending [20], and using compatibilizers (usually maleated PE or PP), which is the most common method in the melt compounding process of nanocomposites [21–26].

According to the studies reported in the literature about modification of layered silicates with alkoxy silane [27–30] it can be expected that using layered silicates in silane grafted polyethylene leads to improved intercalation and exfoliation of nanofiller in the presence of polar silane-grafted polyethylene. Moreover, the flammability and barrier properties can be improved which are two important parameters in the film and packaging industries. The main target of this work is to present the results of the effect of nanoclay on the gel content of silane-grafted and moisture crosslinked polyethylene. The effect of adding nanoclay before or after silane-grafting of LLDPE was investigated. Morphological studies were performed to interpret the changes in mechanical and network properties resulting from the addition of nanoclay.

2. Experimental

2.1. Materials

The polymer matrix used in this study was a linear low-density polyethylene with trade name LL209AA from Arak Petrochemical Co. (Iran), with melt flow index (MFI) of 0.9 g/10 min and density = 0.920 g/cm^3.

The nanofiller was layered silicate (Cloisite Na^+) from Southern Clay Products Inc., USA. It is a natural montmorillonite (MMT) without any modification, density = 2.86 g/cm^3 and *d*-spacing (d_{001}) = 11.7 A°. This grade was chosen because of its higher hydrophilicity compared to other commercial grades.

The grafting additive was Siflin 13 which is a mixture of 92.5 wt% vinyl-tri-methoxysilane (VTMOS) and 7.5 wt% di-cumyl-peroxide (DCP) from Evonik, Germany in liquid form.

2.2. Processing

An internal mixer from Brabender, Germany (model WHT 55), with roller type rotors and mixer capacity of 55 cm^3 was used for preparation nanocomposites and silane-grafted samples. A fill factor of 0.75 was selected based on the density of the compounds. The amount of silane/DCP content was kept constant at 1.8 phr (parts per hundred parts of polyethylene) which means 1.665 phr VTMOS and 0.135 phr DCP. Three levels of MMT were used: 1, 2 and 3 phr. One sample of silane-grafted polyethylene without nanoclay was also prepared. Two different methods were used for preparation silane-grafted LLDPE/MMT nanocomposites based on the sequence of feeding additives into the mixer as follows:

1) First addition of nanoclay into the mix, followed by incorporation of the grafting additives to produce silane-grafted polyethylene. We designate the data obtained by this process as 'Before-grafting (BG)'. For this process, the nanoclay was added at 2 min of mixing, and Siflin 13 was added at 3 min of mixing. The total mixing time was 12 min.
2) First addition of grafting agents into the mix, followed by incorporation of nanoclay. We name this process as 'After-grafting (AG)'. For this process the grafting agents were added at 2 min, and the nanoclay was added at 8 min of mixing. The total mixing time was 17 min.

The screw rotation speed was constant at 60 rpm for all experiments. The temperature was fixed at 125°C for 3 min, and then increased to 190°C with a rate of 32°C/min. The mixing was continued for different periods of time based on the processes selected. For both processes, at first polyethylene was fed to the mixer and was molten. After melting of the polymer, nanoclay and/or grafting agents were added. We choose approximately similar mixing times for the nanoclay, resulting therefore in different total mixing times of the two processes. For all experiments the variation of torque of the internal mixer with time was monitored during the mixing/grafting process.

Samples from internal mixer were compression moulded in a laboratory press (Toyoseiki, Japan) at

200°C/25 MPa to form sheets and films. The films were used for FTIR characterization, and the sheets with 1 mm thickness were used for investigation of mechanical properties and for morphological studies.

2.3. Crosslinking

Crosslinking of silane grafted samples was performed in hot water at 90°C. The total time of crosslinking was 24 hours. The sheets prepared by compression moulding were put in a hot water bath. At different periods of time (1, 3, 5 and 24 h), a piece was cut from the sheets for determination of gel content.

2.4. Analyses

Fourier transfer infrared spectroscopy (FTIR) was used to follow the formation of new chemical groups upon silane grafting and MMT addition. The films were washed by excess acetone before FTIR scans to remove unreacted silane. In this study the FTIR spectra were recorded by a Perkin-Elmer 2000X collecting 25 scans and using a resolution of 4 cm^{-1}.

Tensile properties were measured according to ASTM D 638 with a tension rate of 25 mm/min at room temperature. Dumbbell-shaped specimen for measurement of tensile properties were punched from crosslinked sheets.

The gel content of samples was measured according to ASTM D 2765 by extraction of the samples in p-xylene for 16 h. Small angle X-ray scattering (WAXS) was used to study the morphology of the nanocomposites and of the virgin clay. The X-ray beam was Co-Ka ($\lambda = 0.17889$ nm) radiation. The scanning rate was 0.05°/s, and the scattering angle 2-theta ranged from 4 to 10°.

Melting and crystallization behaviour were studied by a differential scanning calorimeter, model 8220 from Mettler Toledo, Germany. The heating program was as follows:

– First heating scan: Heating from 40 to 200°C with a rate of 10°C/min.
– Keeping the sample at 200°C for 5 min to erase the thermal history.
– First cooling scan: Cooling to 40°C with a rate of 10°C/min.
– Second heating scan: Heating from 40 to 200°C with a rate of 10°C/min.

The melting and crystallization peaks were obtained from the second heating and first cooling scans, respectively. Percent of crystallinity was calculated from the area of melting (ΔH_m) by using 293 J/g for heat of fusion of 100% crystalline polyethylene [31] according to the Equation (1):

$$\text{percentage of crystallinity} = \frac{\Delta H_m}{293} \cdot 100 \qquad (1)$$

3. Results and discussion

3.1. Mixing/grafting evaluation

The variation of torque as a function of mixing time for samples containing different nanoclay concentrations and prepared by the two different process routes is shown in Figures 1 and 2. The first peaks in the figures correspond to the melting of polyethylene. The second peaks are related to the grafting of silane onto the polyethylene. A small increase in torque was observed with the incorporation of nan-

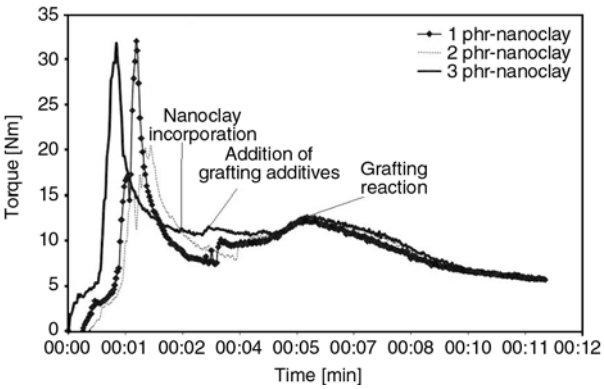

Figure 1. Variation of internal mixer torque with time for different samples prepared by BG process

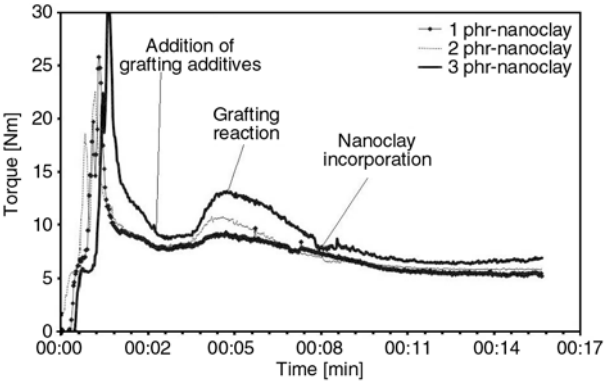

Figure 2. Variation of internal mixer torque with time for different samples prepared by AG process

oclay at 3 min for the BG process, and at 8 min for the AG process. The peak for grafting confirms that the grafting reaction has successfully taken place.

3.2. FTIR analysis

Figure 3 shows FTIR spectra for virgin LLDPE and pure montmorillonite. For pure MMT, four peaks at 521 cm^{-1} (Si–O bending), 1010 cm^{-1} (Si–O stretching, in-plane), 1650 cm^{-1} (–OH bending, hydration) and 3635 cm^{-1} (–OH stretching or Al–Al–OH stretching) were observed. The FTIR spectra of silane grafted LLDPE and corresponding nanocomposites with 3 phr MMT obtained from the two different processes are shown in Figure 4. The main differences between nanocomposites and virgin silane-grafted LLDPE are the appearance of new peaks at 1033, 362 and 514 cm^{-1}. The new absorbance peaks lead to broadening the peaks of 1090 and 3600 cm^{-1} of the virgin silane-grafted sample. The peak at 1033 cm^{-1} is due to Si–O–Si stretching vibrations, and the peak at 3620 cm^{-1} corresponds to Al–Al–OH stretching. However, it should be noted that some of the peaks in silane-grafted polyethylene/MMT nanocomposites are overlapping with the peaks of virgin silane-grafted polyethylene because of some similar groups such as Si–OCH_3. The characteristic peaks for Si–O–C groups appear at 1090, 1182 and 817 cm^{-1}. A small peak at 1620 cm^{-1} due to bending vibration of –OH groups can be seen for the nanocomposites. The peak at 514 cm^{-1} is due to bending vibration of Si–O groups in MMT. A possible reaction is the formation of chemical bond between nanoclay and grafted polyethylene chains via hydrolysis of methoxy groups to form silanol groups, and consequently the reaction of silanol groups of silane-grafted polyethylene with –OH groups in the nanoclay by a condensation reaction, which leads to the formation PE–Si–O–Si–MMT. The characteristic peak for Si–O–Si stretching vibration appears at 1033 cm^{-1}. This reaction is possible because of the presence of water in nanoclay. In general, the FTIR spectra confirm the grafting reaction, and presence of nanoclay in the polyethylene matrix.

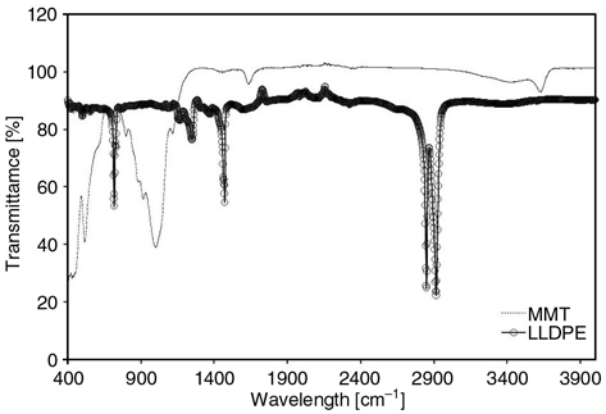

Figure 3. FTIR spectra of virgin LLDPE and pure montmorillonite (MMT)

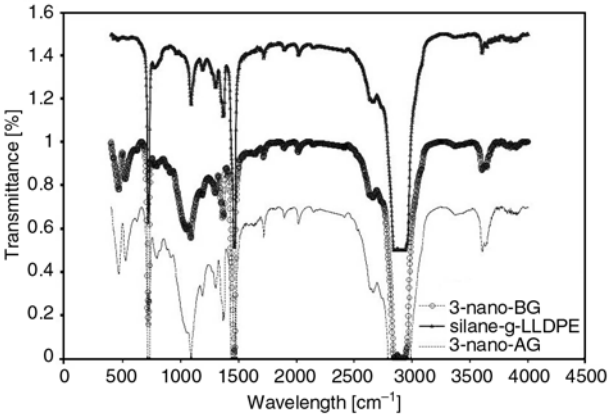

Figure 4. FTIR spectra of silane grafted LLDPE and its nanocomposites with 3 phr nanoclay prepared by different methods

3.3. WAXS analysis

Figure 5 shows the diffraction patterns of virgin nanoclay (MMT) and of different silane-grafted LLDPE/MMT nanocomposites prepared by the two different methods. The WAXS patterns indicate the intercalation/partially exfoliation of the MMT in the LLDPE matrix. A shift of the characteristic diffraction peak to lower 2θ-angles indicates the increasing *d*-spacing between silicate layers in

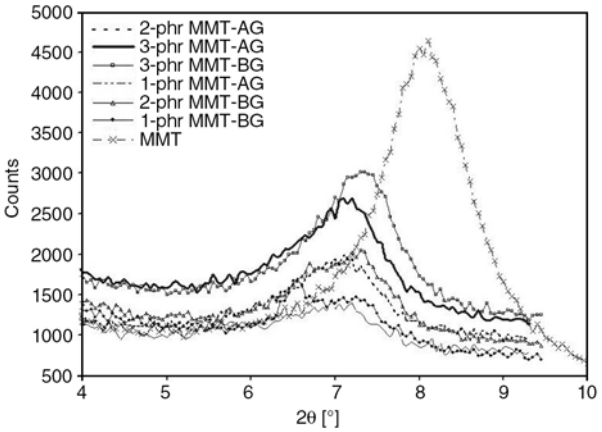

Figure 5. XRD spectra of virgin MMT powders and silane-grafted LLDPE/MMT nanocomposites prepared by AG process and BG process

MMT, which is referred to as intercalation. The broadening of the characteristic peak is suggested to be the result of partial exfoliation [32]. Disappearance of the peak would indicate full exfoliation, which was not observed for our samples with a constant amount of grafting agents. It seems that for samples containing 1 and 2 phr of nanoclay, partial exfoliation is easier achieved than for samples containing 3 phr nanoclay. On the other hand, samples prepared by the AG process showed enhanced intercalation compared to samples prepared by the BG process. However, it seems that the best intercalation was achieved for the sample containing 1 phr nanoclay prepared by the BG process, since for this sample, the shift of the 2θ-angle to lower scattering angles is more pronounced than for all other samples (from 8.1 to 6.5°).

3.4. Effect of nanoclay on gel content

Gel content is an important parameter in crosslinked polyethylene because many properties of the material will be affected by this parameter. For wire and cable insulation, which should pass the hot-set test, gel content is the most important parameter. For the silane crosslinking technology, the rate of crosslinking is an issue for crosslinking of thick shapes. Silane crosslinking needs more time than other crosslinking methods such as peroxide crosslinking and irradiation crosslinking. This drawback limits the application of the silane crosslinking technology to thin products. In industry, often catalysts are used to increase the rate of crosslinking. However, catalysts based on a tin compound (di-butyl-tin-dilaurate) are environmentally harmful and expensive. Figures 6 and 7 show the variation of gel content for samples with different content of nanoclay as obtained by the two process routes. Parameter is the crosslinking time. For the BG process, the gel content does not change significantly with nanoclay loading. However, the gel content for the sample containing 1 phr nanoclay was somewhat higher than for the other samples. This may be attributed to a better dispersion (partial exfoliation of nanoparticles as seen from WAXS) of this sample. The better dispersion of nanoclay results in a more uniform distribution of water molecules in the samples, which leads to higher gel content.

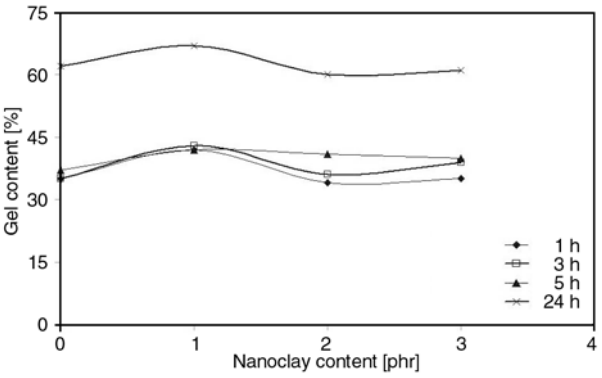

Figure 6. Change of gel content with nanoclay concentration for samples obtained from BG process

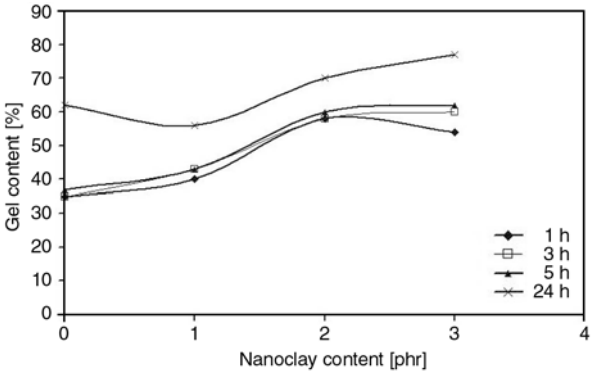

Figure 7. Change of gel content with nanoclay concentration for samples obtained from AG process

For samples prepared by AG process, in which nanoclay was added after the silane grafting reaction, a different behaviour is observed. For these samples, the gel content increases with the increase of the nanoclay content. The lower gel content observed in samples prepared by the BG process in comparison to samples produced by the AG process seems to be due to the absorption of silane molecules by the nanoclay before grafting to the polyethylene chains. A reaction of silane molecules with the nanoclay due to –OH groups in the nanoclay structure is very likely. The variations of the gel content for different MMT concentrations as a function of the crosslinking time are shown in Figures 8 and 9 for the two process routes. It is clear from Figure 9 that incorporation of pristine nanoclay even at low amounts increases significantly the rate of crosslinking. The rate of crosslinking increases with increase of nanoclay loading, with the increase of the rate of crosslinking being more pronounced for samples containing 2 and 3 phr of nanoclay. For samples prepared via BG process, no significant change in the rate of crosslinking was observed except for the sample with 1 phr of nanoclay, which showed a

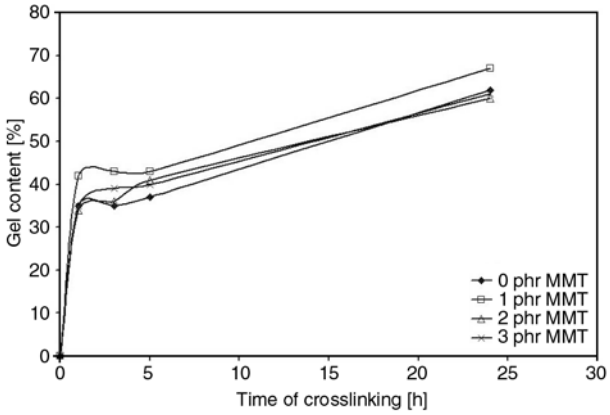

Figure 8. Variation of gel content with time of crosslinking for samples prepared by BG process

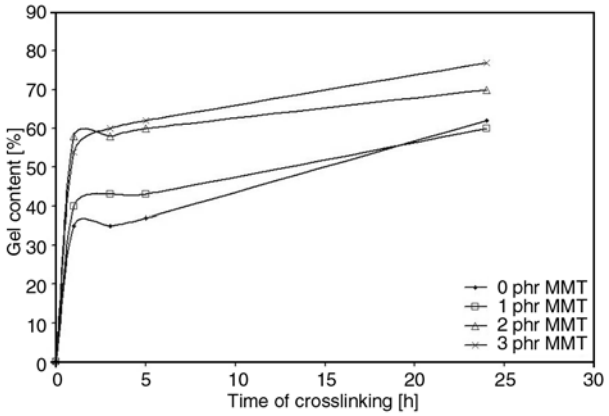

Figure 9. Variation of gel content with time of crosslinking for samples prepared by AG process

Table 1. The ratio [%] between gel contents at 3 and 24 hrs for different samples prepared by different process routes

MMT content	0	1 phr	2 phr	3 phr
Before grafting [%]	56	64	60	64
After grafting [%]	56	72	83	80

small increase in the rate of crosslinking. The percentage of gel content achieved after 3 hours of crosslinking (i.e. the ratio between the gel content at 3 hours and at 24 hours of crosslinking) are listed in Table 1 for the different samples. For the BG process, the maximum percentage of final gel content was obtained for samples containing 1 and 3 phr of nanoclay with 64% compared to 56% for the sample without nanoclay. For the AG process, the percentage of maximum gel content was increased to 72% for the sample with 1 phr nanoclay, and to 83 and 80 % for samples containing 2 and 3 phr nanoclay, respectively.

It is well-known that in silane-crosslinked polyethylene, crosslinking takes place first by hydrolysis of methoxy groups ($–OCH_3$) to form silanol groups (Si–OH). Then via a condensation reaction, the silanol groups will change to siloxane (Si–O–Si) bonds between the polyethylene chains. Therefore, the availability of water is a key parameter in silane crosslinking of polyethylene. The permeation of water molecules into the polymer backbone is a low-speed and time-consuming process. Pristine clay is filler with a higher polarity and hydrophilicity compared to other commercial organically modified montmorillonites (OMMT), because of the presence of Na^+ cations and –OH groups in its structure. Modification of MMT is usually done by ion exchange reactions using ammonium salts. Therefore it can be concluded that the addition of pristine nanoclay increases the absorption of water molecules by the polymer matrix leading to an increase of the crosslinking rate. The well-dispersed nanoclay leads to a uniform distribution of water molecules in polyethylene. However, it should be kept in mind that nanoclay could in principle also have a detrimental effect on the permeation of water molecules into the polymer matrix due to the barrier properties of nanoclay, which restrict gas and water permeation. The competition between these two effects (enhanced water absorption versus barrier properties) determines the rate of crosslinking. In the case of our study, it seems that water absorption of nanoclay is more important than its potential barrier properties. However, it should be noted that our samples were crosslinked in a hot water bath which guaranteed that enough water molecules were available for crosslinking.

3.5. Mechanical properties

Tensile tests were performed to investigate the effect of nanoclay loading on mechanical properties of silane-crosslinked LLDPE. Figures 10 and 11 illustrate the variation of tensile strength (stress at break) and elongation at break, respectively, as a function of nanoclay content for crosslinked samples. The data obtained for the two mixing methods, AG and BG, are presented. Different trends of variation are observed for the samples depending on the process route. For the BG process, tensile strength increased slightly with increasing MMT concentration, while for the AG process, tensile strength shows a tendency to decrease with nanofiller concentration. However, it should be noted that all the samples showed higher tensile strength

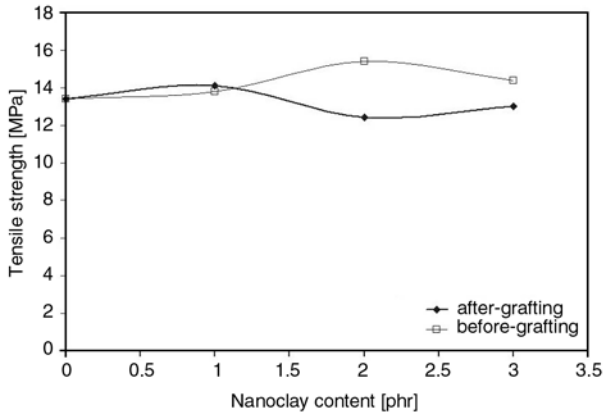

Figure 10. The effect of nanoclay content on tensile strength for samples prepared by different processes

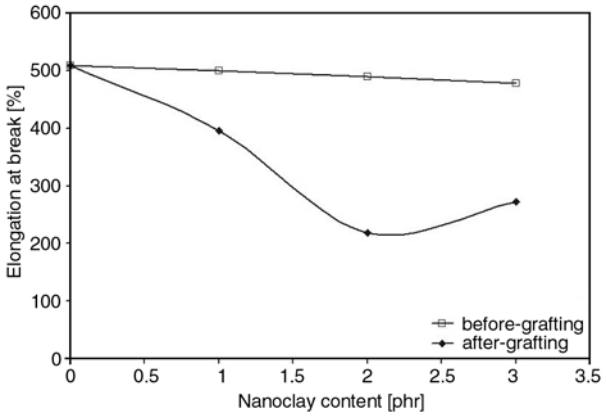

Figure 11. The effect of nanoclay content on elongation for samples prepared by different processes

Table 2. Change in tensile strength [%] of silane grafted LLDPE with nanoclay concentration

MMT content	1 phr	2 phr	3 phr
Before-grafting [%]	3.0	15.0	7.5
After-grafting [%]	5.2	–7.5	–3.0

than virgin uncrosslinked LLDPE. According to the manufacturer's data sheet, the tensile strength for virgin LLDPE is 11 MPa, and elongation at break is 620%. After crosslinking, the tensile strength increases due to the formation of strong chemical bonds between polymer chains. Table 2 summarizes the change of tensile strength of samples prepared by the two different mixing methods relative to virgin silane-crosslinked polyethylene. The maximum improvement was obtained by the sample with 2 phr nanoclay prepared by BG method with a 15% increase in tensile strength. The maximum relative reduction in tensile strength was observed for the sample containing 2 phr MMT prepared by the AG method. In general, it can be concluded that the tensile strength of silane grafted LLDPE shows

Table 3. Change in elongation [%] at break of silane grafted LLDPE with nanoclay concentration

MMT content	1 phr	2 phr	3 phr
Before grafting [%]	–1.7	–3.7	–6.0
After grafting [%]	–22.0	–57.0	–46.0

only small changes as a function of nanoclay content. Although for virgin PE/nanocomposites it has been reported that tensile strength increases with filler content [33, 34], in our study with silane-crosslinked polyethylene no significant change in tensile strength at MMT loading up to 3 phr was observed.

The variation of elongation at break versus MMT content is shown in Figure 11. For samples obtained by the BG process, elongation at break did not change considerably with filler content, although a slight decrease is observed. However, for samples obtained through the AG process, elongation at break decreased dramatically with nanoclay concentration. Table 3 summarizes the changes in elongation at break of samples prepared by the two different production methods relative to virgin silane-crosslinked polyethylene. The relative reduction of elongation at break was higher for samples prepared by the AG method and varied between 22 to 57%. The maximum reduction is observed for the sample with 2 phr nanoclay. One reason for such a decrease is the higher gel content of samples prepared by the AG process compared to samples prepared by the BG process. The crosslinks between polymer chains prevent the slippage of polymer chains past one another leading to a decrease in the elongation at break. Another reason may be the firmer integration of nanoclay particles by the AG process into the polymer matrix resulting in higher gel content, a denser network and more interfacial adhesion. This firmer integration affects both the tensile strength and the elongation at break of the samples.

3.6. Thermal properties

Figure 12 shows melting thermograms obtained from the first heating scan for different samples prepared by the two different mixing routes. As can be seen crosslinking changes the shape of melting peaks significantly. Multiple melting peaks are observed for crosslinked samples (with and without nanoclay addition) compared to the uncrosslinked

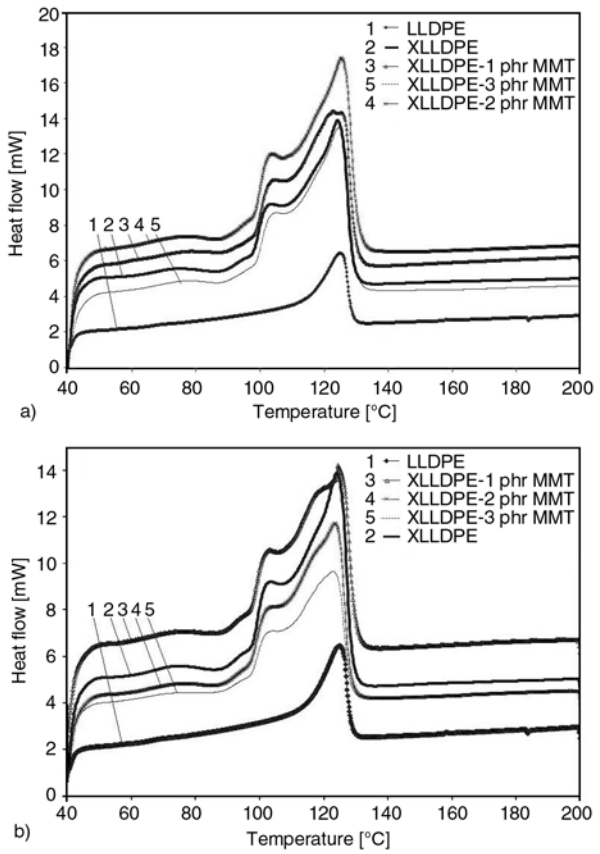

Figure 12. DSC thermograms of first heating scan for different samples prepared by a) BG process and b) AG process

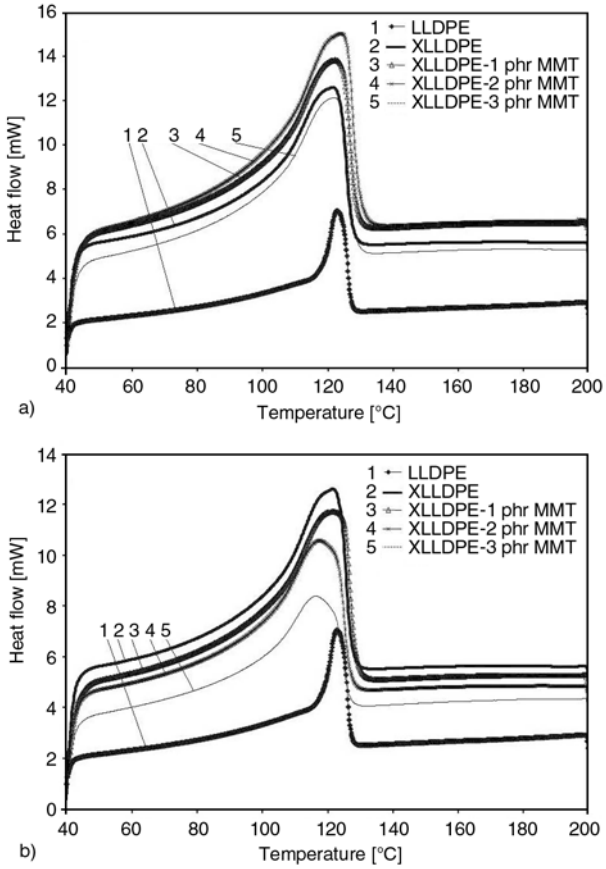

Figure 13. DSC thermograms of second heating scan for different samples prepared by A) BG process and B) AG process

polyethylene. For crosslinked samples, two melting peaks at about 103 and 124°C are observed. An endothermic shoulder is also seen at about 89°C for crosslinked samples. This type of melting behaviour reveals the molecular heterogeneity in the structure of crosslinked polyethylene. The two melting peaks may be attributed to the melting of two different components in the crosslinked polyethylene: the gel part and the sol part. The higher melting temperature corresponds to the sol part and is close to the melting temperature of uncrosslinked LLDPE (125°C). The lower melting temperature is related to gel part. The endothermic shoulder at 89°C may perhaps be attributed to the formation of newly formed Si–O–Si crystallites as studied by Kuan *et al*. [35]. Incorporation of MMT did not change the melting behaviour considerably indicating that the nanoclay has not acted as nucleating agent in this study.

The results for second heating scan are presented in Figure 13, and a different behaviour is observed. Here, no multiple melting peaks can be observed. The second peak at 103°C has disappeared, and instead a broad shoulder leading up to the melting peak at 124°C is observed. This may be due to an improved co-crystallization of the sol and gel part of the crosslinked polyethylene after heat treatment to 200°C.

Figure 14 illustrates the crystallization peaks for samples prepared by the different mixing methods. Similar to the melting behaviour at the first heating run, two different crystallization peaks are observed at temperatures of about 107°C (corresponded to crystallization of virgin LLDPE) and 98°C. For samples prepared by the AG process, with increasing nanoclay content the peak at 98°C becomes stronger than that the peak at 107°C, which weakens considerably. However, for samples prepared by the BG process, this is not the case. Tables 4 and 5 summarize the data obtained from DSC thermograms, and they include melting temperature (T_m) (from 2nd heating scan), crystallization temperature (T_c) for the strongest crystallisation peak, as well as percentage of crystallinity. For samples obtained by the BG process, the melting point did not change significantly with filler

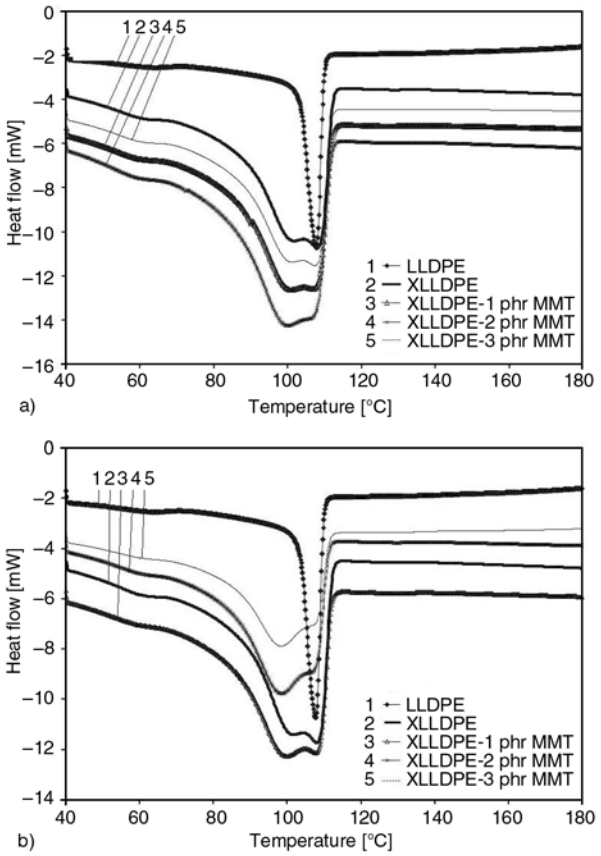

Figure 14. Crystallization peaks for different samples prepared by A) BG process and B) AG process

crosslinking and MMT content. However, for samples obtained by the AG process, the melting point shifted to lower temperatures with increasing nanoclay content. The decrease in the melting point with increasing nanoclay content may be attributed to a decreasing structural regularity of LLDPE in the presence of nanofiller. It is obvious from Tables 4 and 5 that crystallinity decreases with crosslinking. For samples prepared by the BG process, addition of nanoclay did not change the crystallinity, while for samples prepared by the AG process, crystallinity decreased with increasing nanoclay content. This reduction may be attributed to an increase of gel content of the samples prepared by the AG process.

4. Conclusions

Silane-grafted LLDPE/layered silicate nanocomposites were prepared by melt mixing in an internal mixer followed by crosslinking in hot water. The grafting additives were a mixture of vinyl-trimethoxysilane and di-cumyl peroxide. Two methods, AG and BG, were used based on the sequence of adding the grafting agents and the nanoclay into the polyethylene melt. Grafting was confirmed by FTIR analysis. A partially exfoliated morphology of the nanoclay was observed by WAXS measurements. The gel content of samples prepared by adding the nanoclay into grafted-LLDPE (process route AG) was higher than the gel content of samples prepared by adding the nanoclay before the grafting reaction (process route BG). The rate of crosslinking increased with increase of nanoclay content because of the high polarity of the nanofiller and the resulting increase in the absorption of water molecules. Tensile strength of silane grafted samples increased with the addition of nanoclay slightly, while elongation at break decreased dramatically for samples produced by the AG process. The melting behaviour of polyethylene is considerably affected by crosslinking. For samples prepared

Table 4. Melting point (T_m), crystallization point (T_c) and crystallinity percent for different samples prepared BG process

MMT content	LLDPE	XLLDPE	XLLDPE-1 phr MMT	XLLDPE-2 phr MMT	XLLDPE-3 phr MMT
T_m [°C]	122.71	121.19	121.80	123.72	121.82
[a]T_c [°C]	108.24	108.45	107.49	101.20	107.26
ΔH_m [J/g]	100.40	91.28	94.13	92.21	92.00
ΔH_c [J/g]	–89.57	–79.84	–83.63	–80.05	–80.71
Percent crystallinity [%]	34	31	32	31	31

[a]for T_c only the values for strong peak have been presented

Table 5. Melting point (T_m), crystallization point (T_c) and crystallinity percent for different samples prepared AG process

MMT content	LLDPE	XLLDPE	XLLDPE-1 phr MMT	XLLDPE-2 phr MMT	XLLDPE-3 phr MMT
T_m [°C]	122.71	121.19	122.53	117.25	116.50
[a]T_c [°C]	108.24	108.45	108.26	99.38	98.96
ΔH_m [J/g]	100.40	91.28	90.80	87.32	86.09
ΔH_c [J/g]	–89.57	–79.84	–80.33	–80.55	–76.63
Percent crystallinity [%]	34	31	30	29	29

[a]for T_c only the values for strong peak have been presented

by the AG process, the melting point shifted to lower temperatures with increasing nanoclay content, and a deceasing crystallinity was observed.

References

[1] Rado R., Zelenak P.: Crosslinking of polyethylene. International Polymer Science and Technology, **19**, 33–47 (1992).

[2] Thorburn B.: Crosslinking techniques for electrical jacketing materials. in 'Proceedings of ANTEC 94' Conference San Francisco, USA' 1379–1385 (1994).

[3] Roberts B. E., Verne S.: Industrial applications of different methods of crosslinking polyethylene. Plastic and Rubber Processing and Applications, **4**, 135–139 (1984).

[4] Billet C., Delfosse L.: The combustion of polyolefins filled with metallic hydroxides and antimony trioxide. Polymer Degradation and Stability, **30**, 89–99 (1990). DOI: 10.1016/0141-3910(90)90119-R

[5] Veselý K, Ruchlý J., Kummer M., Jancar J.: Flammability of highly filled polyolefins. Polymer Degradation and Stability, **30**, 101–110 (1990). DOI: 10.1016/0141-3910(90)90120-V

[6] Hippi U., Mattila J., Korhonen M., Seppälä J.: Compatibilization of polyethylene/aluminum hydroxide (PE/ATH) and polyethylene/magnesium hydroxide (PE/MH) composites with functionalized polyethylenes. Polymer, **44**, 1193–1201 (2003). DOI: 10.1016/S0032-3861(02)00856-X

[7] Anthonietta G., Shanks R. A.: Structural and thermal interpretation of the synergy and interaction between the fire retardant magnesium hydroxide and zinc borate. Polymer Degradation and Stability, **92**, 2–13 (2007). DOI: 10.1016/j.polymdegradstab.2006.10.006

[8] Yeh J. T., Yang H. M., Huang S. S.: Combustion of polyethylene filled with metallic hydroxide and crosslinkable polyethylene. Polymer Degradation and Stability, **50**, 229–234 (1995). DOI: 10.1016/0141-3910(95)00171-9

[9] Wang Z., Hu Y., Gui Z., Zong R.: Halogen-free flame retardation and silane crosslinking of polyethylenes. Polymer Testing, **22**, 533–538 (2003). DOI: 10.1016/S0142-9418(02)00149-6

[10] Azizi H., Barzin J., Morshedian J.: Silane crosslinking of polyethylene: The effects of EVA, ATH and Sb_2O_3 on properties of the production in continuous grafting of LDPE. Express Polymer Letters, **1**, 378–384 (2007). DOI: 10.3144/expresspolymlett.2007.53

[11] Patel H. A., Somani R. S., Bajaj H. C., Jasra R. V.: Nanoclays for polymer nanocomposites, paints, inks, greases and cosmetics formulations, drug delivery vehicle and waste water treatment. Bulletin of Materials Science, **29**, 133–145 (2006). DOI: 10.1007/BF02704606

[12] Vaia R.: Polymer nanocomposites open a new dimensions for plastics and composites. AMPTIAC Q, **6**, 17–24 (2002).

[13] Hussain F., Hojjati M., Okamoto R., Gorga R. E.: Polymer-matrix nanocomposites, processing, manufacturing and applications: An overview. Journal of Composite Materials, **40**, 1511–1575 (2006). DOI: 10.1177/0021998306067321

[14] Bhat G., Hedge R. R., Kamath M. G., Deshpande B.: Nanoclay reinforced fibers and nonwovens. Journal of Engineered Fibers and Fabrics, **3**, 22–34 (2008).

[15] Jiang L-Y., Wei K-H.: Bulk and surface properties of layered silicate/fluorinated polyimide nanocomposites. Journal of Applied Physics, **92**, 6219–6223 (2002). DOI: 10.1063/1.1516268

[16] Wang S., Hu Y., Qu Z., Wang Z., Chen Z., Fan W.: Preparation and flammability properties of polyethylene/clay nanocomposites by melt intercalation method from Na^+ montmorillonite. Materials Letters, **57**, 2675–2678 (2003). DOI: 10.1016/S0167-577X(02)01354-X

[17] Zhang J., Wilkie C.: Preparation and flammability properties of polyethylene-clay nanocomposites. Polymer Degradation and Stability, **80**, 163–169 (2003). DOI: 10.1016/S0141-3910(02)00398-1

[18] Heinemann J., Richert P., Thomann R., Mülhaupt R.: Polyolefin nanocomposites formed by melt compounding and transition metal catalyzed ethene homo- and copolymerization in the presence of layered silicates. Macromolecular Rapid Communications, **20**, 423–430 (1999). DOI: 10.1002/(SICI)1521-3927(19990801)20:8<423::AID-MARC423>3.0.CO;2-N

[19] Alexandre M., Dubois P., Sun T., Graces J. M., Jérome R.: Polyethylene-layered silicate nanocomposites prepared by the polymerization-filling technique: Synthesis and mechanical properties. Polymer, **43**, 2123–2132 (2002). DOI: 10.1016/S0032-3861(02)00036-8

[20] Song L., Hu Y., Wang S., Chen Z., Fan W.: Study on the solvothermal preparation of polyethylene/organophilic montmorillonite nanocomposites. Journal of Materials Chemistry, **12**, 3152–3155 (2002). DOI: 10.1039/b201488b

[21] Mehrabzadeh M., Kamal M.: Polymer-clay nanocomposites based on blends of polyamide-6 and polyethylene. The Canadian Journal of Chemical Engineering, **80**, 1083–1092 (2002). DOI: 10.1002/cjce.5450800610

[22] Koo C. M., Kim S. O., Chung I. J.: Study on morphology evolution, orientatinal behaviour and anisotropic phase formation of highly-filled polymer layered silicate nanocomposites. Macromolecules, **36**, 2748–2757 (2003). DOI: 10.1021/ma021377n

[23] Koo C. M., Ham H. T., Kim S. O., Wang K. H., Chung I. J.: Morphology evolution and anisotropic phase formation of the maleated polyethylene-layered silicate nanocomposites. Macromolecules, **35**, 5116–5122 (2002).
DOI: 10.1021/ma011770d

[24] Bafna A., Beaucage G., Mirabella F., Mehta S.: 3D hierarchical orientation in polymer-clay nanocomposite films. Polymer, **44**, 1103–1115 (2003).
DOI: 10.1016/S0032-3861(02)00833-9

[25] Gopakumar T. G., Lee J. A., Kongtopoulou M., Parent J. S.: Influence of clay exfoliation on the physical properties of montmorillonite/polyethylene composite. Polymer, **43**, 5483–5491 (2002).
DOI: 10.1016/S0032-3861(02)00403-2

[26] Kaempfer D., Thomann R., Mülhaupt K.: Melt compounding of the syndiotactic polypropylene nanocomposites containing organophilic layered silicate and in-situ formed core/shell nanoparticles. Polymer, **43**, 2909–2916 (2002).
DOI: 10.1016/S0032-3861(02)00113-1

[27] Antochshuk V., Jaromiec M.: Functionalized mesoporous materials obtained via interfacial reactions in self-assembled silica surfactant systems. Chemistry of Materials, **12**, 2496–2501 (2000).
DOI: 10.1021/cm000268p

[28] Mercier L., Pinnavaia T. J.: Direct synthesis of hybrid organic-inorganic nanoporous silica by a neutral amine assembly route: Structure-function control by stoichiometric incorporation of organosiloxane molecules. Chemistry of Materials, **12**, 188–196 (2000).
DOI: 10.1021/cm990532i

[29] Seçkin T., Gültek A., Içgduygu M. G., Önal Y.: Polymerization and characterization of acrylonitrile with γ-methacryloxypropyltrimethoxy-silane grafted bentonite clay. Journal of Applied Polymer Science, **84**, 164–171 (2002).
DOI: 10.1002/app.10289

[30] He H. P., Duchet J., Galy J., Gerard J-F.: Grafting of swelling clays with 3-aminopropyltriethoxysilane. Journal of Colloid and Interface Science, **288**, 171–176 (2002).
DOI: 10.1016/j.jcis.2005.02.092

[31] Hatakeyana T., Zhenhai L.: Handbook of thermal analysis. Wiley, New York (1998).

[32] Mittal V.: Polymer layered silicate nanocomposites: A Review. Materials, **2**, 992–1057 (2009).
DOI: 10.3390/ma2030992

[33] Barus S., Zanetti M., Lazzari M., Costa L.: Preparation of polymeric hybrid nanocomposites base on PE and nanosilica. Polymer, **50**, 2595–2600 (2009).
DOI: 10.1016/j.polymer.2009.04.012

[34] Zuiderduin W. C. J., Westzaan C., Huétink J., Gaymans R. J.: Toughening of polypropylene with calcium carbonate particles. Polymer, **44**, 261–275 (2003).
DOI: 10.1016/S0032-3861(02)00769-3

[35] Kuan H-C., Kuan J-F., Ma C-C. M., Huang J-M.: Structure characteristics and thermal properties of silane-grafted-polyethylene/clay nanocomposite prepared by reactive extrusion. Journal of Applied Polymer Science, **96**, 2383–2391 (2005).
DOI: 10.1002/app.21694